

สมบัติเทอร์มอดิเล็กทริกของไฮดรอนซิลิไซด์ที่สังเคราะห์โดยกระบวนการความร้อน



นางสาวอภาภรณ์ สกุลภาวะเวก

ศูนย์วิทยทรัพยากร  
จุฬาลงกรณ์มหาวิทยาลัย

วิทยานิพนธ์นี้เป็นส่วนหนึ่งของการศึกษาตามหลักสูตรปริญญาวิทยาศาสตรดุษฎีบัณฑิต

สาขาวิชาฟิสิกส์ ภาควิชาฟิสิกส์

คณะวิทยาศาสตร์ จุฬาลงกรณ์มหาวิทยาลัย

ปีการศึกษา 2553

ลิขสิทธิ์ของจุฬาลงกรณ์มหาวิทยาลัย

THERMOELECTRIC PROPERTIES OF IRON SILICIDE SYNTHESIZED BY  
THERMAL METHOD



Miss Aparporn Sakulkalavek

ศูนย์วิทยทรัพยากร  
จุฬาลงกรณ์มหาวิทยาลัย

A Dissertation Submitted in Partial Fulfillment of the Requirements  
for the Degree of Doctor of Philosophy Program in Physics

Department of Physics

Faculty of Science

Chulalongkorn University


Academic Year 2010

Copyright of Chulalongkorn University

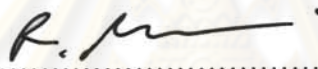
Thesis Title                                    THERMOELECTRIC PROPERTIES OF IRON SILICIDE  
SYNTHESIZED BY THERMAL METHOD  
By    Miss Aparporn Sakulkalavek  
Field of Study                                  Physics  
Thesis Advisor                                Assistant Professor Somchai Kiatgamolchai, Ph.D.

---

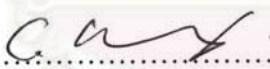
Accepted by the Faculty of Science, Chulalongkorn University in Partial Fulfillment  
of the Requirements for the Doctoral Degree


  
..... Dean of the Faculty of Science  
(Professor Supot Hannongbua, Dr.rer.nat.)

THESIS COMMITTEE

  
..... Chairman  
(Assistant Professor Rattachat Mongkolnavin, Ph.D.)

  
..... Thesis Advisor  
(Assistant Professor Somchai Kiatgamolchai, Ph.D.)

  
..... Examiner  
(Chatchai Srinitiwara Wong, Ph.D.)

  
..... Examiner  
(Somrit Wongmanerod, Ph.D.)

  
..... External Examiner  
(Associate Professor Supakorn Pukird, Ph.D.)

อาณาจักร สกฤตการะเวก : สมบัติเทอร์มออิเล็กทรอนิกส์ของไอร์ออนซิลิไซด์ที่สังเคราะห์โดย  
กระบวนการความร้อน (THERMOELECTRIC PROPERTIES OF IRON SILICIDE  
SYNTHESIZED BY THERMAL METHOD) อ.ที่ปรึกษาวิทยานิพนธ์หลัก: ผศ.ดร.  
สมชาย เกียรติกมลชัย, 88 หน้า.

สารประกอบเหล็ก-ซิลิกอนซึ่งมีอัตราส่วนอะตอมของเหล็กต่อซิลิกอนเป็น 1:2.0, 1:2.3  
และ 1:2.5 ถูกสังเคราะห์โดยกระบวนการความร้อน สารตัวอย่างทั้งหมดถูกอบที่อุณหภูมิ 820  
องศาเซลเซียส หรือ 950 องศาเซลเซียส เป็นเวลา 3, 6 และ 12 ชั่วโมง ในบรรยากาศของอาร์กอน  
เมื่อระยะเวลาในการอบมากขึ้นพบว่าค่าสัมประสิทธิ์ซีเบคมากขึ้นแต่โครงสร้าง  $\epsilon$  ยังปรากฏใน  
สารตัวอย่าง  $\text{FeSi}_{2.0}$  และ  $\text{FeSi}_{2.3}$  จากส่วนเบี่ยงเบนมาตรฐานของค่าสัมประสิทธิ์ซีเบคที่วัดโดยวิธี  
หัววัดร้อนพบว่า สารตัวอย่าง  $\text{FeSi}_{2.0}$  และ  $\text{FeSi}_{2.3}$  มีโครงสร้างที่ไม่สม่ำเสมอมากกว่าสาร  
ตัวอย่าง  $\text{FeSi}_{2.5}$  อิทธิพลของซิลิกอนส่วนเกินต่อสมบัติทางเทอร์มออิเล็กทรอนิกส์พบว่า  
ค่าสัมประสิทธิ์ซีเบคเพิ่มขึ้น และสภาพนำความร้อนลดลงเนื่องจากการกระเจิงของโฟนอนและ  
พาหะโดยซิลิกอนส่วนเกิน โดยเฉพาะที่อุณหภูมิต่ำกว่า 400 องศาเซลเซียส สมบัติทางเทอร์มอ  
อิเล็กทรอนิกส์ ได้แก่ ค่าสัมประสิทธิ์ซีเบค ค่าสภาพนำความร้อน และค่าสภาพนำไฟฟ้าถูกวัดเทียบกับ  
อุณหภูมิตั้งแต่ 30 องศาเซลเซียส ถึง 700 องศาเซลเซียส การกระจายของซิลิกอนส่วนเกินในสาร  
ตัวอย่าง  $\text{FeSi}_{2.3}$  และ  $\text{FeSi}_{2.5}$  ทำให้ค่าสัมประสิทธิ์ซีเบคเพิ่มขึ้น และค่าสภาพนำความร้อนลดลง  
ในขณะที่การคงอยู่ของโครงสร้าง  $\epsilon$  ในสารตัวอย่าง  $\text{FeSi}_{2.0}$  และ  $\text{FeSi}_{2.3}$  ทำให้สภาพนำไฟฟ้า  
เพิ่มขึ้น ค่าสูงสุดของ ZT ของสารตัวอย่าง  $\text{FeSi}_{2.0}$ ,  $\text{FeSi}_{2.3}$  และ  $\text{FeSi}_{2.5}$  ซึ่งถูกอบที่อุณหภูมิ 950  
องศาเซลเซียส นาน 12 ชั่วโมง คือ 0.44, 0.48 และ 0.20 ตามลำดับ วัดที่อุณหภูมิ 700 องศา  
เซลเซียส

ศูนย์วิทยทรัพยากร  
จุฬาลงกรณ์มหาวิทยาลัย

ภาควิชา ฟิสิกส์  
สาขาวิชา ฟิสิกส์  
ปีการศึกษา 2553

ลายมือชื่อนิสิต อาภาภรณ์ สกฤตการะเวก  
ลายมือชื่อ อ.ที่ปรึกษาวิทยานิพนธ์หลัก S. Kiatgandehai

## 4973864923 : MAJOR PHYSICS

KEYWORDS : THERMOELECTRIC MATERIAL /  $\beta$ -FeSi<sub>2</sub> / THERMAL METHOD

APARPORN SAKULKALAVEK : THERMOELECTRIC PROPERTIES OF IRON SILICIDE SYNTHESIZED BY THERMAL METHOD. ADVISOR: ASST. PROF. SOMCHAI KIATGAMOLCHAI, Ph.D., 88 pp.

The Fe-Si compound with atomic ratio Fe:Si = 1:2.0, 1:2.3 and 1:2.5 were synthesized by thermal method. All samples were annealed at 820 °C or 950 °C for 3, 6 and 12 h in Ar atmosphere. Longer annealing time increased Seebeck coefficient but  $\epsilon$ -FeSi phase still presented in FeSi<sub>2.0</sub> and FeSi<sub>2.3</sub> samples. Based on standard deviation of Seebeck coefficient measured by hot-probe technique, it would imply that non-homogeneity in FeSi<sub>2.0</sub> and FeSi<sub>2.3</sub> samples was higher than that in FeSi<sub>2.5</sub> sample. Influences of excess Si on thermoelectric properties were investigated. It was shown that the Seebeck coefficient increased and thermal conductivity decreased due to the phonon and carriers scattering by excess Si, especially at lower temperatures than 400 °C. Thermoelectric properties, Seebeck coefficient, thermal conductivity and electrical conductivity were measured as a function of temperature (30 °C < T < 700 °C). The dispersion of excess Si in FeSi<sub>2.3</sub> and FeSi<sub>2.5</sub> samples increased the Seebeck coefficient and decreased the thermal conductivity while the present of metallic  $\epsilon$ -phase in FeSi<sub>2.0</sub> and FeSi<sub>2.3</sub> samples increased the electrical conductivity. The highest dimensionless figure of merit  $ZT$  for FeSi<sub>2.0</sub>, FeSi<sub>2.3</sub> and FeSi<sub>2.5</sub> were annealed at 950 °C for 12 h were 0.44, 0.48 and 0.20 at 700 °C, respectively.

Department : Physics.....

Student's Signature อภิภากรกุล สกคกร:๖๗

Field of Study : Physics.....

Advisor's Signature S.Kiatgamolchai

Academic Year : 2010.....

## Acknowledgements

I would like to express my gratitude to my thesis advisors, Assistant Professor Dr. Somchai Kiatgamolchai for his suggestion and advice throughout the course of this dissertation. I am also grateful to Assistant Professor Dr. Rattachat Mongkolnavin, Dr. Chatchai Srinitiwatwong , Dr. Somrit Wongmanerod and Associate Professor Dr. Supakorn Pukird for serving as the committee. All of whom have made valuable comments and have been helpful in the production of this dissertation.

I would like to thank department of physics, faculty of science, Chulalongkorn University. Many thanks to my friends who helped me in various way with their friendship and encouragement.

I would like to acknowledge the financial supports from Development and Promotion of Science and Technology talents project (DPST) and Graduate Thesis Grant, Chulalongkorn University.

Finally, a deep gratitude is acknowledged to my family for love, understanding and encouragement throughout the entire study.

ศูนย์วิทยทรัพยากร  
จุฬาลงกรณ์มหาวิทยาลัย

# Contents

	Page
<b>Abstract (Thai)</b> .....	iv
<b>Abstract (English)</b> .....	v
<b>Acknowledgements</b> .....	vi
<b>Contents</b> .....	vii
<b>List of Tables</b> .....	x
<b>List of Figures</b> .....	xi
<b>Chapter I Introduction</b> .....	1
1.1 Thermoelectric Material .....	1
1.2 Iron Disilicide (FeSi <sub>2</sub> ).....	5
1.3 Objectives .....	6
1.4 Research Methodology .....	7
<b>Chapter II Literature Review and Theory</b> .....	8
2.1 Literature Review .....	8
2.2 Heat and Charge.....	12
2.3 Thermoelectric Power or Seebeck Coefficient .....	14
2.4 Thermal Conductivity .....	16
2.4.1 Effects of Electronic Contribution on the Heat Conductivity..	17
2.4.2Effects of Lattice Contribution and Phonon Scattering Mechanism.....	19
2.5 Electrical Conductivity.....	21
2.6 The Efficiency and Figure of Merit of Thermoelectric Material.....	24
<b>Chapter III Experimental Method</b> .....	30
3.1 Consumable Material .....	30
3.2 High Temperature Furnace System .....	30
3.2.1 Gas Cylinder .....	30
3.2.2 Control Box .....	31
3.2.3 High Temperature Furnace .....	32

3.2.4 Pump.....	33
3.2.5 Crucible.....	33
3.3 The Procedures for Operating the High Temperature Furnace System.	34
3.4 Sample Preparation .....	34
3.5 Characterization Technique.....	36
3.5.1 X-Ray Powder Diffraction (XRD).....	36
3.5.2 Scanning Electron Microscope (SEM) .....	37
3.5.2.1 Backscattered Electrons (BSE).....	40
3.5.2.2 Secondary Electrons (SE).....	41
3.5.3 Thermal Analysis .....	42
3.5.4 Seebeck Coefficient and Electrical Resistance Measuring .....	44
3.5.4.1 Hot-probe Seebeck Coefficient Measurement .....	44
3.5.4.2 Seebeck Coefficient and Electrical Resistivity at High Temperature.....	45
3.5.5 Measurement of Thermal Properties .....	48
<b>Chapter IV Result and Discussion.....</b>	<b>53</b>
4.1 As- Grown Sample.....	53
4.2 Effect of Melting Temperature and Melting Time on the Grain Size of $\epsilon$ -Phase and Seebeck Coefficient.....	55
4.3 XRD and SEM Image of As-Grown Sample.....	56
4.4 DTA Measurement.....	61
4.5 Annealed Sample.....	64
4.5.1 SEM Image.....	64
4.5.2 XRD Pattern.....	67
4.6 Seebeck Coefficient.....	69
4.6.1 Seebeck Coefficient at Room Temperature.....	69
4.6.2 Temperature Dependence of Seebeck Coefficient.....	73
4.7 Electrical Conductivity.....	74
4.8 Thermal Conductivity.....	77
4.9 Figure of Merit.....	79



<b>Chapter V Conclusion.....</b>	<b>81</b>
<b>References.....</b>	<b>83</b>
<b>Vitae.....</b>	<b>88</b>



ศูนย์วิทยทรัพยากร  
จุฬาลงกรณ์มหาวิทยาลัย

## List of Tables

	Page
1.1 Bulk thermoelectric materials.....	3
2.1 Correspondence between thermal and electrical quantities.....	12
2.2. Definition of transport coefficients in thermoelectricity.....	13
2.3 Example of experimental values of $L$ at 0 °C and 100 °C for metals.....	18
3.1 Thermal Analysis Categories.....	42
4.1 EDS measurement for the as-grown samples.....	58
4.2. Summary of annealing temperature.....	61
4.3. EDS measurement of the annealed samples.....	64
4.4. Summary of Seebeck coefficient at room temperature of this work and other publication.....	70

  
 ศูนย์วิจัยทรัพยากร  
 จุฬาลงกรณ์มหาวิทยาลัย

## List of Figures

	Page
1.1 The number of papers on thermoelectric materials published as a function of year from 1955 to 2007.....	1
1.2 $ZT$ of many typical thermoelectric materials as a function of year .....	4
1.3 Crystal structure of Fe-Si.....	5
1.4 The equilibrium phase diagram of Fe – Si system.....	6
2.1 Categories of bulk $\beta$ -FeSi <sub>2</sub> synthesis.....	8
2.2 Free electron diffuse from the high temperature end to the low temperature	15
2.3 The conduction of heat from the hot to the cold surface.....	17
2.4 Temperature dependence of mobilities due to lattice and impurity scattering in n-type Si for different electron concentration.....	22
2.5. Carrier concentration as a function of reciprocal temperature showing the intrinsic region, saturation region and ionization region.....	23
2.6 The components of thermoelectric generator.....	24
2.7 The maximum thermoelectric efficiency as function of $T_h$ with a cold side temperature $T_c = 30$ °C for different constant $ZT$ .....	27
2.8 $ZT$ value of thermoelectric material.....	28
2.9 Seebeck coefficient ( $S$ ), electrical conductivity ( $\sigma$ ), $S^2\sigma$ , and electronic ( $k_{el}$ ) and lattice ( $k_{ph}$ ) thermal conductivity as a function of free-carrier concentration ( $n$ ).....	29
3.1 The gas cylinder and gas regulators.....	31
3.2 The control box system.....	31
3.3 The high temperature furnace.....	32
3.4 Schematic drawing of the furnace.....	32
3.5 Alumina crucible and cover coated with boron nitride releasing agent.....	33
3.6 Process to operate the melt the Fe and Si powderAs-grown FeSi <sub>x</sub> sample....	35
3.7 Precision diamond saw (LECO, VC-50).....	35
3.8 X-ray diffraction from atoms in a crystalline material.....	36
3.9 The scanning electron microscope components.....	38

3.10 Cross sections of a electron lens. The electron path through the lens is helical. Electron further from the optical axis undergoes greater deflection.....	39
3.11 Photon and charge particle emission from electrons beam strikes a sample.....	39
3.12 Schematics show the excitation volume: (a) vary accelerating voltage and (b) vary atomic number of the material.....	40
3.13 An example of EDS spectrum of Fe-Si compound.....	41
3.14 DTA system.....	43
3.15 DTA curve show endothermic and exothermic peak.....	44
3.16 Schematic of Seebeck measurement method.....	45
3.17 The voltage- $T_H$ plot and the slope is Seebeck coefficient.....	45
3.18 Diagram of high temperature electrical resistivity measurement.....	46
3.19 Diagram of high temperature Seebeck coefficient measurement.....	47
3.20 The commercial equipment (ZEM-3, Ulvac, Inc.).....	47
3.21 Principles of flash method.....	49
3.22 Relationship between $\Gamma(L,t)$ and $\eta$ .....	50
3.23 A schematic diagram of the laser flash unit.....	51
4.1 As-grown $FeSi_x$ sample.....	53
4.2 Cross section of $FeSi_x$ after cutting by precision diamond saw, (a) before polishing and (b) after polishing by sandpaper. They were prepared for XRD and SEM measurement.....	54
4.3 Bar shape of $FeSi_x$ after cutting by precision diamond saw prepared for electrical resistivity and Seebeck coefficient measurement.....	54
4.4 Disk shape of $FeSi_x$ after cutting by precision diamond saw prepared for thermal diffusivity measurement.....	54
4.5 30x SEM micrograph of $FeSi_{2.3}$ melted at (a) 1450 °C and (b) 1550 °C for 1 h. $\alpha$ -phase surrounding the $\epsilon$ -phase in lighter color than that of $\alpha$ -phase matrix.....	55

4.6 The Seebeck coefficient of the as-grown samples melted at 1550 °C for 1 and 2 h.....	57
4.7 Seebeck coefficient of the as-grown samples melted for 1 h at 1450 °C and 1550°C.....	57
4.8 XRD patterns of as-grown FeSi <sub>2.0</sub> , FeSi <sub>2.3</sub> and FeSi <sub>2.5</sub> samples.....	59
4.9 Surface morphology of FeSi <sub>2.0</sub> , FeSi <sub>2.3</sub> and FeSi <sub>2.5</sub> samples are observed by SEM.....	60
4.10 DTA curves of as-grown (a) FeSi <sub>2.0</sub> , (b) FeSi <sub>2.3</sub> and (c) FeSi <sub>2.5</sub> samples.....	63
4.11 SEM image of FeSi <sub>2.0</sub> sample annealed for 6 h at (a) 820 °C and (b) 950 °C.....	65
4.12 SEM image of FeSi <sub>2.3</sub> sample annealed at 820 °C for 18 h and at 950 °C for 12 h.....	66
4.13 SEM image of FeSi <sub>2.5</sub> sample annealed at 950 °C for 6.....	67
4.14 XRD patterns of FeSi <sub>2.3</sub> sample annealed at 820 °C for 6 h.....	67
4.15 XRD patterns of (a) FeSi <sub>2.0</sub> , (b) FeSi <sub>2.3</sub> and (c) FeSi <sub>2.5</sub> samples annealed at 950 °C for 6 h.....	68
4.16 The volume fraction of ε-phase of annealed FeSi <sub>2.0</sub> , and FeSi <sub>2.3</sub> samples...	71
4.17 Seebeck coefficient of FeSi <sub>2.0</sub> , FeSi <sub>2.3</sub> samples annealed at 820 °C for different time.....	71
4.18 Seebeck coefficient of FeSi <sub>2.0</sub> , FeSi <sub>2.3</sub> and FeSi <sub>2.5</sub> samples annealed at 950 °C for different time.....	72
4.19 Schematic illustration of β-phase formation process.....	73
4.20 Temperature dependence of Seebeck coefficient of FeSi <sub>2.0</sub> , FeSi <sub>2.3</sub> and FeSi <sub>2.5</sub> .....	74
4.21 Temperature dependence of electrical conductivity of FeSi <sub>2.0</sub> , FeSi <sub>2.3</sub> and FeSi <sub>2.5</sub> .....	74
4.22 log σ versus 1000/T for temperature dependent conductivity .....	75

4.23 The calculation of energy gap from slope at high temperature of $\log \sigma - \frac{1000}{T}$ plots of (a) $\text{FeSi}_{2.0}$ , (b) $\text{FeSi}_{2.3}$ and (c) $\text{FeSi}_{2.5}$ .....	76
4.24 Temperature dependence of thermal conductivity of $\text{FeSi}_{2.0}$ , $\text{FeSi}_{2.3}$ and $\text{FeSi}_{2.5}$ .....	78
4.25 Temperature dependence of $K_{el}$ and $K_{ph}$ of $\text{FeSi}_{2.0}$ , $\text{FeSi}_{2.3}$ and $\text{FeSi}_{2.5}$ .....	78
4.26 Temperature dependence of dimensionless figure of merit of $\text{FeSi}_{2.0}$ , $\text{FeSi}_{2.3}$ and $\text{FeSi}_{2.5}$ .....	80



ศูนย์วิทยทรัพยากร  
จุฬาลงกรณ์มหาวิทยาลัย

# CHAPTER I

## INTRODUCTION

Owing to recent environmental and energy problems, conversion of waste heat to electricity has recently become greatly important. The development of thermoelectric material has facilitated the compatibility of thermoelectric devices with various kind of low grade unused heats, such as industrial waste heats, vehicular exhaust heat, solar heat and geothermal heat.

### 1.1 Thermoelectric Material

The term of thermoelectric material is referred to a material which exhibits substantial thermoelectric effects. Apart from superconductors, every material exhibits some degree of thermoelectric effects. For superconducting materials, electrical current flows without driving force. The thermoelectric effect is a direct conversion of temperature difference to electric voltage and vice versa. Thomas Seebeck discovered the thermoelectric effect in solid material in 1823 when he noticed that a voltage difference occurs across a material with a temperature gradient. However, like many other discoveries, it took many years to find useful applications and materials for this discovery. In the 1950s, Abraham Ioffe showed that doped semiconductors showed much larger thermoelectric effect than other materials. This led to research of binary semiconductors  $\text{Bi}_2\text{Te}_3$  as thermoelectric material. It has the greatest thermoelectric effect at room temperature.

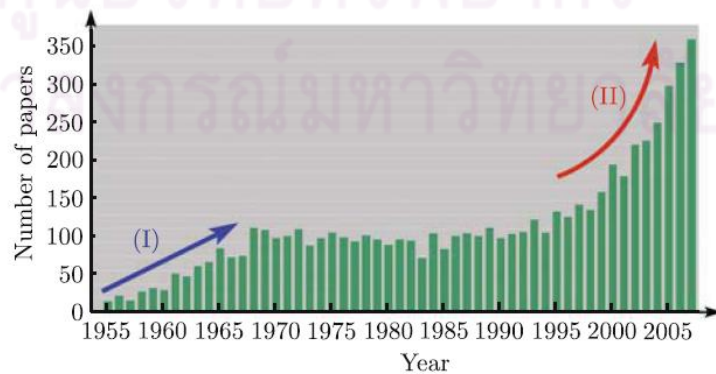


Figure 1.1: The number of papers on thermoelectric materials published as a function of year from 1955 to 2007 [1].

The efficiency of the thermoelectric conversion is directly related to the temperature difference over which the device operates, its average temperature of operation and the transport properties of the thermoelectric represented by  $ZT$ , the dimensionless figure of merit. The larger the  $ZT$  value, the larger the efficiency. The figure of merit,  $Z$ , is determined by

$$Z = \frac{S^2}{\rho K} \quad (1.1)$$

where  $S$  is the thermoelectric power or Seebeck coefficient,  $\rho$  is the electrical resistivity and  $K$  is the thermal conductivity. It is clear from this equation that in order to obtain a high figure of merit, a large Seebeck coefficient and low electric resistivity is required, as well as a low thermal conductivity. Low electrical resistivity is necessary to minimize Joule heating. Low thermal conductivity helps to retain heat at the junctions and to maintain a large temperature gradient.

The discovery of thermoelectric materials started from simple material; semiconductor such as group III-V, group IV-IV and group IV chalcogenides. Table 1.1 shows examples of bulk thermoelectric material classes.

Chalcogenides refers to sulfides, selenides and tellurides. These compounds often show semiconducting behavior [5], which can be suitable for operation over a wide range of temperatures (30 – 1130 °C) [6]. Nowadays in markets, Chalcogenides are the most common thermoelectric materials, such as  $\text{Bi}_2\text{Te}_3$ .  $\text{Bi}_2\text{Te}_3$  and its alloys are good thermoelectric materials at room temperature with  $ZT \approx 1$ . Venkatasubramanian *et al.* [7] reported that p-type  $\text{Bi}_2\text{Te}_2/\text{Sb}_2\text{Te}_3$  may have the highest  $ZT$  of about 2.4 at room temperature as shown in Fig.1.2. Problems with tellurium arise, since it is scarce, toxic and volatile at high temperatures. Therefore these of tellurium are limited [2].

Chalcogenides refers to sulfides, selenides and tellurides. These compounds often show semiconducting behavior [5], which can be suitable for operation over a wide range of temperatures (30 – 1130 °C) [6]. Nowadays in markets, Chalcogenides are the most common thermoelectric materials, such as  $\text{Bi}_2\text{Te}_3$ .  $\text{Bi}_2\text{Te}_3$  and its alloys are good thermoelectric materials at room temperature with  $ZT \approx 1$ . Venkatasubramanian *et al.* [7] reported that p-type  $\text{Bi}_2\text{Te}_2/\text{Sb}_2\text{Te}_3$  may have the highest  $ZT$  of about 2.4 at



room temperature as shown in Fig.1.2. Problems with tellurium arise, since it is scarce, toxic and volatile at high temperatures. Therefore these of tellurium are limited [2].

*Table 1.1 Bulk thermoelectric materials.*

Material class	Examples	Comments
IV	Si, SiGe	Generally poor thermoelectric properties[2]
V-chalcogenides	Bi <sub>2</sub> Te <sub>3</sub> , Sb <sub>2</sub> Te <sub>3</sub> , Bi <sub>2</sub> Se <sub>3</sub>	Can be both n- and p-type
IV-chalcogenides	PbTe, SnTe, GeTe	-
Skutterudites	MX <sub>3</sub> , (M = Co, Rh, Ir and X = P, As, Sb)	Very low thermal conductivity [2]
Calthrates	Sr <sub>8</sub> Ga <sub>16</sub> Ge <sub>30</sub> , Ba <sub>8</sub> Ga <sub>16</sub> Sn <sub>30</sub> , Ba <sub>8</sub> Ga <sub>16</sub> Sn <sub>30</sub>	-
Layered cobalt oxides [3]	CaCoO <sub>2</sub> , NaCoO <sub>2</sub>	Properties improve significantly with Ag doping, but still poor. [4]

Skutterudites and Calthrates are typical of phonon glass electron crystal (PGEC). The basic idea is to significantly reduce phonon scattering (similar with glass) but at the same time keep good electric conductivity (electron crystal) by introducing impurities known as rattler atoms into interstitial voids or cages of unit cell [8]. The rattle atom is heavy atom and its radius has to be smaller than the voids radius of the unit cell. The range for candidate filler element is decided by the ratio of ionic rattle atom radius

( $I_{rad}$ ) and void radius ( $V_{rad}$ ) [9] :  $0.67 \leq \frac{I_{rad}}{V_{rad}} \leq 1$ . When large voids are filled by rattle

atoms, they act as oscillators and thereby reduce the heat transport. The name of skutterudite comes from a naturally occurring with the CoAs<sub>3</sub>, first discovered in Skutterud, Norway. It is a cubic crystal structure with 32 atoms per unit cell. This

structure has 2 voids per unit cell. These voids can be filled by rattlers atom which can reduce thermal conductivity. Nolas and Slack [10] added La (1.79 Å), Nd (1.70 Å) and Sm (1.69Å) to the IrSb<sub>3</sub> binary skutterudite unit cell with a void radius of 2.04 Å. The result indicated that the thermal conductivity was reduced comparing to unfilled skutterudite. Calthrates compound also have the crystal structure that can host rattlers. Examples of this materials family are Sr<sub>8</sub>Ga<sub>16</sub>Ge<sub>30</sub>, Ba<sub>8</sub>Ga<sub>16</sub> Sn<sub>30</sub> and Ba<sub>8</sub>Ga<sub>16</sub>Sn<sub>30</sub>. Here Sr and Ba are the rattlers. Thermal conductivity value is very low (less than 1 W/m.K [11]). These materials are primarily n-type. Seebeck coefficient is in range -120 to -300 μV/K and resistivity range from 1 to 10 mΩ.cm at room temperature.

Finally, there is much work now developing thermoelectric oxides. The CaCoO<sub>2</sub> and NaCoO<sub>2</sub> are two of the most promising of this group [3]. Seebeck coefficient is in the range of 70 μV/K with resistivities near 10 mΩ.cm and thermal conductivity is about 7 W/mK at room temperature. Thermoelectric properties can be significantly improved with Ag doping [4].

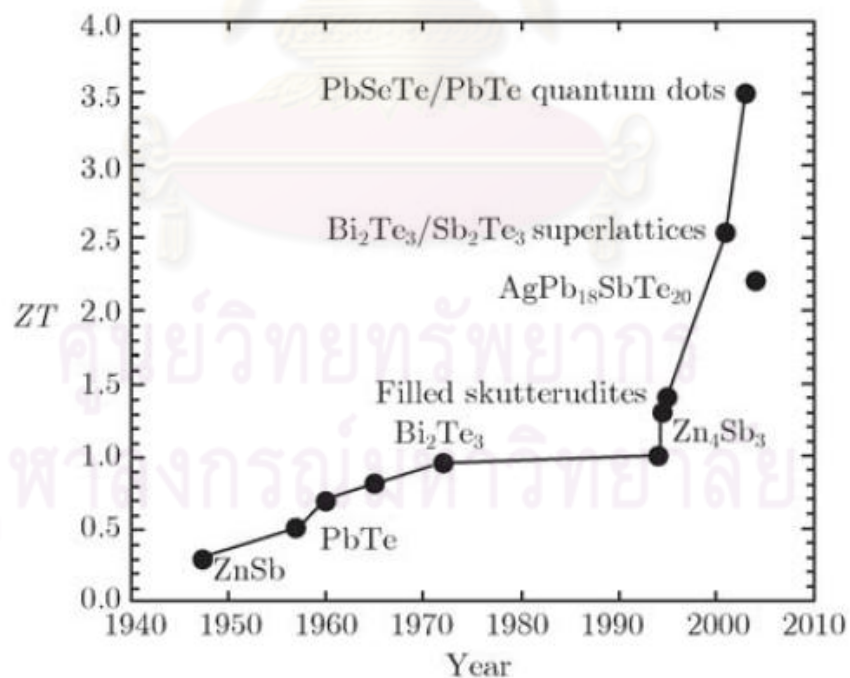


Figure 1.2: ZT of many typical thermoelectric materials as a function of year [12].

## 1.2 Iron Disilicide (FeSi<sub>2</sub>)

FeSi<sub>2</sub> is known for excellent high thermoelectric material that can be used in high temperature range (200 °C to 927 °C). It is also an environmentally friendly material because of the low toxicity of its constituent elements, Fe and Si. The material is good resistant against oxidation and can be operated in air without any protection [13,14].

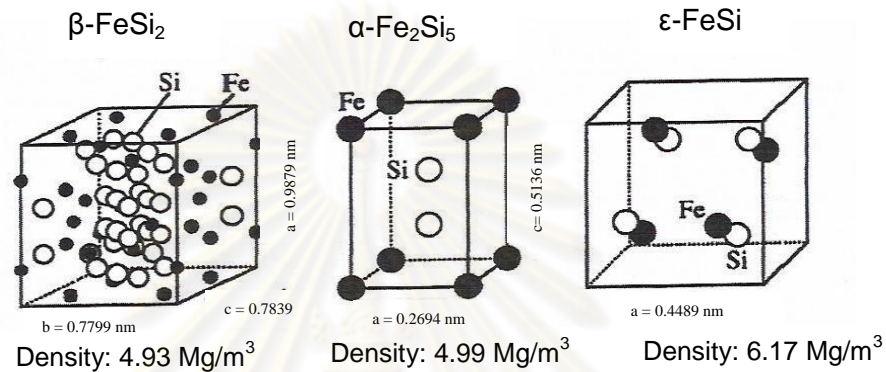


Figure 1.3: Crystal structure of Fe-Si [15].

The crystal structure of  $\epsilon$ -FeSi,  $\alpha$ -Fe<sub>2</sub>Si<sub>5</sub> and  $\beta$ -FeSi<sub>2</sub> are shown in Fig. 1.3.  $\epsilon$ -FeSi has a cubic structure with 8 atoms in a unit cell.  $\alpha$ -Fe<sub>2</sub>Si<sub>5</sub> has a tetragonal structure with 2.87 atoms in a unit cell and  $\beta$ -FeSi<sub>2</sub> presents an orthorhombic structure with 48 atoms in a unit cell [15]. The lattice constant of  $\beta$ -FeSi<sub>2</sub> are  $a = 9.863 \text{ \AA}$ ,  $b = 7.791 \text{ \AA}$  and  $c = 7.833 \text{ \AA}$  [16]. From the equilibrium phase diagram of the Fe-Si system, a series of intermetallic compounds could be formed. Within the limits of 49.7 to 50.8 at.% Si a homogeneous  $\epsilon$ -FeSi exists. High temperature  $\alpha$ -Fe<sub>2</sub>Si<sub>5</sub> phase has the homogeneity limit 70.0 to 72.4 at.% Si whereas the low temperature intermetallic compound  $\beta$ -FeSi<sub>2</sub> contains 68.3 at.% Si [16]. These high temperature phases are metallic and do not show high thermoelectric power. The  $\beta$ -FeSi<sub>2</sub> phase, which shows high thermoelectric power as a semiconductor phase, is formed by the following three reactions:

1. the peritectoid reaction ( $\alpha + \epsilon \rightarrow \beta$ ) at 982 °C,
2. the eutectoid reaction ( $\alpha \rightarrow \beta + \text{Si}$ ) at 937 °C, and
3. the subsequent reaction ( $\epsilon + \text{Si} \rightarrow \beta$ ) [17].

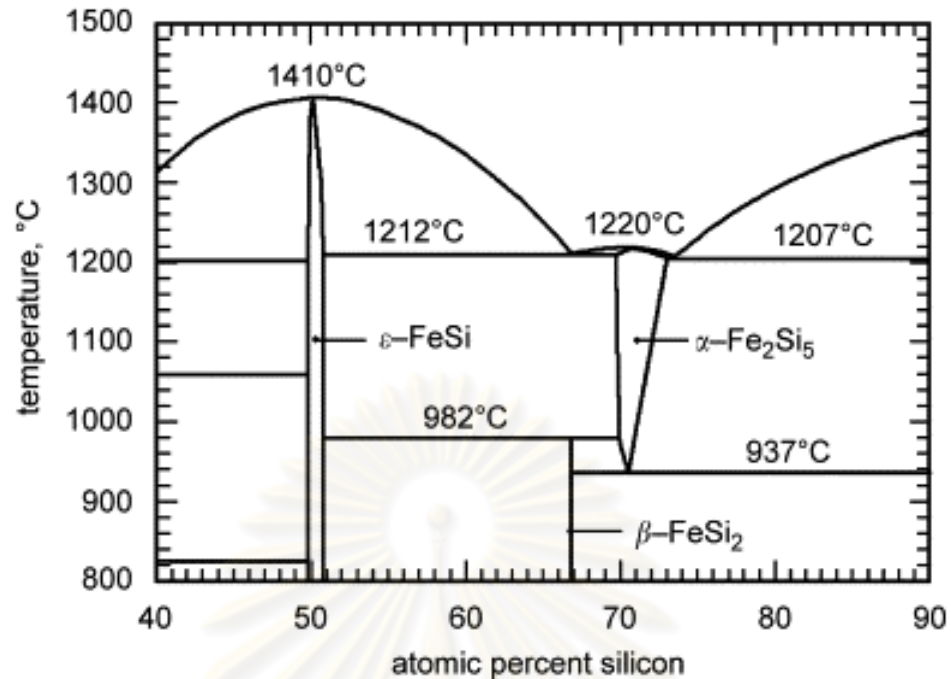


Figure 1.4: The equilibrium phase diagram of Fe – Si system [18].

### 1.3 Objectives

In this thesis, bulk  $\text{FeSi}_2$  will be synthesized and characterized. The objectives of this thesis are:

1. To synthesize  $\text{FeSi}_2$  by thermal method.
2. To assess and understand the key parameters and the conditions that accelerates the  $\beta$ -phase formation and densification.
3. To determine dimensionless figure of merit.

This thesis is divided into five chapters. Chapter 1 is an introduction of thermoelectric material where  $\text{FeSi}_2$  is also described. Chapter 2 describes the literature review of  $\text{FeSi}_2$  and theoretical background. Chapter 3 describes the sample preparation and characterization techniques. Results and discussions are described in Chapter 4. Finally, Chapter 5 concludes the achievement of the work.

## 1.4 Research Methodology

1. Modify the furnace for an inert-ambience heating process.
2. Prepare  $\text{FeSi}_x$ ,  $x = 2.0, 2.3$  and  $2.5$  in Ar atmosphere by melting at  $1550\text{ }^\circ\text{C}$  for 1 h. Sample will be ex-situ annealed, the sample is cooled down to room temperature and then heated up to required annealing temperatures and times, hold at these temperatures for 3, 6 and 12 h.
3. Measure the physical, thermal and electrical properties of the grown materials by following techniques:
  - 3.1 X-Ray diffraction (XRD)
  - 3.2 Scanning electron microscope (SEM)
  - 3.3 Differential thermal analysis (DTA)
  - 3.4 Thermal conductivity measurement by laser flash technique
4. Analyze the data and improve preparation method to obtain the optimized parameters, to achieve high content  $\beta\text{-FeSi}_2$ .

# CHAPTER II

## LITERATURE REVIEW AND THEORY

### 2.1 Literature Review

A bulk  $\text{FeSi}_2$  can be synthesized by many methods. From literature, they can be categorized into five groups:

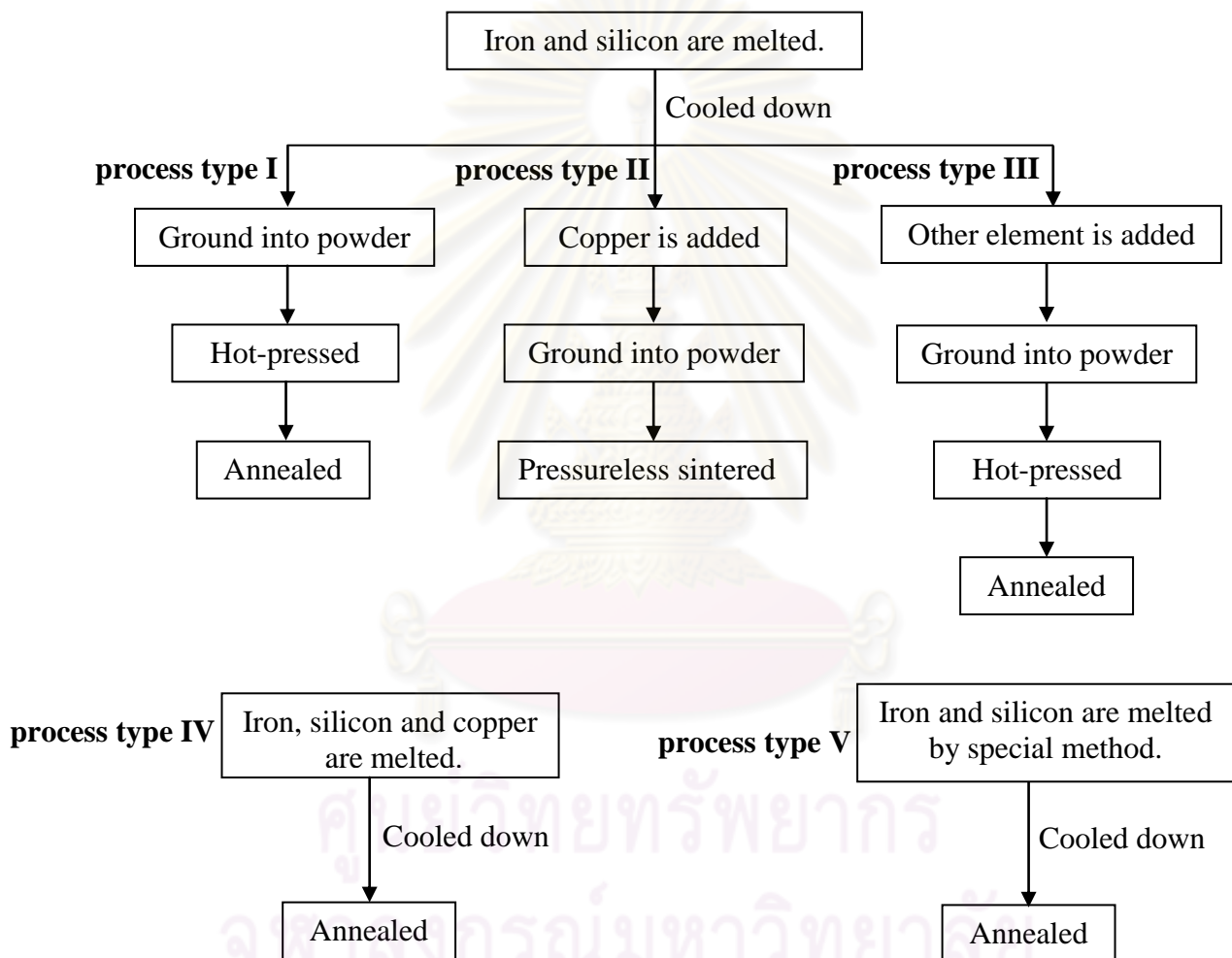


Figure 2.1: Categories of bulk  $\beta\text{-FeSi}_2$  synthesis.

**1. Type I process:** A mixture of iron and silicon powder is melted under an inert atmosphere, cooled down to room temperature, ground into fine powder, hot-pressed and annealed for  $\beta$ -phase formation [16, 19, 20]. As-grown alloy contained  $\alpha$ - and  $\varepsilon$ -phases which is then ground into fine powder by mechanical alloying (MA) process. MA is a ball milling where powder particles are trapped between colliding balls, causing them to be deformed and mixed. Umemoto *et al.* [16] suggested that at least 500 h of milling is required to induce  $\beta$ -FeSi<sub>2</sub> transformation by MA. Hot-pressing (HP) is used to improve the density of sample. The hot-pressing under vacuum with a pressure of 60 MPa for 4 h at 1100 °C yielded the sample density of 97% of the theoretical value but it still consisted of the untransformed mixture of  $\varepsilon$ - and  $\alpha$ -phase [20]. The sample still needs annealing for the  $\beta$ -phase transformation. Ur *et al.* [20] showed that the effective and economical way to produce  $\beta$ -FeSi<sub>2</sub> is approximately 24 h annealing at 830 °C after hot pressing at 1100 °C under 60 MPa for 4 h. Annealing at 1100 °C for 1 h produces  $\varepsilon$ - and  $\alpha$ -phases which is the decomposition of  $\beta$ -phase.

**2. Type II process:** A mixture of iron and silicon powder is melted, cooled down, added with copper powder, ground into fine powder by MA and pressureless sintered [21, 22]. In this process, copper powder is added to induce the liquid phase sintering. Melting of one element is effective enough for a densification of a sintered body due to rearrangement of the particles [23]. This technique will consume less energy than that of the HP technique. Ito *et al.* [22] added 1 mass% Cu into iron and silicon powder and showed that the liquid phase of Cu-Si formed around 802 °C. The Cu-Si liquid phase facilitates the supply of silicon atoms to the  $\varepsilon$ -phase for a subsequent reaction ( $\text{Si} + \varepsilon \rightarrow \beta$ ) because the liquid phase spreads through the grain boundary and particle interface. The final relative density of 93% was obtained for samples containing added copper. Pressureless sintering can be done at 1150 °C for 3 h. The disadvantage of using copper is that it can decrease the thermoelectric performance [21]. SEM image revealed that many small pores dispersed in the pressureless sintering sample and these pores effectively decreased thermal conductivity [21].

**3. Type III process:** A mixture of iron and silicon powder is melted, cooled down, other substance is added, ground into fine powder by MA, hot-pressed and annealed for  $\beta$ -phase formation.

For this process, the other substance is added to either accelerate the  $\beta$ -phase formation or to improved thermoelectric properties by reducing the thermal conductivity due to phonon scattering. Nagai *et al.* [24] added (Si+C) to  $\text{Fe}_{0.92}\text{Mn}_{0.08}\text{Si}_2$  during MA for 20 h under argon atmosphere and then hot-pressed at 900 °C for 1 h under 25 MPa in vacuum. They reported that small SiC particles about 20 nm in size dispersed in  $\beta$ -phase matrix. The thermal conductivity of the samples with 2 mass%(Si+C) was less than 5 W/m. K while it was more than 6 W/m. K for the sample without (Si+C). The maximum figure of merit was  $1.6 \times 10^4 \text{ K}^{-1}$  at 650 °C for  $\text{Fe}_{0.92}\text{Mn}_{0.08}\text{Si}_2$  with 2 mass%(Si+C). However, the thermal conductivity of SiC was 400-800 time higher than that of the  $\beta$ - $\text{FeSi}_2$  [25] and this will deteriorate the thermoelectric performance. Therefore, if a material with low thermal conductivity is finely dispersed as a second phase in the  $\beta$ -matrix, the thermal conductivity of  $\beta$ - $\text{FeSi}_2$  is expected to be further reduced.

Since it is difficult to get rid of  $\epsilon$ -phase in  $\text{FeSi}_2$  compound, a composition of  $\text{Fe}_2\text{Si}_5$  is preferred because it has no such phase. It is expected that excess Si particle from eutectoid reaction ( $\alpha \rightarrow \beta + \text{Si}$ ) will be dispersed in  $\beta$ -matrix [26]. Furthermore, the annealing time needed for  $\beta$ -phase formation can be largely reduced because of  $\epsilon$ -phase is not formed in the as-grown sample. Zhao *et al.* [27] reported that the free Si phase was the most important cause of the high Seebeck coefficient of  $\text{Fe}_2\text{Si}_5$  sample, especially at temperature range 25 °C – 300 °C. At high temperature, both number and mobility of charge carriers increase, so the influence of carrier scattering on Seebeck coefficient become insensitive. They predicted the Z of  $\text{Fe}_2\text{Si}_5$  would be higher than that of  $\text{FeSi}_2$  due to phonon scattering by Si dispersion in the sample.

**4. Type IV process:** A mixture of iron, silicon and copper is melted together and cooled down to room temperature. Yamauchi *et al.* [28] melted iron, silicon and copper powder together and cooled down to room temperature by slowly and rapidly solidified method. For slowly solidified alloy without Cu addition, differential thermal analysis (DTA) showed one sharp endothermic peak between 1000 °C and 1030 °C for all repeatedly heating process and this peak was equivalent to  $\beta$ -phase



decomposition to  $\varepsilon$ - and  $\alpha$ -phase. No reaction occurred for all repeatedly cooling process. For slowly solidified alloy with Cu addition, a large exothermic peak occurred at 630 °C during the first heating process and this peak was  $\beta$ -phase formation from peritectoid or eutectoid reactions. There were two endothermic peaks at 950 °C and 970 °C for all repeatedly heating process. These peaks corresponded to reverse reaction of eutectoid reaction ( $\beta + \text{Si} \rightarrow \alpha$ ) and peritectoid reaction ( $\beta \rightarrow \alpha + \varepsilon$ ), respectively. For all repeatedly cooling process, there was one sharp exothermic peak at 870 °C which is equivalent to eutectoid reaction ( $\alpha \rightarrow \beta + \text{Si}$ ). They showed that the addition of Cu accelerated  $\beta$ -phase formation especially in eutectoid reaction and the initial stage of the peritectoid reaction. The  $\beta$  transformation rate of 0.2 at% Cu added alloy was about 100 times higher than that of Cu-free alloy. The appropriate temperature for fast  $\beta$  formation may be located between 750 °C to 850 °C. The Seebeck coefficient of the  $\text{Fe}_{27.86}\text{Si}_{71.04}\text{Mn}_{1.0}\text{Cu}_{0.1}$  alloy was about 400  $\mu\text{V/K}$ , higher than the 290  $\mu\text{V/K}$  of a conventional  $\text{Fe}_{0.9}\text{Si}_{0.1}\text{Mn}_2$  alloy annealed at 800 °C for 2 h 25 min.

**5. Type V process:** A mixture of iron and silicon is melted by special method, cooled down and annealed for  $\beta$ -phase formation. Kakemoto *et al.* [29] prepared a bulk  $\beta$ - $\text{FeSi}_2$  by horizontal gradient freeze method from the melt material. They reported that the sample was homogeneous if it was melted at 1450 °C for 1 h. SEM image showed that the surface roughness was increased with decreasing Fe/Si due to Si segregation. Shibata *et al.* [30] reported that in-situ annealing at 800-900 °C directly after the melting could not start the peritectoid reaction ( $\alpha + \varepsilon \rightarrow \beta$ ) effectively. Kakemoto *et al.* [29] obtained single phase  $\beta$ - $\text{FeSi}_2$  bulk crystals by ex-situ annealing at 900 °C for 1000 h. Hsu *et al.* [31] used two-step Bridgman growth (TGB) with a three-zone furnace to synthesize bulk  $\beta$ - $\text{FeSi}_2$ . The results indicated that TGB quickly reduced the amount of  $\alpha$ -phase and the optimal annealing condition to yield high  $\beta$ -phase was between 800-900 °C for over 300 h.

For type I, II and III processes, bulk sample must be ground by MA technique that might be contaminative [32]. Although hot-pressing technique results in a sample with density close to the theoretical value but this technique uses lot of heat energy per sample [22].

In this thesis, I am interested in a simple method without element addition, short processing time and inexpensive process for the preparation of  $\beta$ -FeSi<sub>2</sub>. The ratios of Fe and Si powder will be selected as FeSi<sub>2.0</sub>, FeSi<sub>2.3</sub> and FeSi<sub>2.5</sub>. The mixtures of designated composition are melted and annealed in the same furnace. Seebeck coefficient, electrical conductivity and thermal conductivity are measured and analyzed.

## 2.2 Heat and Charge

In order to understand the thermoelectric effects, we shall start from the most fundamental concepts of heat and charge. Isolated objects at different temperatures, if brought into contact with each other, will exchange energy in an attempt to reach thermal equilibrium. A heat current density is the quantity of heat which passes through a boundary each second per unit area and thermal driving force is the change in temperature per unit distance, i.e. the temperature gradient. Similarly, objects with different electrical potentials, if brought into contact with each other, will exchange charge in an attempt for electrical equilibrium. An electrical current density is the quantity of electrical charges which passes through a boundary each second per unit area. An electrical driving force is the change in electrical potential per unit of distance, i.e. the electrical gradient.

**Table 2.1:** Correspondence between thermal and electrical quantities.

	<b>Thermal</b>	<b>Electrical</b>
Quantity	Heat	Charge
Potential	Temperature	Potential
Current Type	Thermal current density ( $\vec{Q}$ )	Electrical current density ( $\vec{j}$ )
Driving Force	Temperature difference	Potential difference

Ohm's law says that the electrical current density ( $\vec{j}$ ) will be proportional to the electrical driving force ( $-\vec{\nabla}V$ ) and the proportionality coefficient is called the electrical conductivity ( $\sigma$ ). Ohm's law is one example of a linear response. For thermoelectric problems of interest, linear response is an excellent approximation and

each of the thermoelectric properties may be defined by simple equations similar to Ohm's law. In table 2.2, the first relation connects the electrical current density to the electrical driving force while the second relation connects the thermal current density ( $\vec{Q}$ ) to the thermal driving force ( $-\vec{\nabla}T$ ). The electrical and thermal conductivity are therefore called direct effects since they connect currents density with the related driving force. The electrical conductivity indicates how well a material conducts electricity and thermal conductivity,  $K$ , indicates how well a material conducts heat. However, the Seebeck coefficient,  $S$ , and Peltier coefficient,  $\Pi$ , are called cross effects since they connect an electrical driving force to the thermal driving force or thermal current density to an electric current density. The cross effects are the basis for utilizing thermoelectric material for energy conversion applications. The Seebeck coefficient indicates how large a voltage difference a material generates in a temperature gradient and Peltier coefficient indicates how much heat passes through a material for a given electric density current.

*Table 2.2: Definition of transport coefficients in thermoelectricity.*

No.	Thermoelectric Property	Definition	Under Condition	Type
1	Electrical conductivity	$\vec{j} = -\sigma\vec{\nabla}V$	$\vec{\nabla}T = 0$	Direct
2	Thermal conductivity	$\vec{Q} = -K\vec{\nabla}T$	$\vec{j} = 0$	Direct
3	Seebeck coefficient	$-\vec{\nabla}V = S\vec{\nabla}T$	$\vec{j} = 0$	Cross
4	Peltier coefficient	$\vec{Q} = \Pi\vec{j}$	$\vec{\nabla}T = 0$	Cross

In order to include the cross effects into the currents under arbitrary gradients, we need to add the effects together;

$$\vec{j} = \sigma(-\vec{\nabla}V) + \sigma S(-\vec{\nabla}T) \quad (2.1)$$

$$\vec{Q} = \sigma\Pi(-\vec{\nabla}V) + K(-\vec{\nabla}T) \quad (2.2)$$

These expressions represent a generalization of Ohm's law. In general a driving force,  $-\vec{\nabla}V$  or  $-\vec{\nabla}T$ , can generate a current density,  $\vec{j}$  or  $\vec{Q}$ .

### 2.3 Thermoelectric Power or Seebeck Coefficient

When a thermal gradient is applied to a solid, it will be accompanied by an electric field in the opposite direction and was discovered by Thomas Seebeck in 1826. It is easiest to show this effect using a one-dimensional model. Consider a piece of material with a uniform concentration of charge carriers. One end is hot and the other end is cold. The material in a temperature gradient will develop a voltage between the hot end and the cold end. This is because the charge carriers at the hot end have, on average, more energy than the charge carriers at the cold end. So, they are moving faster from the hot end to the cold end. On the other hand, when extra carriers have collected on the cold end, carriers flow to the hot end because of the carrier density gradient. In the equilibrium situation, there is no net flow of charge carriers. A voltage is therefore developed between the hot and cold end. Finally, the potential difference ( $\Delta V$ ) across a piece of material is developed due to a temperature difference  $\Delta T$ . The absolute Seebeck coefficient is defined as

$$S = \frac{dV}{dT}. \quad (2.3)$$

By convention, the sign of  $S$  represents the potential of the cold side with respect to the hot side. If electrons diffuse from hot to cold end, then the cold side is negative with respect to the hot side and  $S$  is negative. In p-type semiconductor, on the other hand, hole would diffuse from the hot to the cold end. The cold side would be positive with respect to the hot side which would make  $S$  a positive quantity.

From equation (2.3), the potential difference is given by

$$\Delta V = \int_{T_0}^T SdT. \quad (2.4)$$

We assume that the conduction electrons in the metal behave as if they were free. This means that the density of state  $g(E) \propto E^{1/2}$ . The average energy  $E_{av}$  per electron in a metal is given by [33]

$$E_{av}(T) = \frac{3}{5} E_{F0} \left[ 1 + \frac{5\pi^2}{12} \left( \frac{k_B T}{E_{F0}} \right)^2 \right], \quad (2.5)$$

where  $E_{F0}$  is the Fermi energy at 0 K and  $k_B$  is Boltzmann's constant.

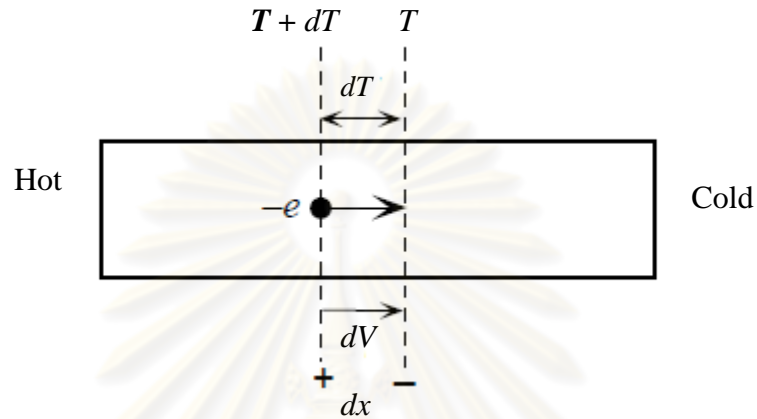


Figure 2.2: A free electron diffuses from the high temperature end to the low temperature end.

From Eq. (2.5), the average energy per electron in the hot end is greater than the cold end. Consequently the net electrons in the hot region diffuse toward the cold region as shown in Fig. 2.2. Consider a small length  $dx$  over which the temperature difference is  $dT$  and voltage difference is  $dV$ . Suppose that one electron diffuses from the hot region to the cold region. It has to do work against the potential difference  $dV$  which is  $-edV$ . This work done against  $dV$  decreases the average energy of the electron by  $dE_{av}$  from  $E_{av}(\text{hot})$  to  $E_{av}(\text{cold})$ ;

$$-edV = E_{av}(T + dT) - E_{av}(T). \quad (2.6)$$

Substituting for  $E_{av}(T)$  from equation (2.5) and expanding  $(T + dT)$

$$-edV = \frac{\pi^2 k_B^2}{4E_{F0}} \left[ (T + dT)^2 - (T)^2 \right]. \quad (2.7)$$

Neglecting  $dT^2$  term, we obtain

$$-edV \approx \frac{\pi^2 k_B^2 T dT}{2E_{F0}}. \quad (2.8)$$

Since  $S = dV/dT$ , the Seebeck coefficient is given by

$$S \approx -\frac{\pi^2 k_B^2 T}{2eE_{F0}}. \quad (2.9)$$

It is clear from Eq. (2.9) that  $S$  depends on temperature. It should be emphasized that Eq. (2.9) is based on an assumption that the conduction electrons in the material behave as if they were free. In reality, we have to consider the interactions of the carriers with ion core and lattice vibration. By including the scattering process, Mott and Jones [34] have derived the following expression for the Seebeck coefficient,

$$S \approx -\frac{\pi^2 k_B^2 T}{3eE_{F0}} \chi \quad (2.10)$$

where  $\chi$  is a numerical constant that depends on the material, such as  $\chi = -1.48$  for gold.

## 2.4 Thermal Conductivity

Heat transfer is due to a temperature difference. There are three modes of heat transfer; conduction, convection and thermal radiation. Heat conduction in solids is by phonons and free electrons. Heat transfer is energy transfer. Heat will be transferred from hot to cold surfaces and this phenomenon is known as the conduction of heat. In a steady state, a linear temperature profile is established in the solid and the rate of heat transfer,  $Q$ , is observed to be proportional to the temperature difference between the two surfaces ( $T_H - T_C$ ) and the surface area of the plate,  $A$ , and inversely proportional to the thickness of the plate,  $X$ :

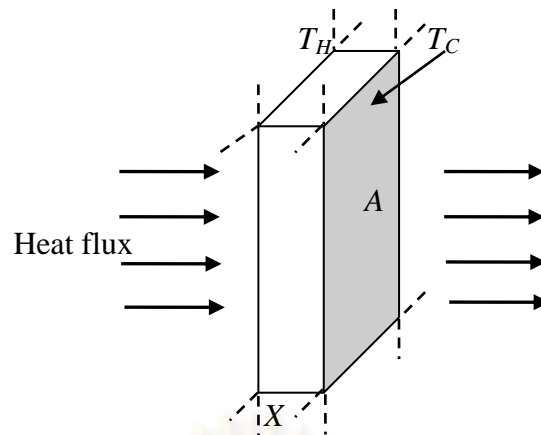


Figure 2.3: The conduction of heat from the hot to the cold surface.

$$Q \propto A \frac{T_H - T_C}{X} . \quad (2.11)$$

The above expression reduces to the following equation as the thickness of the plate approaches an infinitesimally small value;

$$q(x,t) = \frac{Q}{A} = -K \frac{dT(x,t)}{dx} \quad (2.12)$$

where  $q(x,t)$  is the heat flux [ $\text{W.m}^{-2}$ ],  $K$  is the thermal conductivity [ $\text{W.m}^{-2}.\text{K}^{-1}$ ] and  $T(x,t)$  is the temperature at position  $x$  and time  $t$ . Eq. (2.12) is referred to as Fourier's law of heat conduction. Thermal conductivity of material has two main components: the lattice (phonon component)  $K_{ph}$  and the electronic (or hole) component  $K_{el}$ .

$$K_{total} = K_{el} + K_{ph} . \quad (2.13)$$

#### 2.4.1 Effects of Electronic Contribution on the Heat Conductivity

In 1853, Wiedemann and Franz reported that at room temperature, the thermal conductivity of metal was proportional to the electrical conductivity. In 1872, Lorenz concluded that the ratio of thermal conductivity to electrical conductivity of pure metals is proportional to the absolute temperature, in the form of equation

$$\frac{K_{el}}{\sigma} = LT . \quad (2.14)$$

$L$  is the proportionality constant called “Lorenz number.” Eq. (2.14) is usually called the Wiedemann- Franz law. The value of theoretical Lorenz number is defined by assuming that the electrons do not interact with each other and the scattering of electrons is due to impurities or lattice vibrations and it is elastic [35]. The law of Wiedemann and Franz is valid at very low temperature (10 K) and high temperature ( $T \geq \theta_D$ , where  $\theta_D$  is Debye temperature) because in these regions the electrons are scattered elastically [35]. In 1927, Maxim [36] reported the value of theoretical Lorenz number to be

$$L = \frac{\pi^3}{3} \left( \frac{k_B}{e} \right)^2 = 2.45 \times 10^{-8} \text{ V}^2/\text{K}^2. \quad (2.15)$$

The law is satisfied for most metals within 10% at room temperature [37]. Experimental values of  $L$  at 0 °C and 100 °C are given in Table 2.3 and in good agreement with Eq. (2.15). For FeSi<sub>2</sub>, the Eq. (2.14) was used to calculate the  $K_{el}$  in temperature rang 30 °C – 900 °C. The value of  $K_{el}$  was less than 1 W/m/K and it increased with increasing temperature [21, 25].

**Table 2.3:** Example of experimental values of  $L$  at 0 °C and 100 °C for metals. [38].

Metal	$L \times 10^{-8} \text{ V}^2/\text{K}^2$		Metal	$L \times 10^{-8} \text{ V}^2/\text{K}^2$	
	0 °C	100 °C		0 °C	100 °C
Ag	2.31	2.37	Pb	2.47	2.56
Au	2.35	2.40	Pt	2.51	2.60
Cd	2.42	2.43	Sn	2.52	2.49
Cu	2.23	2.33	W	3.04	3.20
Mo	2.61	2.79	Zn	2.31	2.33



## 2.4.2 Effects of Lattice Contribution and Phonon Scattering Mechanism

A simple formula of lattice thermal conductivity based on classical kinetic theory of gases is

$$K_{ph} = \frac{1}{3} C_v \bar{d} \bar{v} \quad (2.16)$$

where  $C_v$  is the specific heat at constant volume,  $\bar{d}$  is the average phonon mean free path and  $\bar{v}$  is the average phonon velocity. At high temperature, above the Debye temperature,  $C_v$  in Eq. (2.16) approaches the classical value of  $3R$  where  $R$  is gas constant. At low temperature;  $C_v \propto T^3$ , law of Debye. However, since Eq. (2.16) is based on classical kinetic theory of gas, it is not valid for a wide range of materials. Then that lattice thermal conductivity, using the Callaway formalism, will be,

$$K_{ph} = \frac{k_B}{2\pi^2 v_s} \int_0^{\frac{\theta_D}{T}} \tau_c(x) \frac{x^4 e^x}{(e^x - 1)} dx \quad (2.17)$$

where  $\theta_D$  is Debye temperature,  $x = \frac{h\omega}{2\pi k_B T}$ ,  $\omega$  is phonon frequency and  $\tau_c$  is combined relaxation time.

$$\tau_c^{-1} = \tau_p^{-1} + \tau_D^{-1} + \tau_B^{-1} + \tau_{EP}^{-1} \quad (2.18)$$

where  $\tau_c^{-1}$  is combined mean free path,

$\tau_p^{-1}$  is mean free path depending on phonon-phonon scattering,

$\tau_D^{-1}$  is mean free path depending on point-defect scattering,

$\tau_B^{-1}$  is mean free path depending on grain boundary scattering and

$\tau_{EP}^{-1}$  is mean free path depending on electron-phonon scattering.

## Phonon Scattering Mechanism

### 1. Phonon-phonon Scattering

In real materials, one phonon does disturb all the other phonons. The resulting phonon-phonon scattering rate increase with increasing temperature because there are more phonon. This scattering is given by

$$\tau_c^{-1} \propto \omega^2. \quad (2.19)$$

The effect of phonon-phonon scattering to thermal conductivity, the temperature dependence is given by [39]

$$K_p \propto \exp\left[\frac{\theta_D}{2T} - 1\right]. \quad (2.20)$$

At high temperature, above Debye temperature, the thermal conductivity should be inversely proportional to temperature. As the temperature is lowered below the Debye temperature the thermal conductivity should rise exponentially until other scattering processes predominate.

### 2. Point defect scattering

A point defect is atom with difference from all of the others. A point defect is small and has little or no effect on long wavelength, low energy phonon. But short wavelength, high energy phonons are strongly scattered by point defects. For scattering by point defect

$$\tau_D^{-1} \propto \omega^4. \quad (2.21)$$

### 3. Phonon-charge carrier scattering

This interaction, both phonon and charge carriers will be scattered. At low temperature, long wavelength phonons can interact with all the charge carriers. But at high temperature, no charge carriers around to interact with phonon. So, the phonon-charge carrier scattering mechanism is much more effective at low temperature, long

wavelength phonons than it is at scattering high temperature, short wavelength phonon.

$$\tau_D^{-1} \propto \omega . \quad (2.22)$$

#### 4. Grain boundary scattering

Boundary scattering mainly affects the low frequency phonons and thus should not be important limitations at high temperature [40]

$$\tau_B^{-1} = \frac{v_s}{L}, \quad (2.23)$$

where  $v_s$  is the sound velocity and  $L$  is the characteristic length.

## 2.5 Electrical Conductivity

If there are  $n$  charge carrier per unit volume under a constant electric field  $\vec{E}$ , the electric current density  $\vec{j}$  is defined as

$$\vec{j} = \frac{ne^2\tau\vec{E}}{m} = \sigma\vec{E} \quad (2.24)$$

where  $\sigma$  is the electrical conductivity and  $\tau$  is a charge-carrier relaxation time which depends on the charge carrier scattering.

The electrical conductivity of a semiconductor is given by

$$\sigma = e(\mu_n n + \mu_p p) \quad (2.25)$$

where  $\mu_n$  and  $\mu_p$  refer to the mobilities of the electrons and holes, and  $n$  and  $p$  refer to the density of electrons and holes, respectively. A doped semiconductor, majority carriers greatly outnumber minority carriers, so that Eq. (2.25) can be reduced to a single term involving the majority carrier. Typical semiconductors can be described by accounting two charge-carrier scattering mechanisms, lattice scattering and impurity scattering. The mobility due to these scattering mechanisms is illustrated in Fig.2.4.

### 1. Lattice Scattering

Lattice scattering is a result of the thermal motion of the lattice atoms at temperatures above zero Kelvin. Lattice scattering becomes dominant at higher temperatures because the lattice vibrations increase with increasing temperature. A full theoretical analysis shows that the mobility due to lattice scattering varies as  $T^{-3/2}$  for a bulk material.

### 2. Impurity scattering

Impurity scattering comes from the ionized donor and acceptor impurities. A passing charge carrier will be deflected by the Coulomb force between it and the ion. The probability of impurity scattering depends on the doping density and the proportion of those atoms that are ionized. Impurity scattering becomes less significant with temperature since above a certain temperature, the impurity atoms will be ionized and also the charge carriers are moving faster and interact with the impurity for a shorter time. The variation of mobility due to impurity scattering decreases as  $T^{3/2} / N_T$ , where  $N_T$  is the total impurity concentration.

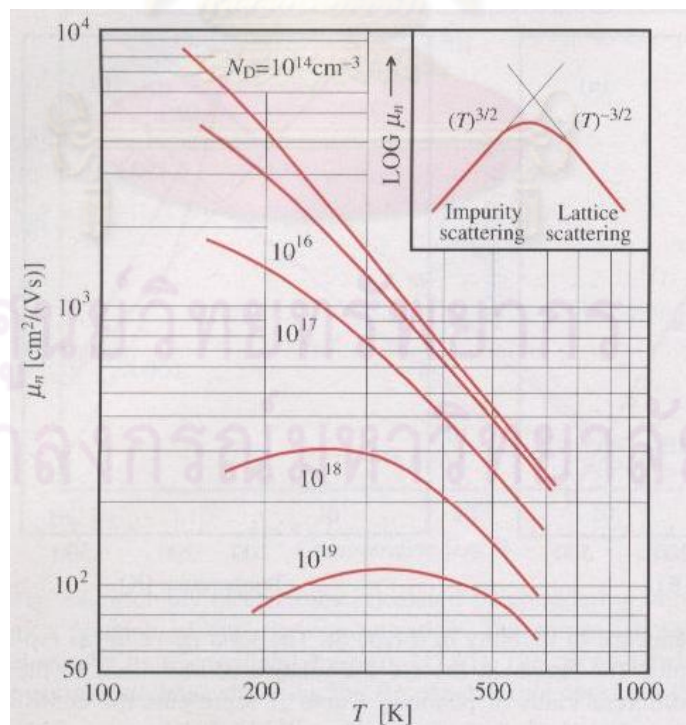


Figure 2.4: Temperature dependence of mobilities due to lattice and impurity scattering in n-type Si for different electron concentration [41].

The carrier concentration in a semiconductor is affected by temperature,  $n \propto \exp(-\frac{E}{k_b T})$  where  $E$  is the conductive energy and  $k_b$  is Boltzmann constant. At high temperature,  $E$  is the energy gap ( $E_g$ ) and at low temperature  $E$  is the activation energy of dopant ( $E_a$ ). The temperature dependence of carrier concentration can be seen in Fig. 2.5. At very low temperature (large  $1/T$ ), the carrier concentration is very small. As the temperature is raised, donor or acceptor atoms are increasingly ionized. When all are fully ionized, carrier concentrations become saturated. As the temperature is increased even further, the thermally generated intrinsic carriers outnumber the dopants. In this intrinsic region, carrier concentration increases with increasing temperature. In this case, only the influence of lattice scattering,  $\mu \propto T^{-3/2}$ , can be expected. For our high temperature measurement, electrical conductivity become

$$\sigma \propto \exp(-\frac{E_g}{k_b T}) \quad (2.26)$$

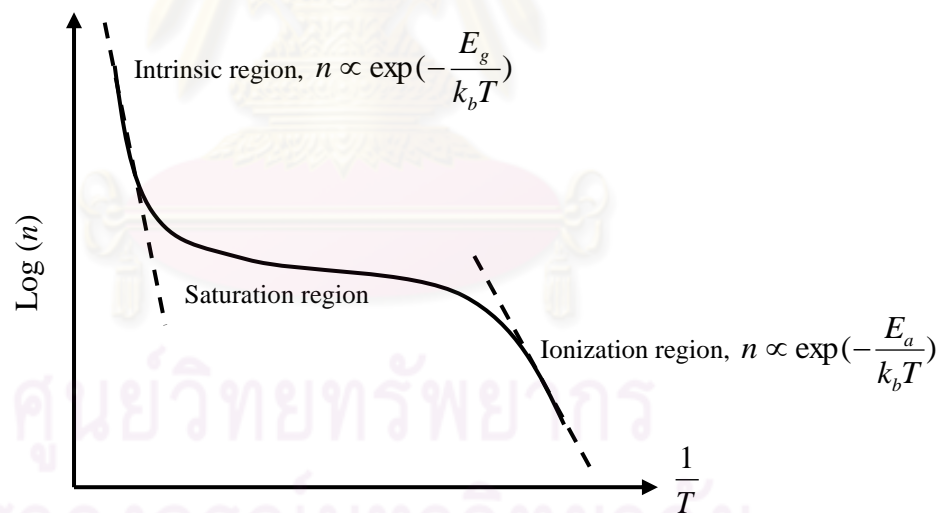


Figure 2.5: Carrier concentration as a function of reciprocal temperature showing the intrinsic region, saturation region and ionization region.

## 2.6 The Efficiency and Figure of Merit of Thermoelectric Material

In Fig. 2.6, an n-type and p-type thermoelectric material of length  $l$  are connected in thermal parallel and electrical series. Heat energy flux  $q$  is an input to this system.  $q$  is passed through the thermoelectric material by temperature difference driven.  $q_1$  and  $q_2$  are heat energy fluxes that come out of the system. The n-type and p-type thermoelectric material are connected by the conductor, which is assumed to have negligible electrical resistance and thermal resistance. A load resistor  $R$  is connected between the n-type and p-type.  $I$  is the generated currents.

The following assumptions are made for the calculation of the thermoelectric efficiency:

1.  $\rho_n = \rho_p = \rho$  over the temperature range  $T_c \leq T \leq T_h$ ,
2.  $K_n = K_p = K$  over the temperature range  $T_c \leq T \leq T_h$ ,
3.  $-S_n = S_p = S$  over the temperature range  $T_c \leq T \leq T_h$ ,
4.  $A_n = A_p = A$  is the cross section area of the thermoelectric materials,

where  $\rho$  is electrical resistivity ( $\Omega \cdot \text{m}$ ) and  $K$  is thermal conductivity ( $\text{W}/\text{m} \cdot \text{K}$ ).

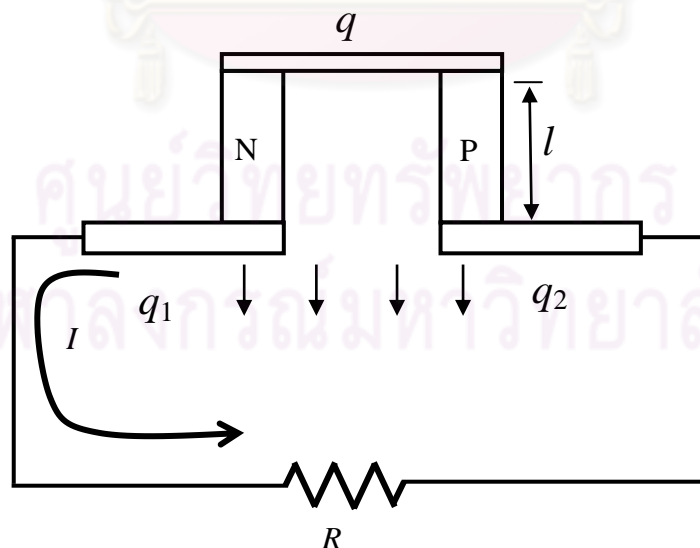


Figure 2.6: The components of thermoelectric generator.

Total internal electrical resistance ( $r$ ), thermal conductance ( $\delta$ ) and generated voltage ( $V$ ) can be calculated from following equation:

$$r = \frac{(\rho_n + \rho_p)l}{A} = \frac{2\rho l}{A} \quad (2.27)$$

$$\delta = \frac{(K_n + K_p)A}{l} = \frac{2KA}{l} \quad (2.28)$$

$$V = S(T_h - T_c) = S\Delta T \quad (2.29)$$

The electrical current and power delivered to the external load ( $R$ ) are,

$$I = \frac{S\Delta T}{r + R}, \quad (2.30)$$

$$P = I^2 R = \frac{S^2 \Delta T^2 R}{(r + R)^2}. \quad (2.31)$$

Following Ioffe [42], the input energy flux is the heat energy flux entering the hot junction and is given by

$$q = \delta\Delta T + ST_h I - \frac{I^2 r}{2}. \quad (2.32)$$

In a power generation device, the efficiency  $\eta$ , is defined as a dimensionless ratio of power output to heat energy flux absorbed at the hot junction

$$\eta = \frac{P}{q} = \frac{I^2 R}{\delta\Delta T + ST_h I - \frac{I^2 r}{2}}. \quad (2.33)$$

By defining  $m = \frac{R}{r}$  and using the expression for  $I$  from Eq. (2.29)

$$\eta = \frac{\Delta T}{T_h} \times \frac{\frac{m}{m+1}}{1 + \frac{\delta r(m+1)}{S^2 T_h} - \frac{\Delta T}{2T_h(m+1)}}. \quad (2.34)$$

By defining 
$$Z = \frac{S^2}{\delta r} = \frac{S^2}{\rho K} , \quad (2.35)$$

Eq. (2.33) becomes

$$\eta = \frac{\Delta T}{T_h} \times \frac{\frac{m}{m+1}}{1 + \frac{m+1}{ZT_h} - \frac{\Delta T}{2T_h(m+1)}} . \quad (2.36)$$

So this equation expresses the efficiency as a function of the hot and cold temperatures,  $T_h$  and  $T_c$  and the parameters  $m$  and  $Z$ . The maximum efficiency is found by  $\frac{d\eta}{dm} = 0$ .

$$\frac{d\eta}{dm} = \frac{\Delta T}{T_h} \left[ \frac{\left(1 + \frac{m+1}{ZT_h} - \frac{\Delta T}{2T_h(m+1)}\right) \left(\frac{1}{(m+1)^2}\right) - \left(\frac{m}{m+1}\right) \left(\frac{1}{ZT_h} + \frac{\Delta T}{2T_h(m+1)^2}\right)}{\left(1 + \frac{m+1}{ZT_h} - \frac{\Delta T}{2T_h(m+1)}\right)^2} \right] = 0 \quad (2.37)$$

$$\frac{1-m^2}{ZT_h} - \frac{\Delta T}{2T_h} + 1 = 0 \quad (2.38)$$

$$m^2 = 1 - \frac{Z\Delta T}{2} + ZT_h \quad (2.39)$$

$$m^2 = 1 + \frac{Z(T_h + T_c)}{2} \quad (2.40)$$

$$m = \sqrt{1 + ZT} \quad (2.41)$$

where  $T = \frac{T_h + T_c}{2}$

$$\eta_{\max} = \frac{\Delta T}{T_h} \times \frac{\sqrt{1 + ZT} - 1}{\sqrt{1 + ZT} + \frac{T_c}{T_h}} . \quad (2.42)$$

The maximum efficiency of the thermoelectric conversion is directly related to the temperature difference over which the device operates, its average temperature of operation and the transport properties of the thermoelectric represented by  $ZT$ , the dimensionless figure of merit. The larger the  $ZT$  value, the larger the efficiency.  $ZT$



value for p- and n-type thermoelectric materials are shown in Fig. 2.8. Each material class has its optimum temperature rang with high  $ZT$  values. For both p- and n-type of  $\beta$ -FeSi<sub>2</sub>, the maximum  $ZT$  value occurred at 570 °C ( $\approx$  850 K).

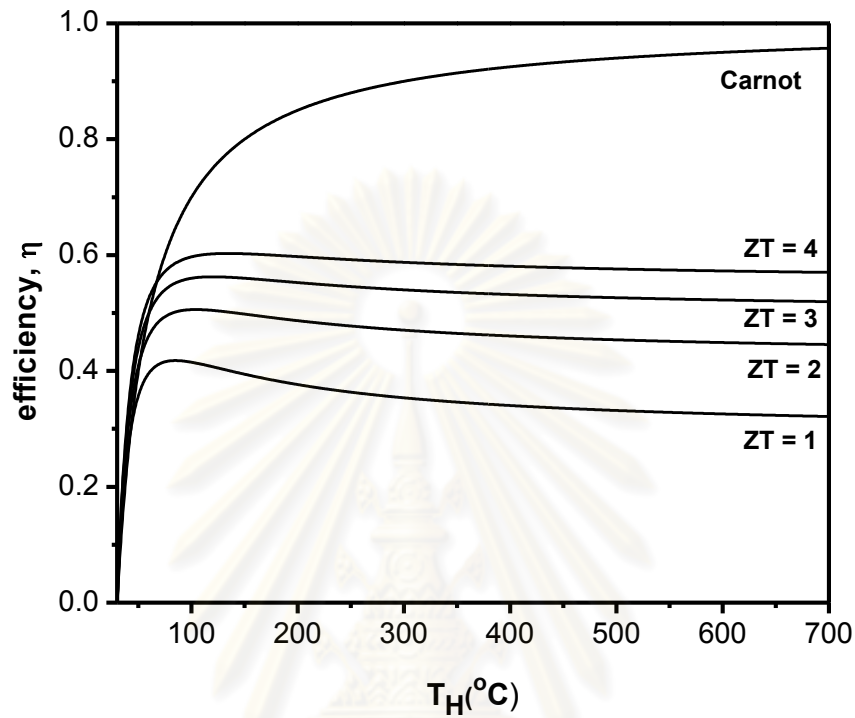
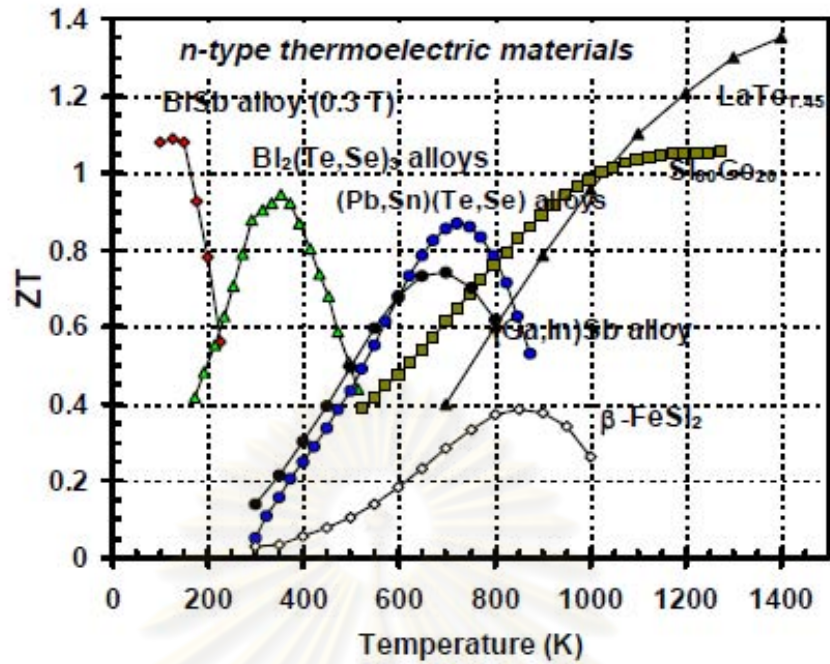
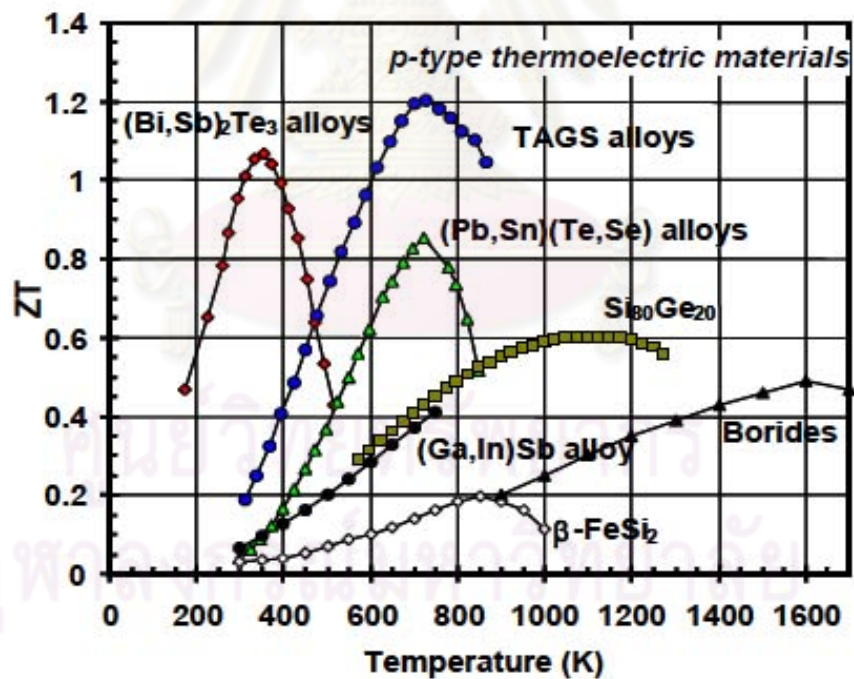


Figure 2.7: The maximum thermoelectric efficiency as function of  $T_h$  with a cold side temperature  $T_c = 30$  °C for different constant  $ZT$  .

ศูนย์วิทยทรัพยากร  
จุฬาลงกรณ์มหาวิทยาลัย



(a) n-type



(b) p-type

Figure 2.8: ZT value of thermoelectric material [43].

It is clear from Eq. 2.35 that in order to obtain a high figure of merit, a large Seebeck coefficient and low electric resistivity is required, as well as a low thermal conductivity. In the following figure, we present the variation of three parameters,  $S$ ,  $K$  and  $\sigma$ , against the carrier concentration,  $n$ . The  $ZT$  value reaches the maximum in the semiconductor region with carries concentration on the order of  $10^{19} - 10^{21} \text{ cm}^{-3}$ . For metals, they have good electrical conductivity and thermal conductivity but very low Seebeck coefficient. So, metals are not suitable to make thermoelectric materials.

On the other hand, for insulators, although they have large Seebeck coefficient but their electrical conductivity and thermal conductivity are extremely low. It is difficult to improve  $ZT$  because  $\sigma$ ,  $S$  and  $K$  are all coupled with each other. Moreover, they are strongly dependent on the material structure and carrier concentration.

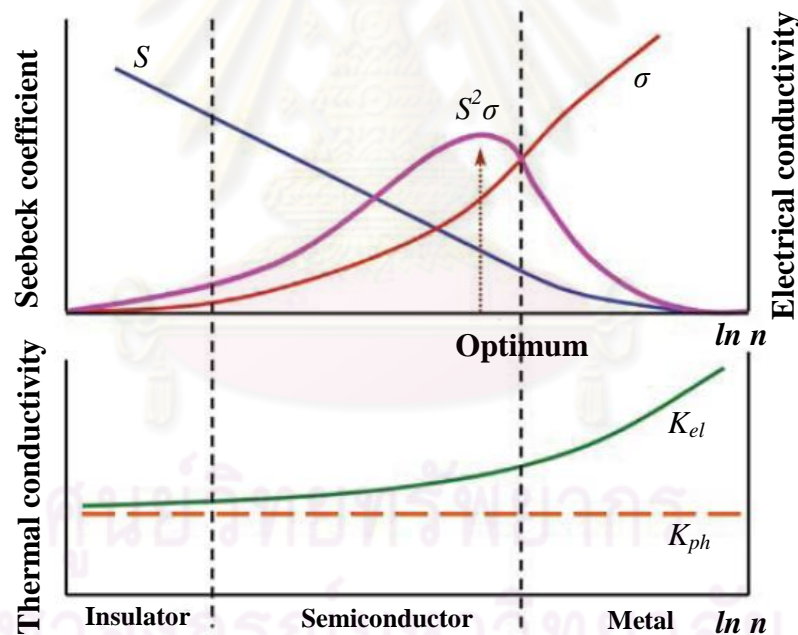


Figure 2.9: Seebeck coefficient ( $S$ ), electrical conductivity ( $\sigma$ ),  $S^2\sigma$ , and electronic ( $k_{el}$ ) and lattice ( $k_{ph}$ ) thermal conductivity as a function of free-carrier concentration ( $n$ ) [39, 42].

# CHAPTER III

## EXPERIMENTAL METHOD

In this chapter, we will describe the sample preparation method and characterization techniques. The high temperature furnace system is used to prepare and anneal the sample. We will explain the components and the procedures for operating the high temperature furnace system. For characterization techniques, XRD and SEM are used to check phase and Fe-Si composition in the sample both before and after annealing. DTA is used to obtain the qualitative information of  $\beta$ -phase formation. Physical properties need to be measured to examine the performance of materials. The parameters, including the Seebeck coefficient, electrical conductivity and thermal conductivity, can then be determined to calculate the dimensionless figure of merit,  $ZT$ . Hot-probe technique is used to measure the Seebeck coefficient at room temperature. Laser thermal flash technique is used to measure the thermal diffusivity and heat capacity. A commercial equipment (ZEM-3, Ulvac, Inc.) is used to measure the electrical resistivity and Seebeck coefficient from room temperature to 700 °C.

### 3.1 Consumable Material

The consumable materials used for experiments are listed as followed.

1. Silicon powder, 99% purity, of Sigma Aldrich, mesh size -325.
2. Iron powder, 99% purity, of Goodfellow, maximum powder size 60  $\mu\text{m}$ .
3. Boron nitride releasing agent.

### 3.2 High Temperature Furnace System

The high temperature furnace system composes of five sections which are (i) gas cylinder, (ii) control box, (iii) high temperature furnace, (iv) pump and (v) crucible with cover.

#### 3.2.1 Gas Cylinder

For this experiment, the Ar gas with high purity grade (TIG, 99.995%) is used to minimize oxidation. The gas cylinder is connected to the gas regulator. The gas

regulator reduces high pressure gas in the gas cylinder to lower, usable level as it passes to other part of system.



Figure 3.1: The gas cylinder and gas regulators.

### 3.2.2 Control Box

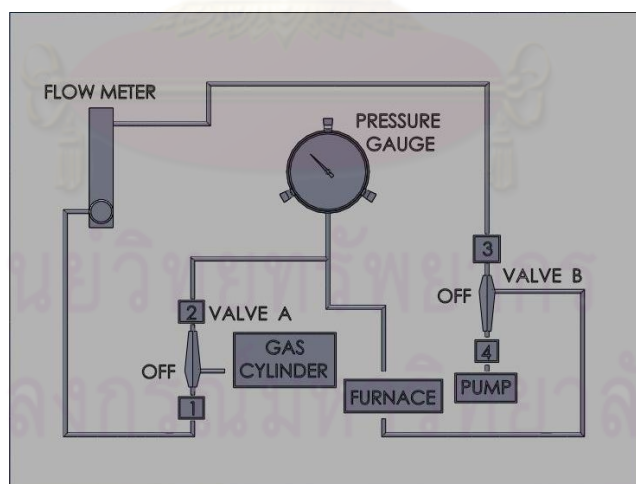


Figure 3.2: The control box system.

The control box composes of valve A, valve B, flow meter and pressure gauge. Valve A and valve B are three-way valve. Valve A can be in the following positions: OFF (Ar gas cannot flow to the system), 1 (Ar gas flow through the flow meter) or 2 (Ar

gas flow to the furnace). Valve B can be in the following positions: OFF (Ar gas cannot flow to the furnace), 3 (Ar gas flow through furnace) and 4 (air or Ar gas is pumped from the furnace). Flow meter measures the flow rate of Ar gas in the range 0 - 120 cc./min. We generally use 100 cc./min. Pressure gauge is used for measuring the pressure in the alumina tube.

### 3.2.3 High Temperature Furnace

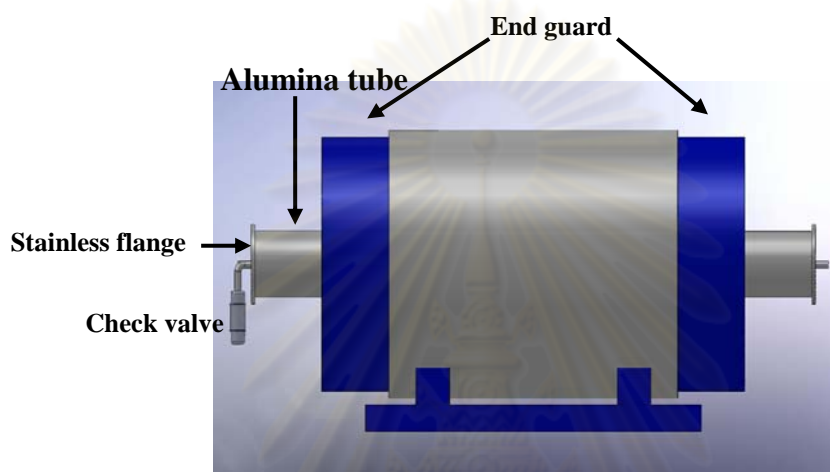


Figure 3.3: The high temperature furnace.

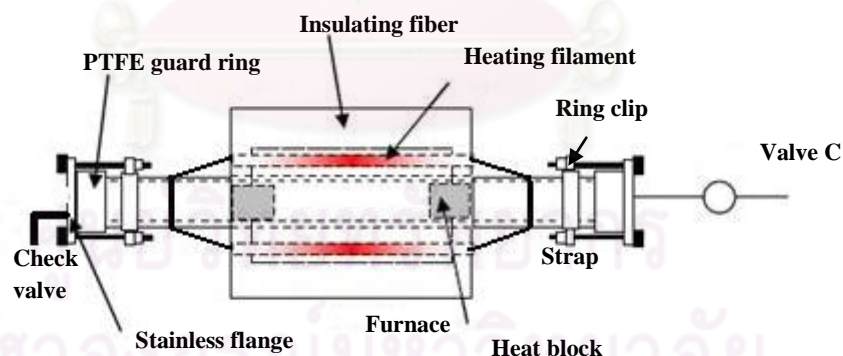


Figure 3.4: Schematic drawing of the furnace.

A “Lenton” tube furnace model LTF 16/50/180 is used. This model has a maximum operating temperature of 1600 °C and maximum continuously operating temperature of 1550 °C [44]. The furnace is set up and modified for a controlled-gas melting and annealing. The heating filaments are made from silicon carbide which are mounted parallel to the alumina tube.

High purity alumina tube (99.7%) with outer diameter of 60 mm and inner diameter of 50 mm is installed horizontally into the furnace bores. The tube end is approximately 20-25 cm away from the furnace bore and it is retained by straps with ring clips. Both ends of tube are protected by PTFE guard rings. “Viton” O-ring can endure heat more than 200 °C. O-rings are inserted between ring clips and alumina tube and they are inserted between the tube ends and PTFE guards. Heat blocks are placed in the tube for optimum temperature uniformity. Check valve is installed in the stainless flange to allow flow in one direction only; helping to protect alumina tube if over pressured. If the pressure in the alumina tube is slightly more than the atmospheric pressure, gas is released through the check value. Valve C is used to release gas from the tube.

### 3.2.4 Pump

“Busch” vacuum pump is used to evacuate the alumina tube to the absolute pressure of 150 mbar. The tube was purged with Ar gas. Pumping and purging are repeated alternatively 10 times before operating the furnace system. This would dilute the air in the tube by a factor of approximately  $0.15^{10}$  (less than 1 ppm).

### 3.2.5 Crucible

The cylinder alumina crucible with diameter of 29.3 mm and height of 30.2 mm is used in this work. We found that Fe-Si melt compound strongly stick to the crucible. So, inside the crucible was brushed by BN releasing agent to prevent the reaction between crucible and Fe-Si melt compound.



*Figure 3.5: Alumina crucible and cover coated with boron nitride releasing agent.*

### 3.3 The Procedures for Operating the High Temperature Furnace System

1. Open the stainless flange, insert the alumina crucible to the center of the furnace, insert the heat block, close the flange and close the valve C.
2. Set valve A to “OFF” and valve B to “4”. Pump the alumina tube until the pressure gauge is approximately constant (around -0.9 bar).
3. Set valve A to “2” and valve B to “OFF”. Flow Ar gas into the alumina tube until the pressure gauge read 0 bar.
4. Repeat step 2 and 3 for 10 times.
5. Set valve A to “1” and valve B to “3”. Flow Ar gas into the alumina tube until the flow meter reads 100 cc. /min.
6. Set program to operate the furnace system.

### 3.4 Sample Preparation

A mixture of Fe and Si powders with Fe/Si atomic ratio 1:2.0, 1:2.3 and 1:2.5 were mixed by mortar and pestle. The mixed powders were melted in an alumina crucible coated with boron nitride releasing agent. The crucible was put inside a tube furnace which has the argon gas flowing at the rate of 100 cc/min. The powder was heated up to 800 °C at the rate of 8 °C/min, and then to temperature  $T_m$  at the rate of 5 °C/min. The molten material was held for 1 h at this temperature. After cooling at the rate of 5 °C/min to 800 °C at the rate of 8 °C/min to room temperature as shown in Fig.3.6, samples were cut into slices with a thickness of approximately 1.7 mm and polished. Impurity on samples surface were removed by washing with alcohol and deionized water. Three types (FeSi<sub>2.0</sub>, FeSi<sub>2.3</sub>, FeSi<sub>2.5</sub>) of samples were *ex-situ* annealed at 820 °C or 950 °C for various time durations.

The bulk samples are mounted on a ceramic plate using a thermoset-cement and they are cut by diamond wheel saw as shown in Fig. 3.7. The samples are cut to slices with a thickness of 1.7 mm for XRD and SEM measurement and cut to a bar shape for Seebeck coefficient and resistivity measurement at high temperature. These figures will be shown in section 4.1. Cement on the sample is removed by isopropyl alcohol (IPA) and impurity on sample surface is removed by washing with alcohol and



deionized water. Samples are polished with sandpaper. The samples are dried by hot a plate at around 100-120 °C.

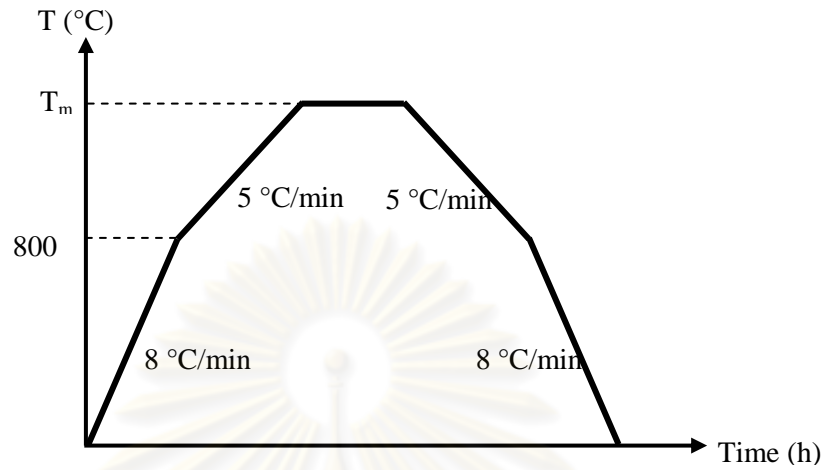


Figure 3.6: The temperature profile used to prepare the Fe and Si powder.

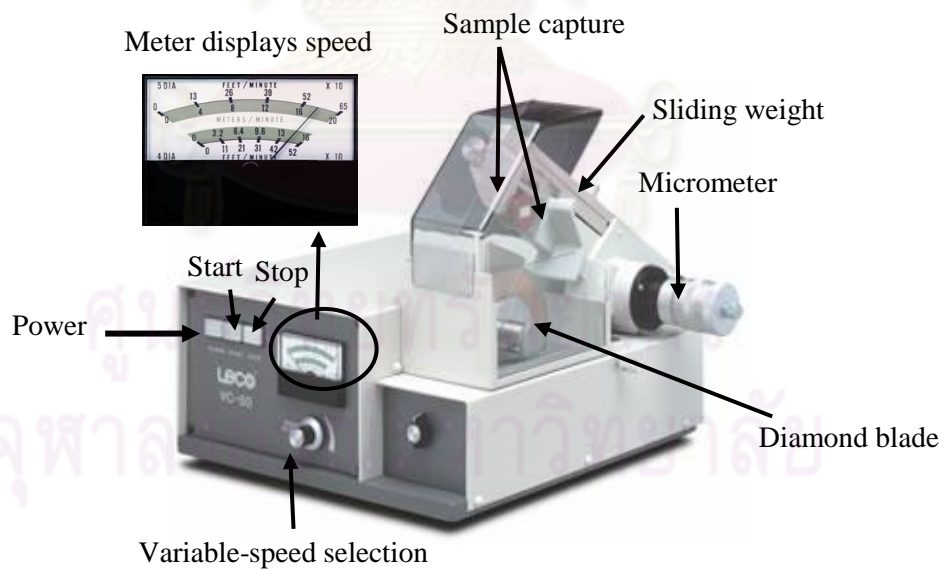


Figure 3.7: Precision diamond saw (LECO, VC-50) [45].

## 3.5 Characterization Technique

### 3.5.1 X-Ray Powder Diffraction (XRD)

X-ray powder diffraction (XRD) is a rapid analytical technique primarily used for phase identification of a crystalline material and can provide information on unit cell dimensions. If we consider a characteristic X-ray beam of wavelength  $\lambda$ , is incident on a pair of parallel planes, separated by an interplanar spacing  $d$ . The two parallel incident rays make an angle  $\theta$  with these planes. A reflected beam of maximum intensity will result if the waves are in phase. The ray from the second row of atoms travels a distance  $(AB + AC)$  greater than the ray from the top row. For this to produce a diffraction maximum the path difference must be an integer number of wavelengths. But  $AB$  and  $AC$  both equal  $d\sin\theta$ , we can express this relationship mathematically in Bragg's law

$$2d\sin\theta = n\lambda. \quad (3.1)$$

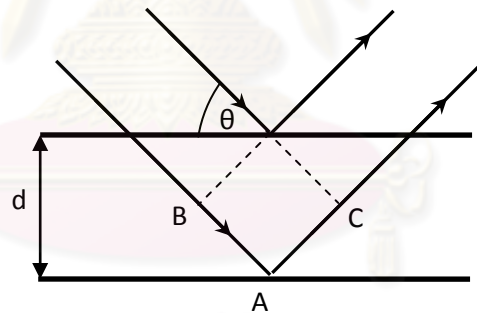


Figure 3.8: X-ray diffraction from atoms in a crystalline material.

The diffraction pattern includes information about peak position ( $2\theta$ ) and intensity ( $I$ ). The peak positions are indicative of crystal structure. The peak intensities reflect from each plane is directly dependent on the distribution of the electrons in the unit cell.

The relation for the relative intensity of pattern lines:

$$I \propto |F|^2 \left( \frac{1 + \cos^2 2\theta}{\sin^2 \theta \cos \theta} \right) \quad (3.2)$$

where  $I$  is relative integrated intensity (arbitrary unit),

$F$  is the structure factor and

$\theta$  is Bragg's angle.

The structure factor is sum of electron density at each point in the unit cell multiplied by complex number  $\exp[2\pi i(hx + ky + lz)]$ . That is

$$F_{hkl} = \int_{\text{cell}} \rho(xyz) \cdot \exp[2\pi i(hx + ky + lz)] dV. \quad (3.3)$$

A given set of planes with  $h, k, l$  cut the  $a$ -axis of the unit cell in  $h$  sections, the  $b$  axis in  $k$  sections and the  $c$  axis in  $l$  sections. For diffraction X-ray technique powder, incident beam of monochromatic X-ray interacts with a sample which is in the form of powder. These specimens must contain sufficient particles with the correct orientation to allow diffraction from all possible diffracting planes when rotated in the X-ray beam. In this work, the structural information can be investigated by using the Bruker AXS and  $2\theta$ -scan is from  $20^\circ$  to  $60^\circ$ ,  $0.02^\circ$  per step and scanning rate is  $2^\circ$  per minute. The XRD pattern is compared to Powder Diffraction File (PDF) of the International Centre for Diffraction Data. File No. 74-1285, No. 73-1843 for  $\beta$ -FeSi<sub>2</sub>, file No. 76-1748 for  $\epsilon$ -FeSi, file No. 41-1221 for  $\alpha$ -Fe<sub>2</sub>Si<sub>5</sub>, file No. 80-0018 for Si and file No.34-0529 for Fe.

### 3.5.2 Scanning Electron Microscope (SEM)

In scanning electron microscope, a solid sample is bombarded in vacuum by primary electron beam. Primary electron beam is produced from electron gun and it is focused by electromagnetic lens to a few nanometer in diameter. When an electron passes through an electromagnetic lens, it is subjected to two vector forces. A force parallel to the  $Z$  axis of the lens,  $F_Z$ , and a force parallel to the radius of the lens,  $F_R$ . These forces are responsible for two different actions on the electron, spiraling and focusing. The force  $F_Z$  causes electron to spiral through the lens. This spiraling causes the electron to experience  $F_R$  which causes the beam to be compressed toward the optical axis. The electromagnetic lens works by Lorentz force,  $\vec{F} = e(\vec{v}_\perp \times \vec{B})$ . The electrons spiral through the lens in a helical trajectory, the frequency of which is the electron cyclotron frequency,  $\omega$ :

$$\omega = \frac{eB}{m}. \quad (3.4)$$

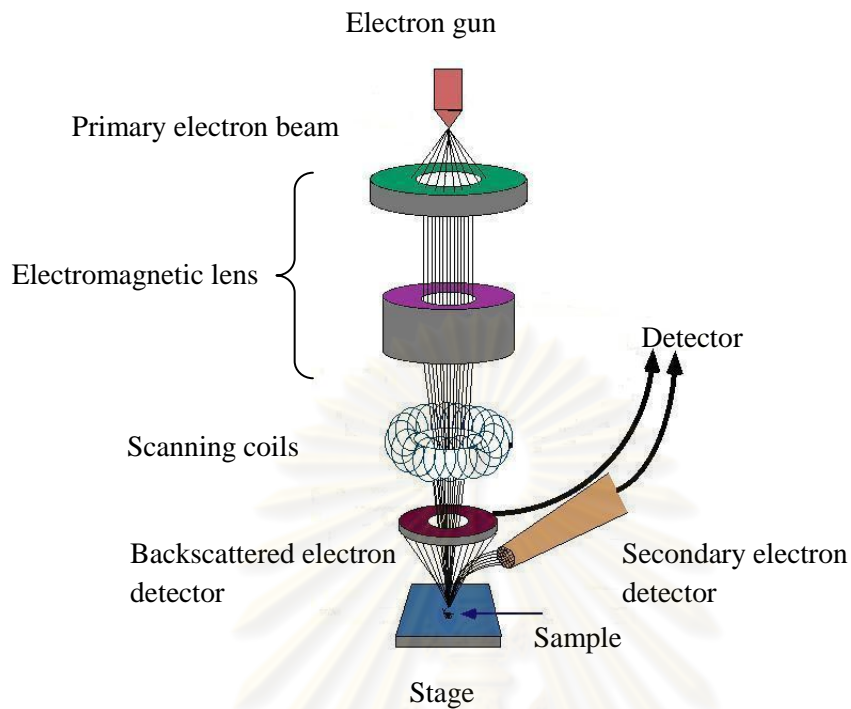


Figure 3.9: The scanning electron microscope components [46].

At the bottom end of the column, a set of scanning coils move the focus beam back and forth across the sample, row by row. When a primary electrons beam strikes a sample. A large number of signals are generated: backscattered electrons, secondary electrons, X-ray, Auger electrons. A detector counts these electrons and sends the signals to an amplifier. The final image is displayed on a screen. The interaction between primary electron and the sample may be elastic or inelastic depending on the deflection of the primary electron. At a large-angle deflection, elastic interaction is occurred. Inelastic interaction occurs at small-angle deflection.

The volume inside the sample when the interaction was occurred depends on the following factors:

- Atomic number of the material: higher atomic number materials absorb or stop more electrons, smaller interaction volume.
- Accelerating voltage: higher voltages, penetration lengths are long and cause a lager interaction volume.

- Angle of incidence for the electron beam: the greater the angle from the normal of the sample surface, the smaller the interaction volume.

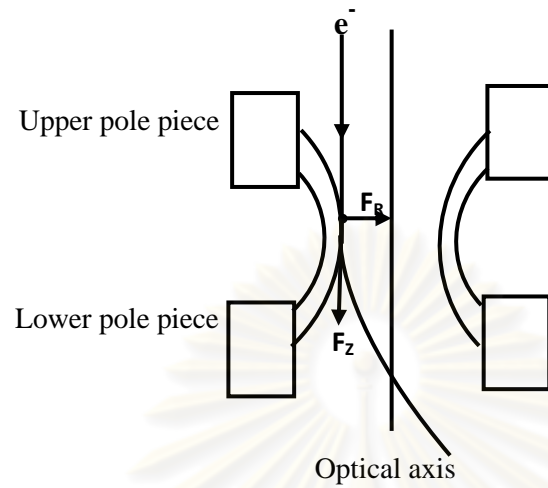


Figure 3.10: Cross sections of electron lens. The electron path through the lens is helical. Electron further from the optical axis undergoes greater deflection.

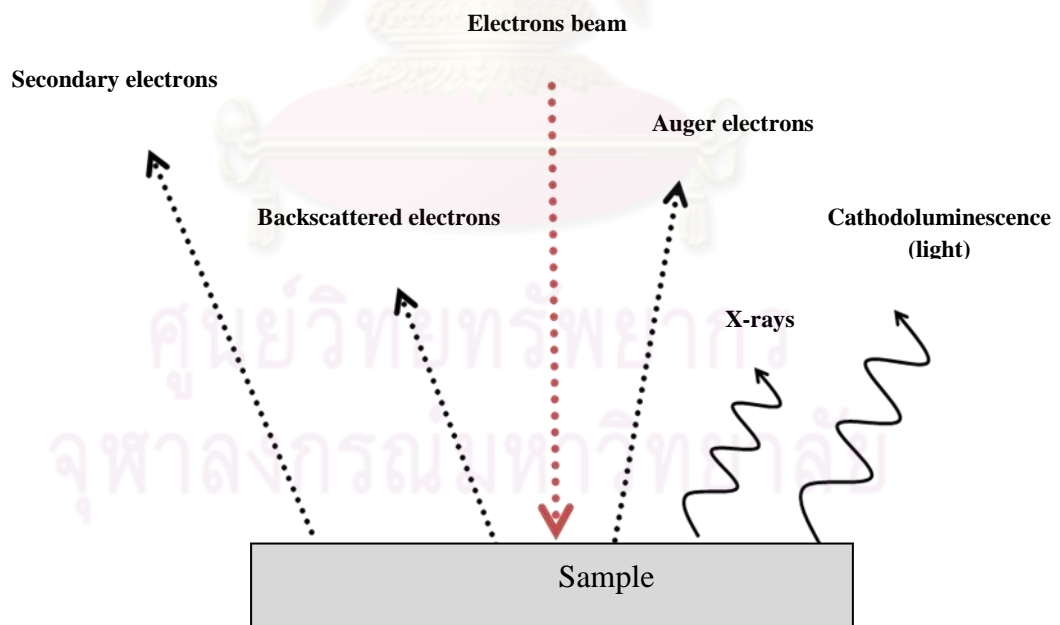


Figure 3.11: Photon and charge particle emission from electrons beam strikes a sample.

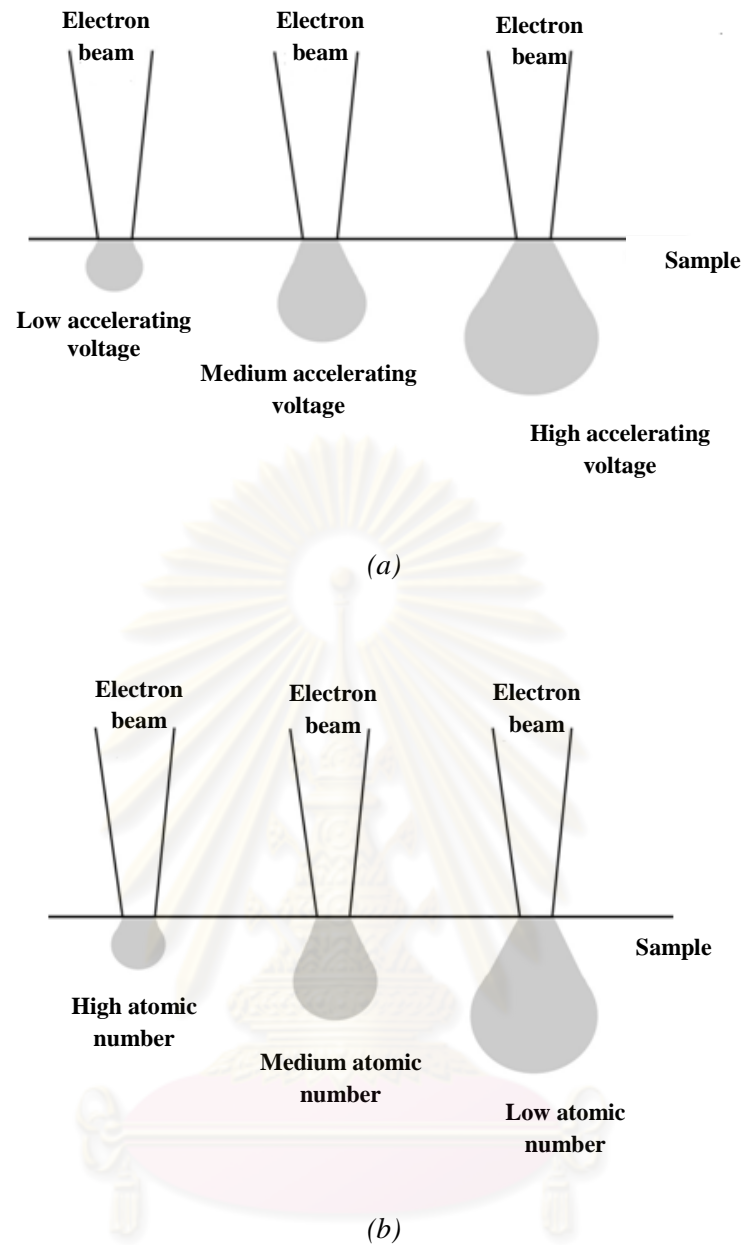


Figure 3.12: Schematics show the excitation volume: (a) vary accelerating voltage and (b) vary atomic number of the material.

Our discussion will focus upon backscattered electrons and secondary electrons.

### 3.5.2.1 Backscattered Electrons (BSE)

These electrons are the beam electrons that interact with the electric field of the nucleus of a sample atom, resulting in a change in the direction of beam electrons without a significant change in the energy of beam electrons, i.e. elastic collisions. This mode provides image contrast as a function of elemental composition, i.e., higher

atomic number material appears brighter than low atomic number material because as the atom nucleus increases, the number of BSEs increases. Thus, BSEs can be used to get an image that has different elements present in the sample. To create an SEM image, the emitted electrons are detected for each position in the scanned area by an electron detector. The intensity of the electron signal is displayed as brightness on a cathode ray tube (CRT). The CRT display represents the morphology of the sample surface area. Magnification of the CRT image is the ratio of the image display size to the sample area scanned by electron beam. In this work, we use the BSE image to identify the  $\alpha$ -,  $\epsilon$ -, or  $\beta$ - phase of the sample.

### 3.5.2.2 Secondary Electrons (SE)

Secondary electrons are electrons that have been ejected from the electron shell when beam of electrons interact with the electric field, produce from electron in sample atom. The result is a transfer of energy to the sample atom and expulsion of electron from that atom as a SEs. If the vacancy due to the creation of a SEs is filled from a higher level orbital, characteristic X-Ray of that energy transition is produced. In the spectrum range of 0-20 keV, all elements from boron to uranium are detected.

In this work, X-ray spectroscopy that is known as Energy Dispersive X-ray Spectroscopy, EDS is used to determine the chemical composition of the sample by detecting characteristic X-ray. The weight or atomic percent of the sample can be calculated from the area under the peaks.

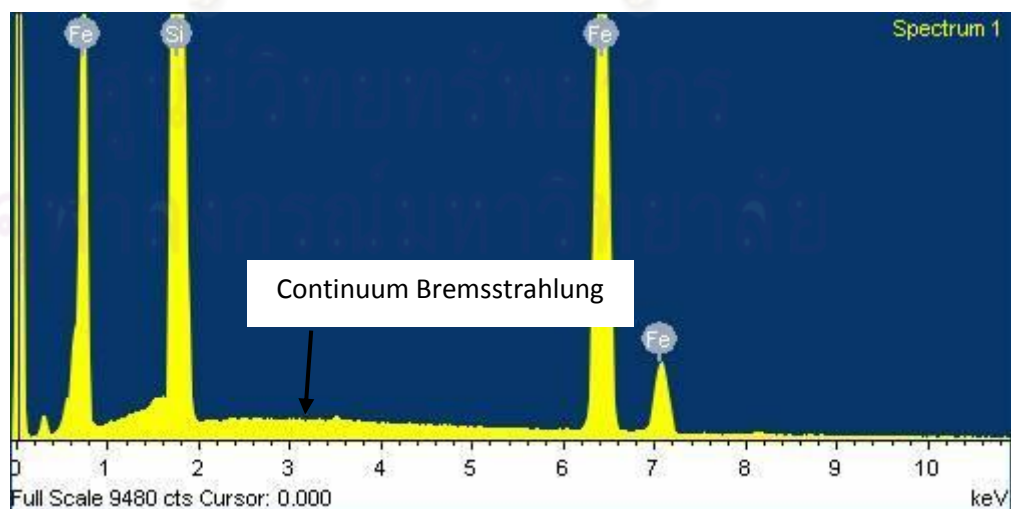


Figure 3.13: An example of EDS spectrum of Fe-Si compound.

We employed the scanning electron microscope, Phillips XL30CP. Because the SEM works with electrons, the samples must be electrically conductive to prevent charge accumulation on the sample surface. Carbon tape is used for this propose.

### 3.5.3 Thermal Analysis

Thermal analysis is the analysis of a change in a property of a sample when temperature changes. There are many methods in thermal analysis. Of these techniques for detecting properties, the five shown below are commonly used techniques representative of thermal analysis.

*Table 3.1: Thermal Analysis Categories.*

Name	Measurement Object	Unit
Differential Thermal Analysis (DTA)	Temperature difference	°C/μV
Differential Scanning Calorimetry (DSC)	Thermal Flow difference	W
Thermogravimetry (TG)	Mass change	mg
Themomechanical Analysis (TMA)	Length	mm
Dynamic Thermomechanical Measurements (DMA)	Electricity	Pa

Differential thermal analysis, DTA, is the simplest and most widely used thermal analysis technique to identify the reaction temperature. The temperature difference ( $\Delta T$ ) between the sample and inert reference material is recorded under identical conditions

$$\Delta T = T_s - T_r \quad (3.5)$$

where  $T_s$  is the sample temperature and  $T_r$  is the reference temperature. DTA system consists of two identical sample holders containing small amount sample and inert reference material respectively. Both sample holders are heated by single heater and they are connected to the thermocouples measuring temperature,  $T_s$  and  $T_r$ . Thermocouples are connected to a voltmeter which reports the temperature difference as  $\mu V$ -signal. As furnace temperature is increased and no reaction occurs in the sample,  $\Delta T$  will be roughly constant or change slowly. If the transformation of the sample has occurred,  $\Delta T$  will increase or decrease rapidly because the input heat will



raise the temperature of reference while the sample phase transition involves a latent heat.

The reference material should have the following characteristics:

- (i) It should undergo no thermal events over the operating temperature rang.
- (ii) It should not react with the sample holder or thermocouple.
- (iii) Both the thermal conductivity and the heat capacity of the reference should be similar to those of the sample.

Alumina,  $\text{Al}_2\text{O}_3$ , and carborundum,  $\text{SiC}$ , have been extensively used as reference material.

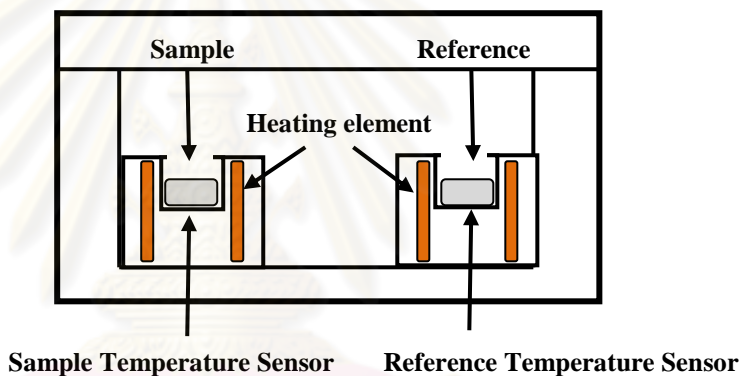


*Figure 3.14: DTA system.*

DTA curve is a plot between furnace temperature on the x-axis and the temperature difference on the y-axis. It provides data on phase transformations that occur on the sample. Empty run is performed prior to the measurement to provide a base-line, which will be subtracted from the measured data.

$\Delta T$  is negative for the endothermic reaction and positive for the exothermic reaction. In this work, DTA is used to identify the  $\beta$ -phase formation, such as peritectoid and eutectoid reaction. The machine in use is Netzsch STA model 449C Jupiter.

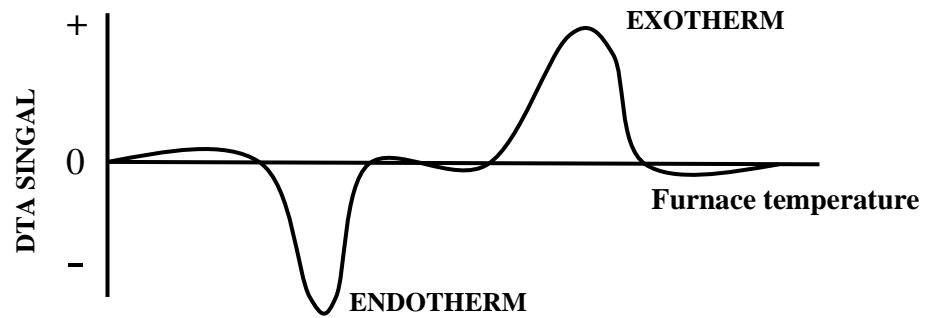


Figure 3.15: DTA curve show endothermic and exothermic peak.

### 3.5.4 Seebeck Coefficient and Electrical Resistivity Measuring System

#### 3.5.4.1 Hot-Probe Seebeck Coefficient Measurement

The Seebeck coefficient at room temperature is measured by a hot-probe technique. A schematic diagram of an apparatus is shown in Fig.3.16. The hot probe is made from Cu rod where its tip is heated by enamel-coated Cu coil connected to a DC power supply. A hot probe tip is positioned on to the top surface of the sample. The thermocouple (type K) is attached to the probe to measure the probe-tip temperature ( $T_H$ ). The bottom of the sample is in contact with a large Cu block which acts as a heat sink. Another thermocouple (type K) is also attached to this block for the measurement of base temperature ( $T_C$ ). Additional Cu wires are attached to the tip and the Cu block in order to measure the developed voltage. In this experiment,  $T_C$  of Cu block does not change because of its large mass and small heating power at the tip. The probe tip heats the sample in the vicinity of the tip leading to a temperature gradient. The measurement is done over the temperature range of 26-40 °C. The potential different,  $\Delta V$ ,  $T_H$  and  $T_C$  can be read sequentially by Keithley™ digital millimeter model 2700 equipped with a scanner card model 7100. The convention for our system is that if the sign of  $\Delta V$  is minus, the major carriers will be electrons. On the other hand, if the sign of  $\Delta V$  is positive, the major carries will be holes. Because  $T_C$  is practically constant for our system, the Seebeck coefficient is usually determined from the slope of  $\Delta V$  versus  $T_H$ .

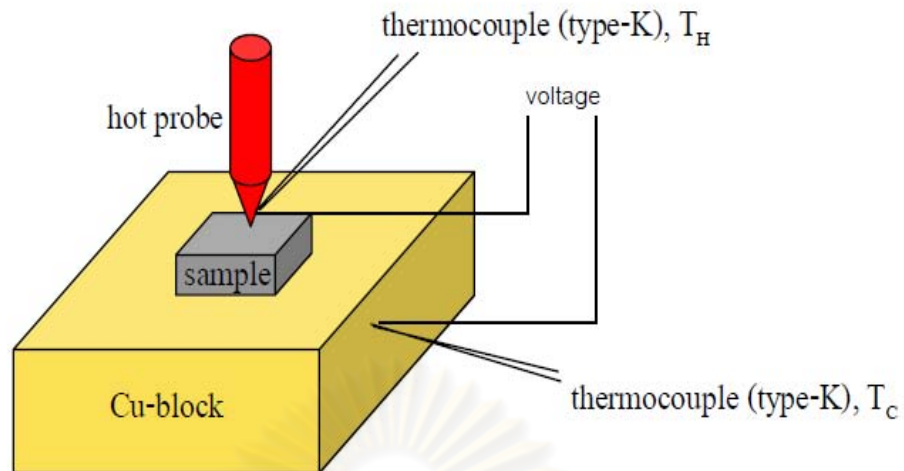


Figure 3.16: Schematic of Seebeck measurement setup.

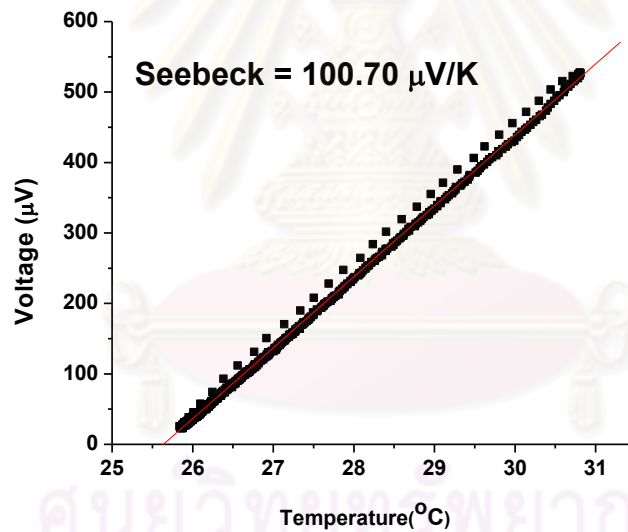


Figure 3.17: The voltage-  $T_H$  plot and the slope is Seebeck coefficient.

### 3.5.4.2 Seebeck Coefficient and Electrical Resistivity at High Temperature

The DC four-terminal method is used to measure the electric resistance by applying a constant current ( $I$ ) between both ends of the sample and measuring the change in voltage  $\Delta V$  between one wires at each of the two thermocouple pair as shown in Fig. 3.18. The Seebeck coefficient is measured by a static DC method based on the slope of a voltage versus temperature-difference curve. The diagram is shown in Fig. 3.19.

The commercial equipment (ZEM-3, Ulvac, Inc.) is used to measure the electric resistivity and Seebeck coefficient on the same bar-type sample with a dimension 2 mm by 4 mm in cross section and 15-17 mm in length. This equipment is set up at Thailand Institute of Scientific and Technological Research. Before starting the measurement, a V-I plot made to check whether the sample is properly contacted with the detecting probes. All measurements can be controlled by computer and raw data are automatically saved. The error of the Seebeck coefficient and electrical resistivity measurements were estimated to be less than  $\pm 5\%$  [47].

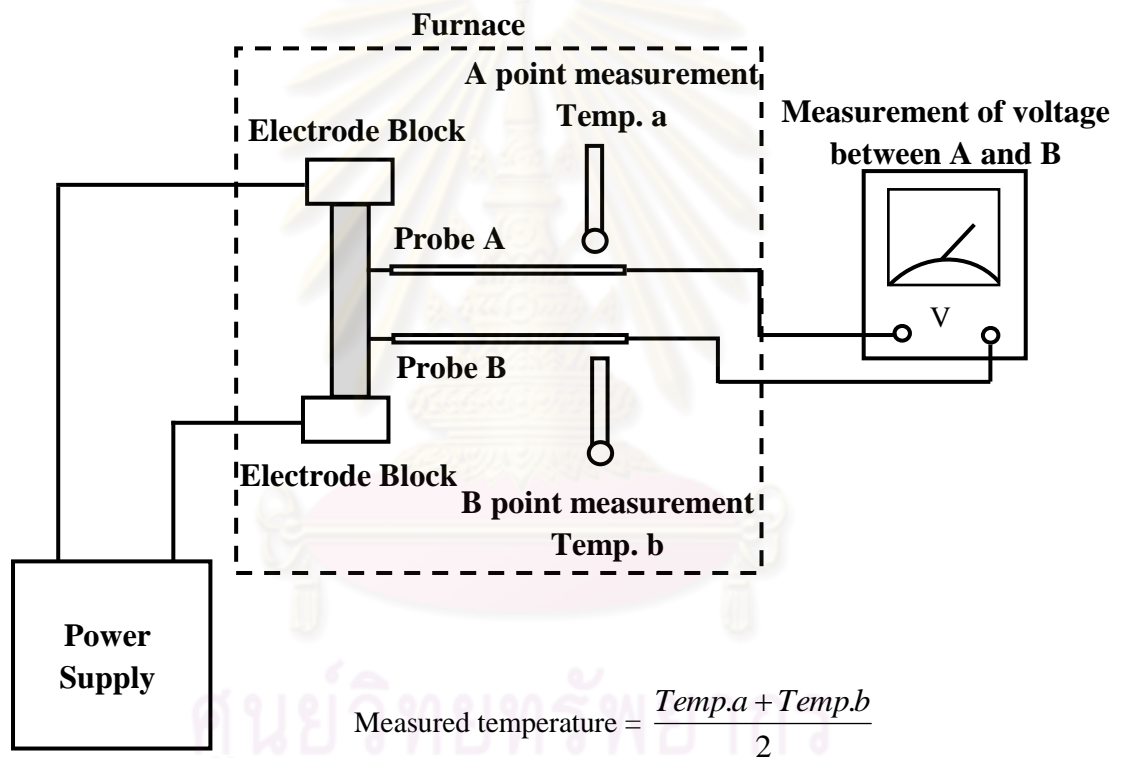


Figure 3.18: Diagram of high temperature electrical resistivity measurement.

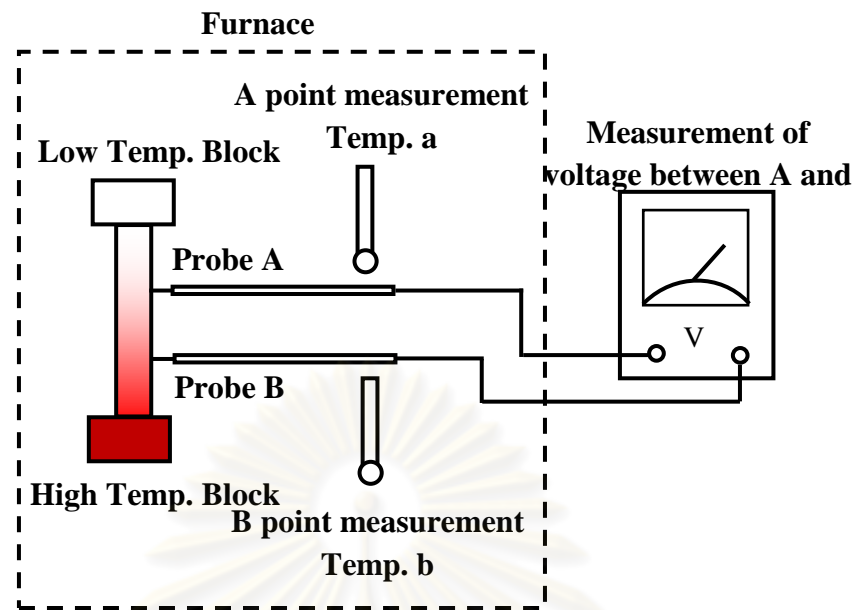


Figure 3.19: Diagram of high temperature Seebeck coefficient measurement.



Figure 3.20: The commercial equipment (ZEM-3, Ulvac, Inc.) is used to measure the electric resistance and Seebeck coefficient from room temperature to 700 °C. [48]

### 3.5.5 Measurement of Thermal Properties

Thermal conductivity ( $K$ ) measurements at steady-state condition are difficult and time consuming. The fundamental quantity that enters into heat transfer situation at steady state is the thermal diffusivity ( $\lambda$ ). The diffusivity is a measure of how quickly a body can change its temperature. It increases with the ability of a body to conduct heat. This is converted to the steady-state thermal conductivity through the equation

$$K = \lambda \rho C_p \quad (3.11)$$

where  $\rho$  is density and  $C_p$  is specific heat.

Consider the one dimension of heat equation:

$$\frac{dT(x,t)}{dt} = c^2 \frac{d^2T(x,t)}{dx^2} \quad (3.12)$$

note  $c^2 = \lambda$  is referred to as the thermal diffusivity.

The solution of heat equation can be solved by separation of variable method:

$$T(x,t) = \frac{1}{L} \int_0^L T(x,0) dx + \frac{2}{L} \sum_{n=1}^{\infty} \exp\left(-\frac{n\pi^2 \lambda t^2}{L^2}\right) \times \cos \frac{n\pi x}{L} \int_0^L T(x,0) \cos \frac{n\pi x}{L} dx. \quad (3.13)$$

The measurement of the thermal diffusivity of a material is usually carried out by rapid heating ( $\leq 1$  msec) one side of a sample and measuring the temperature rise curve on the opposite side. The time that it takes for the heat to travel through the sample and cause the temperature to rise on the rear face calculates the through-plane thermal conductivity if the specific heat density is known.

Before the flash, the temperature of the sample and surroundings is at some uniform temperature. Assuming that  $t = 0$ , the heat quantity,  $Q$ , given by an instantaneous pulse heat source is absorbed in an area of small depth  $h$ , on the surface of the sample and the heat flux lines are parallel and directed through the sample; there is no heat flow in the plane of the sample. Temperature distribution is given by

$$0 < x \leq h ; \quad T(x,0) = \frac{Q}{\rho Ch}$$

$$h < x \leq L ; \quad T(x,0) = 0.$$

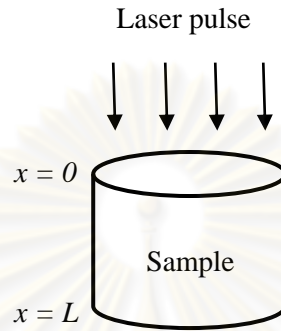


Figure 3.21: Principles of flash method.

From equation (2.15), the temperature distribution after time  $t$ :

$$T(x,t) = \frac{Q}{\rho CL} \left[ 1 + 2 \sum_{n=1}^{\infty} \cos\left(\frac{n\pi x}{L}\right) \frac{\sin(n\pi h/L)}{n\pi h/L} \times \exp\left(-\frac{n^2 \pi^2 \lambda t}{L^2}\right) \right]. \quad (3.14)$$

If  $h$  is very small,  $\sin\left(\frac{n\pi h}{L}\right) \approx \frac{n\pi h}{L}$ . Temperature distribution at  $x=L$ :

$$T(L,t) = \frac{Q}{\rho CL} \left[ 1 + 2 \sum_{n=1}^{\infty} (-1)^n \times \exp\left(-\frac{n^2 \pi^2 \lambda t}{L^2}\right) \right]. \quad (3.15)$$

From equation (3.15), the maximum temperature at  $x=L$ :

$$T_M = \frac{Q}{\rho CL}. \quad (3.16)$$

Here, assuming that

$$\Gamma(L,t) = \frac{T(L,t)}{T_M} \quad (3.17)$$

$$\eta = \frac{\pi^2 \lambda t}{L^2} . \quad (3.18)$$

So

$$\Gamma(L,t) = 1 + 2 \sum_{n=1}^{\infty} (-1)^n \exp(-n^2 \eta) . \quad (3.19)$$

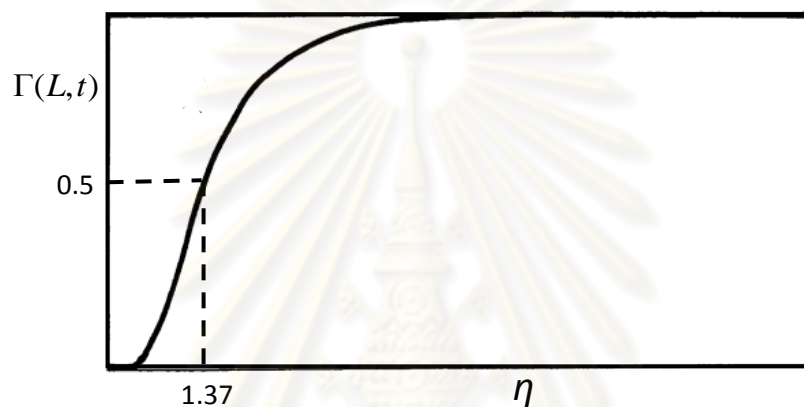


Figure 3.22: Relationship between  $\Gamma(L,t)$  and  $\eta$ .

The relation between  $\Gamma(L,t)$  and  $\eta$  is shown in figure 3.22. This curve represents the temperature change on the back side of sample. Since  $\eta$  is equal to 1.37 when  $\Gamma(L,t) = 0.5$ . Thermal diffusivity is given as following equation (3.18).

$$\lambda = 1.37 \frac{L^2}{\pi^2 t_{1/2}} \quad (3.20)$$

where  $t_{1/2}$  is the time required for temperature on the back side of the sample to reach  $1/2$  of the maximum value after the sample surface is irradiated with instantaneous heat source.

In this work, the thermal diffusivity is measured by a laser-flash method using a commercial ULVAC machine TC-7000H. The error of the thermal diffusivity measurements was about 10% [47]. The system is horizontal arrangement and it consists of a Rb laser, a vacuum chamber, a computer and an infrared radiation thermometer equipped with an InSb as shown in Fig.3.23.



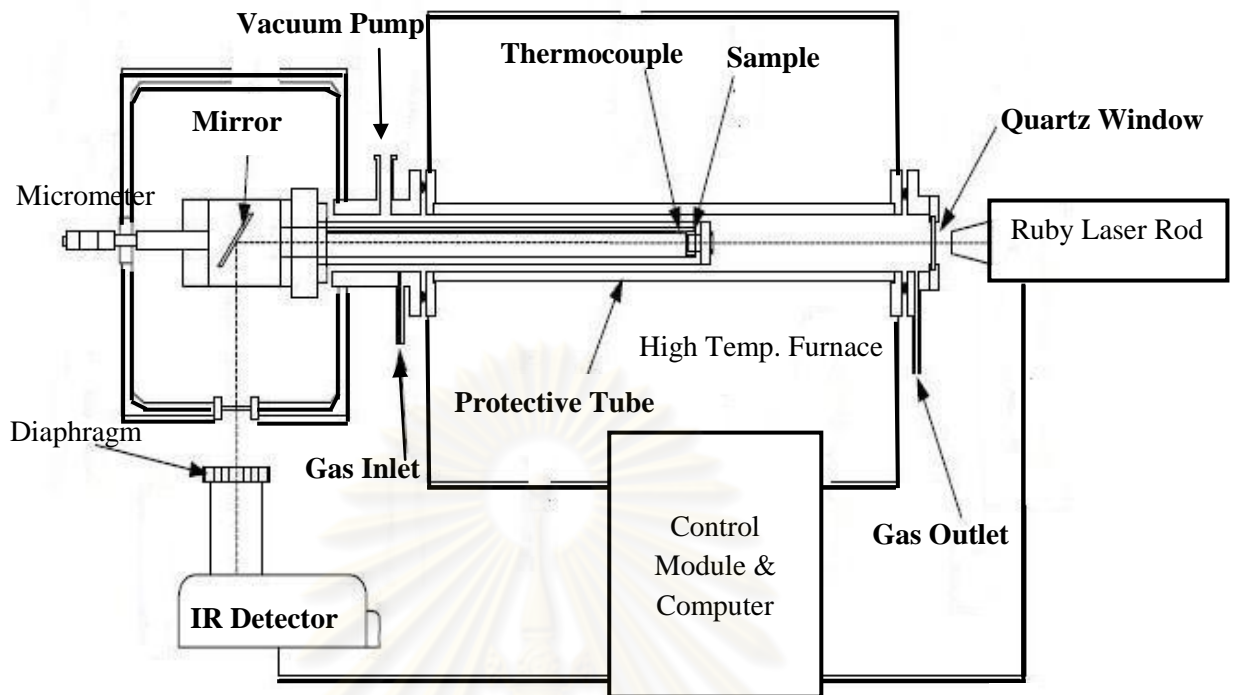


Figure 3.23: A schematic diagram of the laser flash unit.

The laser is generated from high speed Xenon discharge pulse source, generated a maximum 2-9.5 J/pulse. The sample requires a disk shape with diameter 10 mm and thickness 1-3 mm. The two surfaces are parallel and flat. The sample is coated with graphite to avoid a high laser reflection. In the process of measuring, the front surface of the sample is irradiated with laser beam. The laser energy is absorbed on the front surface of the sample and gets converted into the heat energy. The heat energy travels through the sample. Immediately after the laser pulse, the rear surface is monitored by using InSb infrared detector. The computer uses the rear surface temperature versus time trace to obtain a value of half rise time,  $t_{1/2}$ . The magnitude of the temperature rise and the amount of laser energy are not required for thermal diffusivity determination, but only the shape of curve, which is used in the analysis.

The flash method for measuring thermal diffusivity was also used to measure the specific heat,  $C_p$

$$C_p = \frac{Q}{\rho L \Delta T} \quad (3.21)$$

where  $\Delta T$  is temperature rise.

The laser energy,  $Q$ , is the quantity of heat absorbed by the sample and it depends on emissivity,  $\varepsilon$ . The proposed route is to measure the temperature rise of a reference sample of known specific heat, in order to determine the energy input. However, it is necessary to coat both sample and reference with a coating usually graphite to ensure the same energy absorption. For reference, the relationship between temperature rise and laser energy is

$$Q\varepsilon' = \rho' L' C'_p \Delta T' \quad (3.22)$$

where the prime refer to the reference sample. For the unknown sample using the same energy input and coating

$$Q\varepsilon = \rho L C_p \Delta T. \quad (3.23)$$

If  $\varepsilon = \varepsilon'$ , the Eqs. (3.22) equal to (3.23) and then

$$\rho' L' C'_p \Delta T' = \rho L C_p \Delta T \quad (3.24)$$

$$C_p = \frac{\rho' L' C'_p \Delta T'}{\rho L \Delta T}. \quad (3.25)$$

The thermal conductivity is calculated using the equation (3.11).

ศูนย์วิจัยและพัฒนา  
จุฬาลงกรณ์มหาวิทยาลัย

# CHAPTER IV

## RESULT AND DISCUSSION

### 4.1 As-Grown Sample

Figure 4.1 shows a bulk of the as-grown Fe-Si compound for  $\text{FeSi}_x$  sample. The shape of sample is semispherical-like, a drop of liquid metal. Most of the surface look shiny but a dull thin layer cover a bottom of it. Kloc *et al.* [49] synthesised Fe – Si compound by Czochralski technique, a method of producing large single crystals by inserting a small seed crystal of germanium, silicon, or other semiconductor material into a crucible filled with similar molten material, then slowly pulling the seed up from the melt while rotating it. During melting of Fe and Si in Ar atmosphere, a dull thin layer of oxide covered the surface. After heating in vacuum, the dull layer slowly disappeared and the surface of the melt became shiny. From these results, it may be imply that the dull thin layer on the as-grown sample is oxide layer. However, the accurarte result will be confirmed by EDS measurement and it is presented in section 4.3.

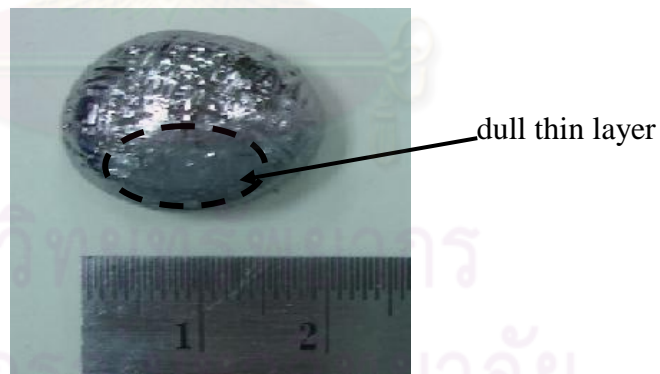
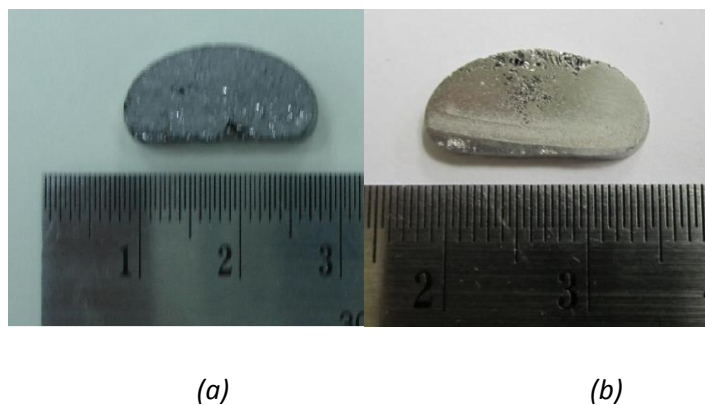
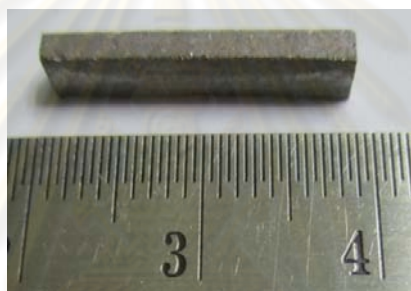


Figure 4.1: As-grown  $\text{FeSi}_x$  sample.

The samples are cut into slices with a thickness of 1.7 mm for XRD and SEM measurements, bar with a rectangular shape 15- 20 mm in length, 2 mm in width and 4 mm in thickness for Seebeck coefficient and resistivity measurement at high temperature and disk shape, 10-15 mm in diameter, 2-4 mm in thickness for thermal diffusivity measurement as shown in Fig.4.2, Fig 4.3 and Fig.4.4, respectively.



*Figure 4.2: Cross section of  $FeSi_x$  after cutting by precision diamond saw, (a) before polishing and (b) after polishing by sandpaper. They were prepared for XRD and SEM measurement.*

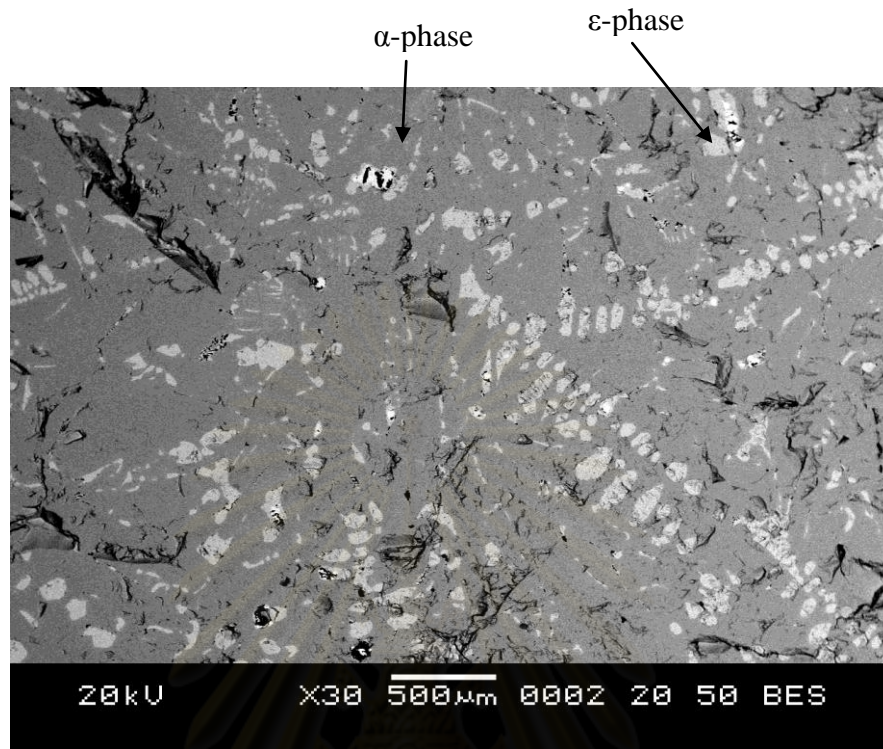


*Figure 4.3: Bar shape of  $FeSi_x$  after cutting by precision diamond saw prepared for electrical resistivity and Seebeck coefficient measurement.*

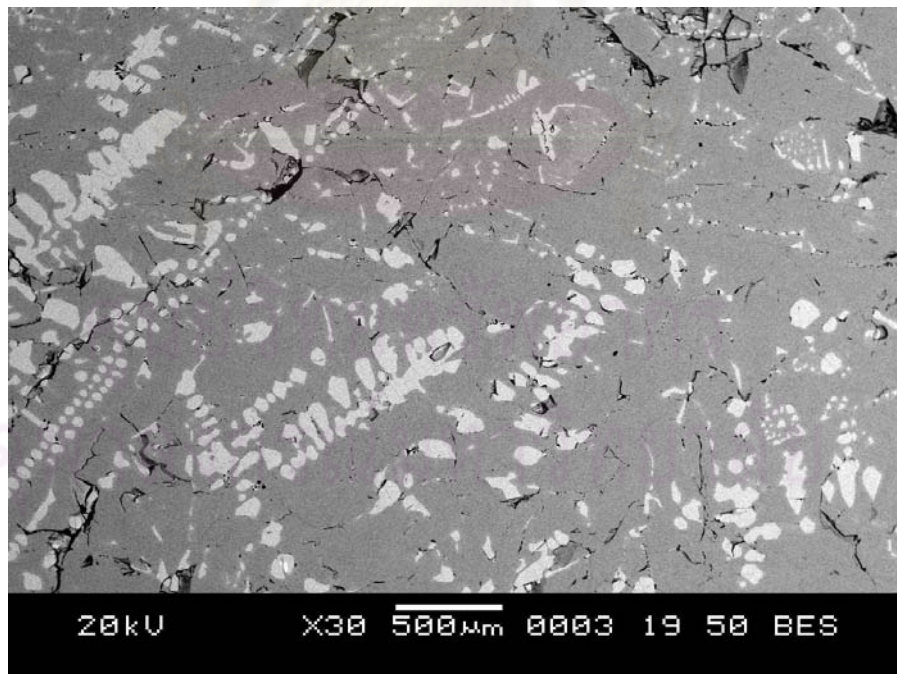


*Figure 4.4: Disk shape of  $FeSi_x$  after cutting by precision diamond saw prepared for thermal diffusivity measurement.*

## 4. 2 Effect of Melting Temperature and Melting Time on the Grain Size of $\epsilon$ -phase and Seebeck Coefficient



(a)



(b)

Figure 4.5: 30x SEM micrograph of  $\text{FeSi}_{2.3}$  melted at (a) 1450 °C and (b) 1550 °C for 1 h.  $\alpha$ -phase surrounding the  $\epsilon$ -phase is lighter color than that of  $\alpha$ -phase matrix.

Kakemoto *et al.* [29] reported that the structural of Fe and Si with atomic ratio Fe/Si = 1/2, 2/5 and 1/3 was homogenous when it was melted at 1450 °C for 1 h. In this work, we found that the samples were brittle when they were melted at 1450 °C for 1 h or 2 h, especially in FeSi<sub>2.5</sub> sample which has the highest Si content. The highest operating temperature of furnace is 1600 °C and melting point of Fe and Si are 1538 °C and 1414 °C respectively. So, the samples are melted at 1550 °C for 1 h and 2 h. We expect that the grain size of  $\epsilon$ -phase is increased with temperature. In order to investigate the effect of melting temperature on the grain size of  $\epsilon$ -phase, two samples were prepared with melting temperatures at 1450 °C and 1550 °C for 1 h. SEM micrographs of these samples are shown in Fig. 4.5. Both have  $\epsilon$ -phase inclusions in the matrix of  $\alpha$ -phase. No difference in grain size of  $\epsilon$ -phase can be observed. The surface of the sample melted at 1550 °C is smoother than that melted at 1450 °C. This result indicates that the grain size of  $\epsilon$ -phase is independent on the selecting temperatures, 1450 °C and 1550 °C. However, the effects of another melting temperature on the grain size of  $\epsilon$ -phase are required before this can be concluded.

The effects of melting time and melting temperature on the Seebeck coefficient are shown in Fig. 4.6 and Fig. 4.7, respectively. The Seebeck coefficient does not significantly change with the melting time or melting temperature range measured here but it depends on only Si content in the starting sample. The Seebeck coefficient of Si that is used in this work is around 140  $\mu\text{V/K}$ . The Seebeck coefficient is highest value in the as-grown FeSi<sub>2.5</sub> sample because it has higher Si content than FeSi<sub>2.0</sub> and FeSi<sub>2.3</sub> samples. These results imply that the amount of  $\epsilon$ -phase does not increase when increasing of melting time and melting temperature. Therefore, next experiment will use melting temperature at 1550 °C for 1 h.

### 4.3 XRD and SEM Image of As-Grown Sample

Figure 4.8 shows the XRD pattern of as-grown samples. Symbols represent peak positions and relative intensity for each phase of silicon-iron compounds or element using database of a computer program PCPDFWIN version 2.01. The elemental Si ( $2\theta \approx 28.4^\circ$ ) and Fe ( $2\theta \approx 44.8^\circ$ ) peaks are unseen. FeSi<sub>2.0</sub> and FeSi<sub>2.3</sub> samples compose mainly of  $\alpha$ - and  $\epsilon$ - phases. The  $\beta$ - phase was not found in all as-grown

samples. For  $\text{FeSi}_{2.3}$  sample, the relative XRD intensity of  $\epsilon$  to  $\alpha$ -phase decreased and  $\text{FeSi}_{2.5}$  sample has only  $\alpha$ -phase.

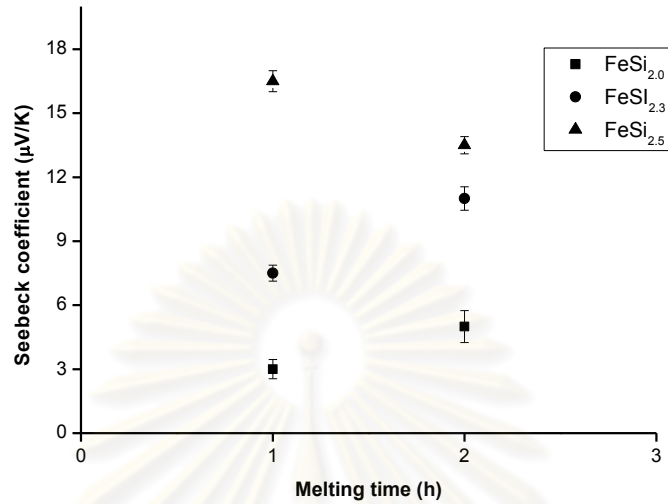


Figure 4.6: The Seebeck coefficient of the as-grown samples melted at  $1550\text{ }^\circ\text{C}$  for 1 and 2 h.

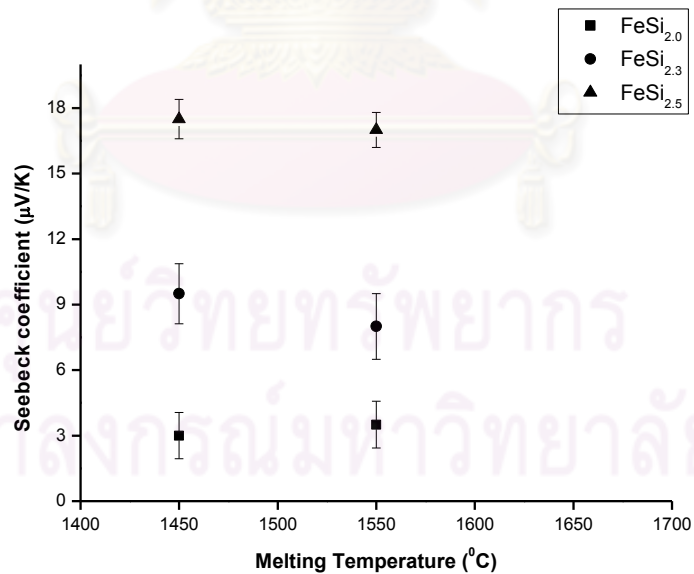


Figure 4.7: Seebeck coefficient of the as-grown samples melted for 1 h at  $1450\text{ }^\circ\text{C}$  and  $1550\text{ }^\circ\text{C}$ .

SEM micrographs of as-grown samples after polishing are shown in Fig.4.9. EDS analysis of all samples over a square-millimeter area confirms that the Si/Fe ratio is as same as that of the prepared mixture before melting. Some cracks are observed which occur during cutting and polishing. The Fe/Si ratios obtained from EDS spectrum confirm that the white dot in Fig. 4.8(A) is  $\epsilon$ -FeSi. The Fe:Si atomic ratio of these white dots as shown in Table 4.1 is in the range of 1: (1.07-1.13) . The background (dark area) of all pictures in Fig. 4.8 has the Fe:Si ratio in the range of 1: (2.46 - 1.51) which is equivalent to  $\alpha$ -Fe<sub>2</sub>Si<sub>5</sub>. In FeSi<sub>2.0</sub> sample, the shape of  $\epsilon$ -phase is mostly round with the diameter of approximately 10  $\mu$ m. In FeSi<sub>2.3</sub> sample, the amount and size of  $\epsilon$ -phase decrease. The  $\epsilon$ -phase with a size from 3 $\mu$ m to 10  $\mu$ m is distributed within the  $\alpha$ -matrix. The boundaries between the two phases are irregular in shape. In FeSi<sub>2.5</sub> sample, the structures consist of only  $\alpha$ -phase and this sample is very brittle. These results are inconsistent with the XRD pattern. Oxygen content was not detected by EDS.

In summary,  $\beta$ -phase does not form in as-grown samples. Theoretically, super-cooling by more than 230 °C per minute is necessary to form  $\beta$ -FeSi<sub>2</sub> directly from melt [17]. The amount and size of  $\epsilon$ -phase decrease and the brittleness increases which increasing Si/Fe ratio.

*Table 4.1: EDS measurement for the as-grown samples.*

Sample	$\epsilon$ phase (Fe:Si = 1:1)	$\beta$ phase (Fe:Si = 1: 2)	$\alpha$ phase (Fe:Si = 1: 2.5)
FeSi <sub>2.0</sub>	Fe:Si = 1 : 1.13	Not detectable	Fe:Si = 1 : 2.47
FeSi <sub>2.3</sub>	Fe:Si = 1 : 1.07	Not detectable	Fe:Si = 1 : 2.46
FeSi <sub>2.5</sub>	Not detectable	Not detectable	Fe:Si = 1 : 2.51



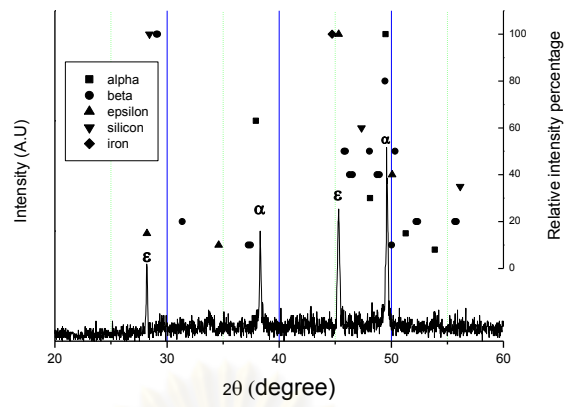
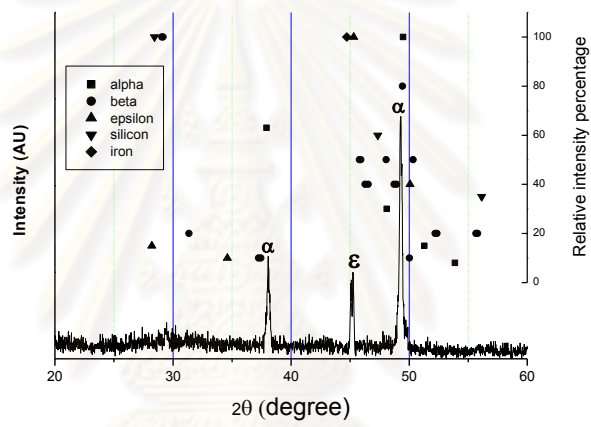
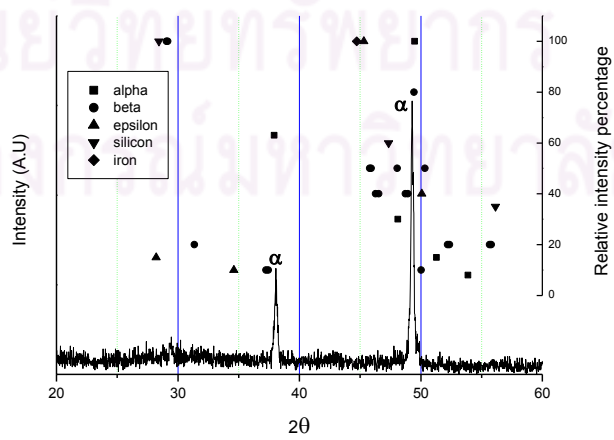
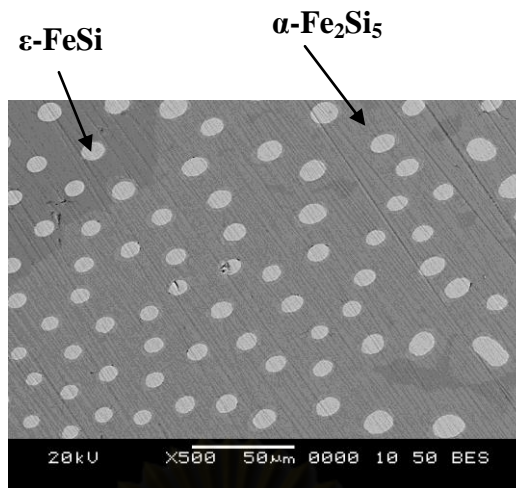
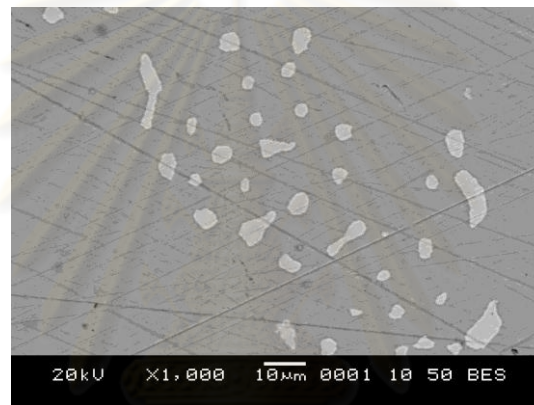
(a) *As-grown FeSi<sub>2.0</sub>*(b) *As-grown FeSi<sub>2.3</sub>*(c) *As-grown FeSi<sub>2.5</sub>*

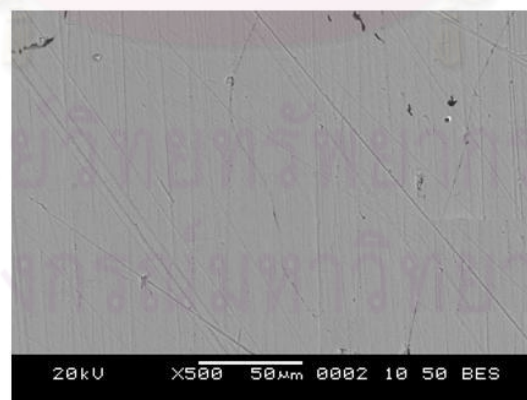
Figure 4.8: XRD patterns of as-grown  $FeSi_{2.0}$ ,  $FeSi_{2.3}$  and  $FeSi_{2.5}$  samples.



(a) As-grown  $FeSi_{2.0}$



(b) As-grown  $FeSi_{2.3}$



(c) As-grown  $FeSi_{2.5}$

Figure 4.9: Surface morphology of  $FeSi_{2.0}$ ,  $FeSi_{2.3}$  and  $FeSi_{2.5}$  samples observed by SEM.

## 4.4 DTA Measurement

According to the phase transformation reaction, other phases of as-grown sample can be changed to  $\beta$ -phase by thermal treatment. DTA was carried out to obtain qualitative information of  $\beta$ -phase formation. In Table 4.2, we summarize annealing temperature for all reactions reported in several publications.

From Fig. 4.10, for  $\text{FeSi}_{2.0}$ ,  $\text{FeSi}_{2.3}$  samples, there are two endothermic peaks in the temperature range 960-1010 °C for all heating stages and one broad exothermic peak around 830 °C for all cooling stages. For  $\text{FeSi}_{2.5}$  sample, there is only one sharp endothermic peak at 960 °C during heating stage. Further heating stage produces a smaller 960 °C endothermic peak because less  $\alpha$ -phase existed.

Isothermal annealing at 830 °C led to the semiconducting  $\beta$ -phase transformation by peritectoid reaction, ( $\epsilon + \alpha \rightarrow \beta$ ), or subsequence reaction, ( $\epsilon + \text{Si} \rightarrow \beta$ ) [26, 28, 50, 52]. However, degree of peritectoid reaction of our sample is small and the exothermic peak during cooling stage of  $\text{FeSi}_{2.0}$ ,  $\text{FeSi}_{2.3}$  samples becomes broad. There is no  $\epsilon$ -phase presented in the as-grown  $\text{FeSi}_{2.5}$  sample and therefore the peritectoid reaction or subsequence reaction could not occur. The exothermic peak around 830 °C could not be observed.

Table 4.2: Summary of annealing temperature.

Publication	Annealing Temperature	Results
Sakata <i>et al.</i> [17]	Above 865 °C Below 860 °C At 800 °C At 986 °C	$\epsilon$ and $\alpha$ increased, $\beta$ decreased $\epsilon$ and $\alpha$ decreased, $\beta$ increased $\alpha \rightarrow \beta + \text{Si}$ , $\epsilon + \text{Si} \rightarrow \beta$ $\alpha + \epsilon \rightarrow \beta$
Yamauchi <i>et al.</i> [26]	Below 870 °C	$\alpha \rightarrow \beta + \text{Si}$ , $\alpha + \epsilon \rightarrow \beta$
Yamauchi <i>et al.</i> [28]	1007 – 1027 °C	$\beta \rightarrow \epsilon + \alpha$
Kojima <i>et al.</i> [50]	Above 855 °C Below 855 °C	$\alpha + \epsilon \rightarrow \beta$ $\alpha \rightarrow \beta + \text{Si}$ , $\epsilon + \text{Si} \rightarrow \beta$
Ur. S.C. [52]	At 830 °C At 1100 °C	$\alpha + \epsilon \rightarrow \beta$ $\alpha$ and $\epsilon$ formation

The first endothermic peak for 1<sup>st</sup> heating stage of FeSi<sub>2.0</sub> and FeSi<sub>2.3</sub> samples occurs at 960 °C. This peak shifts to higher temperature for 2<sup>nd</sup> and 3<sup>rd</sup> heating stage (at temperature range of 960-975 °C). Interestingly, this peak exists at 960 °C for all heating stages of FeSi<sub>2.5</sub> sample where initial sample contains only  $\alpha$ -phase. The endothermic peak at 960 °C corresponds to the eutectoid reaction ( $\alpha \rightarrow \beta + \text{Si}$ ). This reaction has been confirmed by SEM images (Fig. 4.13) and XRD patterns (Fig. 4.14) of the annealed samples at 950 °C. FeSi<sub>2.0</sub> and FeSi<sub>2.3</sub> samples have  $\epsilon$ - and  $\alpha$ -phases, the peritectoid reaction ( $\alpha + \epsilon \rightarrow \beta$ ) appears at 986 °C, quite close to the reported value 975 °C [26]. Therefore, the temperature range 960-975 °C consists of both peritectoid and eutectoid reactions. As-grown FeSi<sub>2.5</sub> sample do not consist of  $\epsilon$ -phase, only eutectoid reaction occurs at 960 °C.

The endothermic peaks at 1010 °C for FeSi<sub>2.0</sub> sample become smaller for FeSi<sub>2.3</sub> sample and disappear for FeSi<sub>2.5</sub> sample. This implies that this peak must be associated with  $\epsilon$ -phase. This peak has been identified as a reversed peritectoid reaction ( $\beta \rightarrow \alpha + \epsilon$ ) [52, 50]. Subsequent heating stage produced stronger 1010 °C endothermic peak because more  $\beta$ -phase was formed.

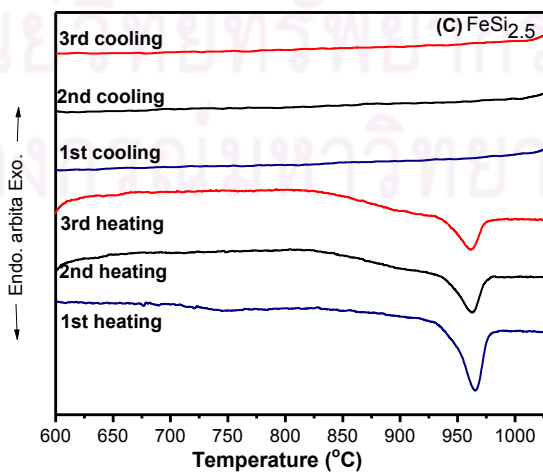
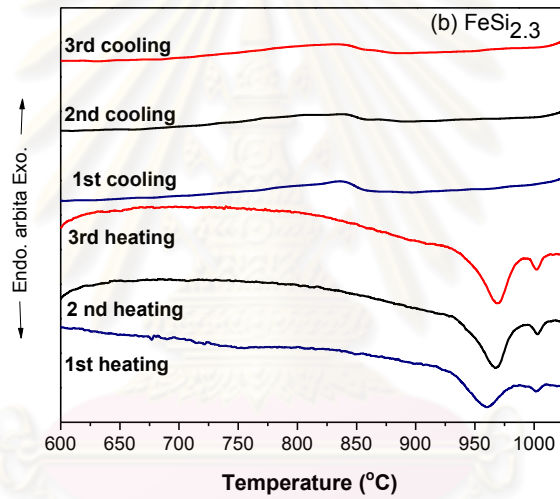
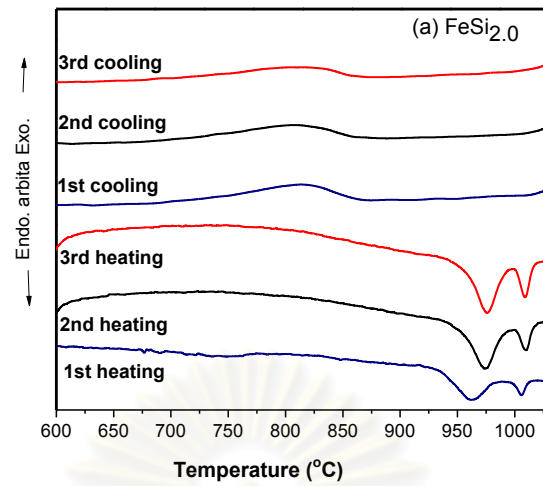


Figure 4.10: DTA curves of as-grown (a)  $\text{FeSi}_{2.0}$ , (b)  $\text{FeSi}_{2.3}$  and (c)  $\text{FeSi}_{2.5}$  samples.

## 4.5 Annealed Samples

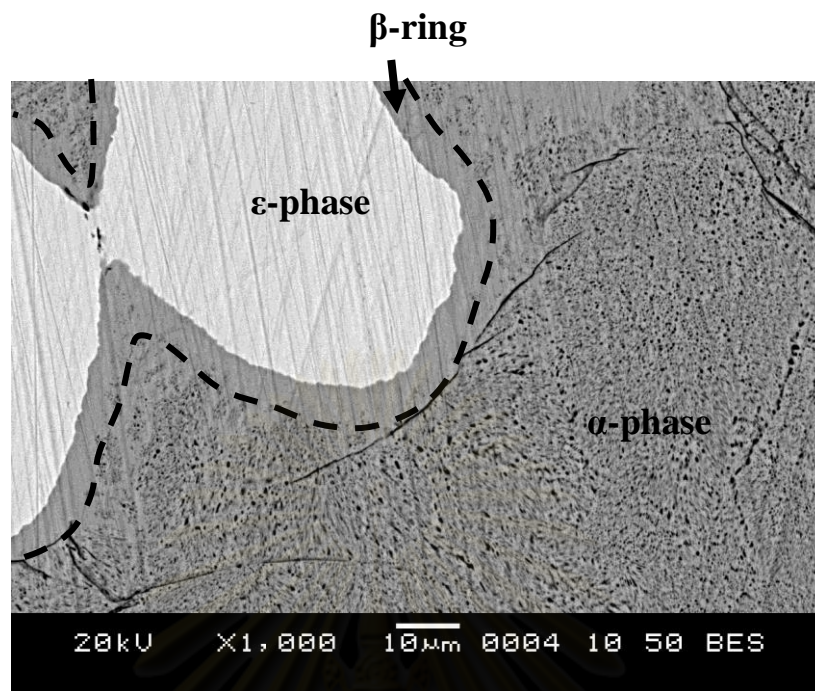
### 4.5.1 SEM Image

From the DTA results, the as grown samples were annealed specifically at 820 °C and 950 °C for 3, 6 and 12 h. Figure 4.11 shows microstructure of annealed FeSi<sub>2.0</sub> sample. In case of annealing at 820 °C for 6 h, a small ring-like structure  $\beta$ -phase layer formed around the  $\epsilon$ -phase due to the peritectoid reaction. The thickness of  $\beta$  ring is about 8 to 10  $\mu$ m. Yamauchi *et al.* [53] reported that the  $\beta$ -phase formation from peritectoid reaction gave the ring-like structure surrounding  $\epsilon$ -phase while the eutectoid structure gave the structure composed of  $\beta$ -phase and excessive strip line Si. Ito *et al.* [21] reported that the  $\beta$ -phase was obtained from sintered compacts through a heat treatment around 700-900 °C for about 100 h. Hsu *et al.*[31] synthesized a bulk  $\beta$ -FeSi<sub>2</sub> and reported that the optimal annealing condition ,yielding more  $\beta$ -phase of iron disilicide, were at 800 – 900 °C for over 300 h . Kakemoto *et al.* [29] successfully obtained a single  $\beta$ -FeSi<sub>2</sub> bulk crystal by annealing at 900 °C for 1000 h. The kinetics for this conversion has been known to be sluggish [26]. Therefore, it is not surprised that the thickness of  $\beta$  ring of the annealed sample at 820 °C for 12 h is similar to that of annealed sample for 6 h. This information has alarmed us that the starting amount and size of  $\epsilon$ -phase must be as small as possible to increase contact areas between the  $\epsilon$ - and  $\alpha$  phases.

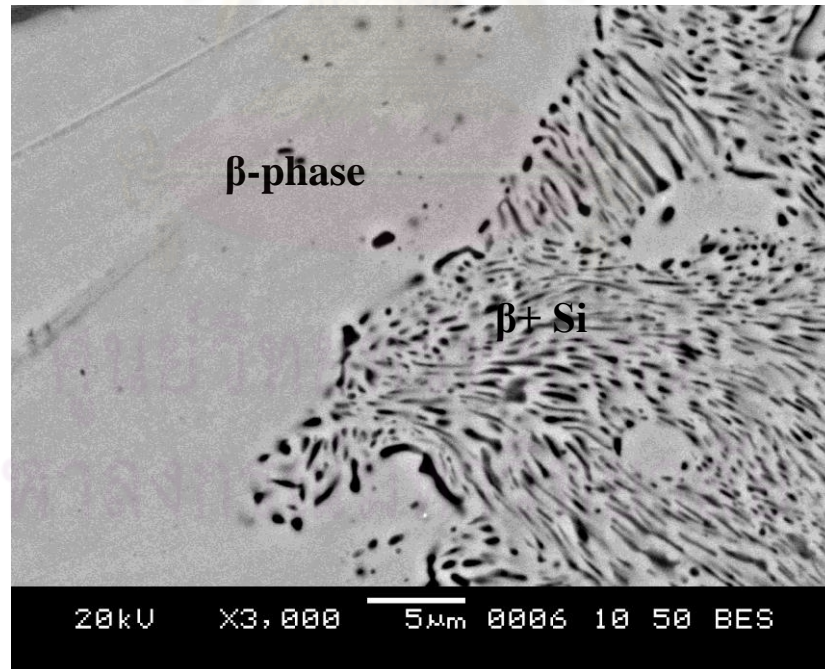
Table 4.3 shows EDS measurement of the annealed samples. For annealed FeSi<sub>2.5</sub> sample, the  $\beta$ -phase is not detectable because EDS analysis covers areas of  $\beta$ - and Si phases.

Table 4.3: EDS measurement of the annealed samples.

Sample condition	$\epsilon$ -phase (Fe:Si = 1:1)	$\beta$ -phase (Fe:Si = 1: 2)	$\alpha$ -phase (Fe:Si = 1: 2.5)
FeSi <sub>2.0</sub> annealing at 820 °C for 6 h	Fe:Si = 1 : 1.11	Fe:Si = 1 : 2.04	Fe:Si = 1 : 2.36
FeSi <sub>2.0</sub> annealing at 950 °C for 6 h	Fe:Si = 1 : 1.05	Fe:Si = 1 : 2.07	Fe:Si = 1 : 2.45
FeSi <sub>2.3</sub> annealing at 820 °C for 18 h /950 °C for 12 h	Fe:Si = 1 : 1.10	Fe:Si = 1 : 2.10	Fe:Si = 1 : 2.44
FeSi <sub>2.5</sub> annealing at 950 °C for 6 h	Not detectable	Not detectable	Fe:Si = 1 : 2.51



(a)



(b)

Figure 4.11: SEM image of  $\text{FeSi}_{2.0}$  sample annealed for 6 h at (a) 820 °C and (b) 950 °C.

Figure 4.11(b) shows SEM image at a magnification of 3000 of the annealed  $\text{FeSi}_{2.0}$  sample at  $950\text{ }^{\circ}\text{C}$ . Its structure shows Si network from eutectoid reaction and Si network disperses in the  $\beta$  matrix. At this temperature, pure  $\beta$ -phase occurred from peritectoid reaction as reported in DTA results.

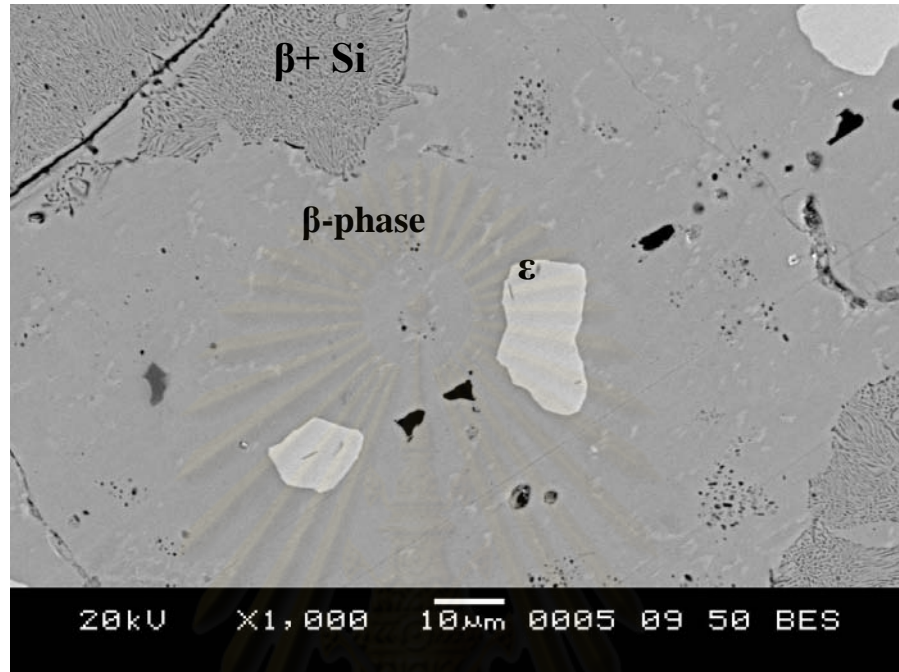


Figure 4.12: SEM image of  $\text{FeSi}_{2.3}$  sample annealed at  $820\text{ }^{\circ}\text{C}$  for 18 h and at  $950\text{ }^{\circ}\text{C}$  for 12 h.

For  $\text{FeSi}_{2.5}$  sample, the starting phase is  $\alpha$ -phase. SEM image after  $950\text{ }^{\circ}\text{C}$  annealing is shown in Fig.4.13. It shows that  $\alpha$ -phase decomposes to  $\beta$ - and Si- phases and Si particles were homogeneously distributed in the  $\beta$ -matrix. From table 4.3, the EDS analysis over a square millimeter covering  $\beta + \text{Si}$  area is equivalent to the composition of  $\alpha - \text{Fe}_2\text{Si}_5$ . It should be noted that 100%  $\beta$ -phase formation without  $\epsilon$  or  $\alpha$ -phases is from the eutectoid reaction only because it is difficult to get rid of  $\epsilon$ -phase by a few hour annealing.



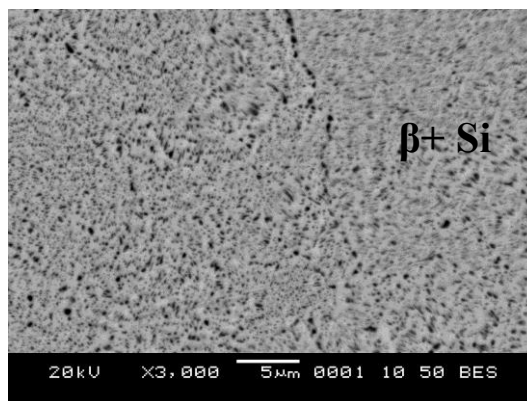


Figure 4.13: SEM image of the annealed  $FeSi_{2.5}$  sample at  $950\text{ }^{\circ}C$  for 6 h.

## 4.5.2 XRD Pattern

XRD pattern of  $FeSi_{2.3}$  after  $820\text{ }^{\circ}C$  annealing is shown in Fig. 4.14. At this annealing temperature, the  $\beta$ -formation occurs by the peritectoid reaction ( $\alpha + \epsilon \rightarrow \beta$ ). So, Si peak cannot be seen. These results are consistent with SEM and DTA results. The intensity of  $\beta$ -phase is not significantly different for 3, 6 and 12 h annealing time. XRD patterns of  $FeSi_{2.0}$ ,  $FeSi_{2.3}$  and  $FeSi_{2.5}$  samples annealed at  $950\text{ }^{\circ}C$  for 6 h are shown in Fig.4.15. It is clear that  $\beta$ -phase is formed by an observation of strong peak  $2\theta \approx 29.1^{\circ}$  (100% intensity) and  $2\theta \approx 49.4^{\circ}$  in all samples. For  $FeSi_{2.3}$  and  $FeSi_{2.5}$  samples, Si peak ( $2\theta \approx 28.4^{\circ}$ ) can be slightly seen as a result of eutectoid reaction. SEM micrograph of the annealed sample still shows pure  $\epsilon$ -phase, this might indicate that those pure  $\epsilon$ -phases are small in quantity and below detectable limit of XRD machine.

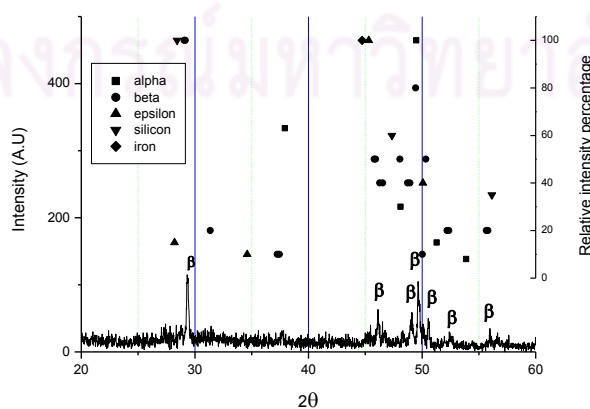
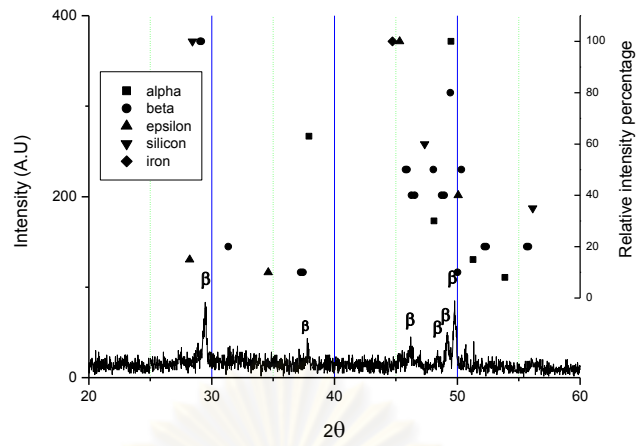
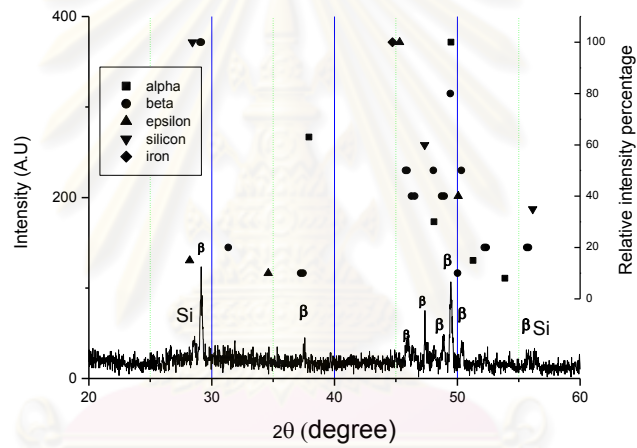


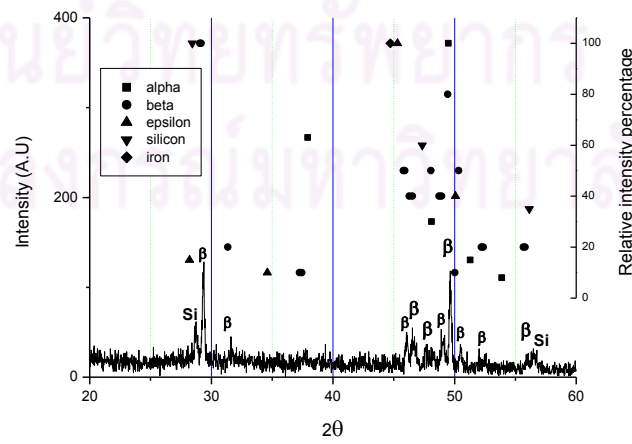
Figure 4.14: XRD patterns of sample  $FeSi_{2.3}$  annealed at  $820\text{ }^{\circ}C$  for 6 h.



(a)



(b)



(c)

Figure 4.15: XRD patterns of (a)  $FeSi_{2.0}$ , (b)  $FeSi_{2.3}$  and (c)  $FeSi_{2.5}$  samples annealed at  $950\text{ }^{\circ}C$  for 6 h.

## 4.6 Seebeck Coefficient

### 4.6.1 Seebeck Coefficient at Room Temperature

In this work, the Seebeck coefficient is positive for all compositions. According to our apparatus configuration, these mean that hole-like carrier dominates the transport. Unintentional doping of sample is due to the unknown impurity in raw materials and BN released agent used. Zhengxin *et al.* [54] studied the effect of doping  $\beta$ -FeSi<sub>2</sub> thin film with boron and arsenic by sputtering method. The results indicated that the  $\beta$ -FeSi<sub>2</sub> thin film doped with boron was p-type. The relation between the Si content and Seebeck coefficient was studied by several researchers. Tani *et al.* [55] studied the thermoelectric properties of FeSi<sub>x</sub> ( $1.9 \leq x \leq 2.4$ ). They reported that the Seebeck coefficient at room temperature for  $x = 1.90, 2.10$  and  $2.20$  was negative, while it was positive for  $x = 2.00, 2.05$  and  $2.40$ . The maximum Seebeck coefficient was  $-470 \mu\text{V/K}$  for  $x = 2.20$ . Komabayashi *et al.* [56] measured the Seebeck coefficient of the FeSi<sub>x</sub> films where  $x$  was in the range of  $1.64 < x < 2.32$ . In the region of  $x < 1.95$ , the Seebeck coefficient was small ( $10 - 30 \mu\text{V/K}$ ) while in the region of  $1.95 < x < 2.06$ , Seebeck coefficient increased with increasing  $x$ . The maximum value of Seebeck coefficient was found to be  $230 \mu\text{V/K}$  near  $x = 2.06$ . The Seebeck coefficient changes its sign near  $x = 2.08$  and was negative for  $x > 2.08$ .

Nagai [19] calculated the Seebeck coefficient of semiconducting  $\beta$ -phase with a dispersion of metallic  $\varepsilon$ -phase by following equation;

$$S = S(\beta)(1-f) + S(\varepsilon)f \quad (4.1)$$

where  $S$  is the total Seebeck coefficient,  $f$  is volume fraction of  $\varepsilon$ -phase and  $S(\beta)$  and  $S(\varepsilon)$  are Seebeck coefficient of  $\beta$  and  $\varepsilon$ -phases, respectively. At room temperature,  $S(\beta) = 250 \mu\text{V/K}$  and  $S(\varepsilon) = 2.6 \mu\text{V/K}$  [19].

From Eq. (4.1), the  $f$  value can be calculated by substituting  $S(\beta) = 250 \mu\text{V/K}$ ,  $S(\varepsilon) = 2.6 \mu\text{V/K}$  and  $S$  as presented in table 4.4. The relation between  $f$  value and annealing time is shown in Fig. 4.16. These data are obtained from this work, Refs. [52] and [53]. For the as-grown samples, the  $f$  value is equal to 1.0 because the  $\beta$ -phase does not occur. The  $f$  value decreases with increasing annealing time. From table 4.5, if the Si content is higher than the stoichiometric composition of FeSi<sub>2</sub>, the Seebeck

coefficient will be larger than the Seebeck coefficient of  $\beta$ -phase (250  $\mu\text{V/K}$ ). This may be due to the two-phase structure of  $\beta$ - matrix and Si dispersoids. The second phase dispersion in  $\beta$ -phase matrix is expected to increase scattering factor for carriers and phonons, which leads to higher Seebeck coefficient and lower thermal conductivity [13] especially below 330  $^{\circ}\text{C}$  [29].

Table 4.4: Summary of Seebeck coefficient at room temperature of this work and other publication.

Publication	Composition	Preparation Method	Seebeck coefficient ( $\mu\text{V/K}$ )
Yamauchi <i>et al.</i> [53]	$\text{FeSi}_2$	Melt and rapid solidification / Annealed at 890 $^{\circ}\text{C}$ for 20 h.	80
Ur. S.C.[52]	$\text{FeSi}_2$	- Hot-pressed / Annealed at 830 $^{\circ}\text{C}$ for 48 h	150
		- Thermal-sprayed / Annealed at 845 $^{\circ}\text{C}$ for 200 h	20
Tani, J. and Kido, H. [54]	$\text{FeSi}_{2.2}$	Melted in silica ampoules / Spark plasma sintering / Annealed at 840 $^{\circ}\text{C}$ for 168 h	- 470
This work	$\text{FeSi}_{2.0}$	Melted in alumina crucible /	137
	$\text{FeSi}_{2.3}$	Annealed at 950 $^{\circ}\text{C}$ for 12 h	150
	$\text{FeSi}_{2.5}$		270

Seebeck coefficient of our as-grown samples is relatively low (less than 10  $\mu\text{V/K}$ ) due to the metallic  $\alpha$ - and  $\varepsilon$ -phases dominance. Fig. 4.17 shows the result of Seebeck coefficient measured at room temperature for annealed  $\text{FeSi}_{2.0}$  and  $\text{FeSi}_{2.3}$  samples at 820  $^{\circ}\text{C}$  for various time durations. It can be seen that the Seebeck coefficient increases with increasing annealing time but it is not significantly different for 3, 6 and 12 h annealing time at 820  $^{\circ}\text{C}$ . This is because the peritectoid reaction occurring at this temperature takes very long time to complete whereby our annealing time are not long enough to obtain the completed  $\beta$ -phase.

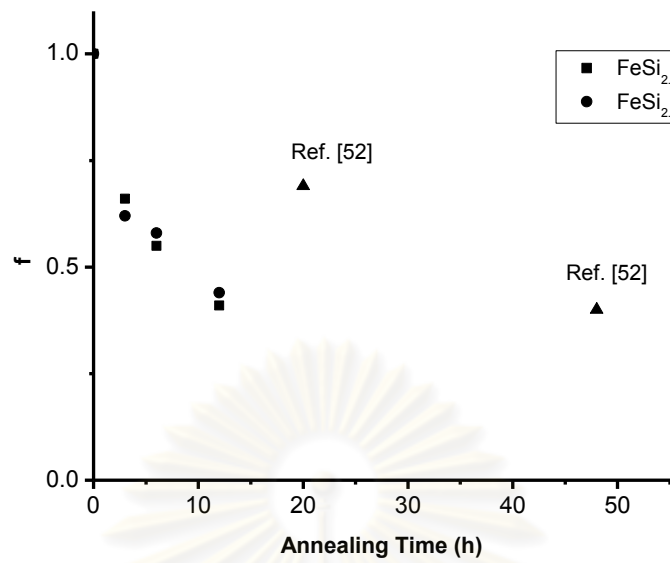


Figure 4.16: The volume fraction of  $\varepsilon$ -phase of annealed  $\text{FeSi}_{2.0}$  and  $\text{FeSi}_{2.3}$  samples.

Figure 4.18 shows the result of Seebeck coefficient at room temperature for the annealed  $\text{FeSi}_{2.0}$ ,  $\text{FeSi}_{2.3}$  and  $\text{FeSi}_{2.5}$  samples at  $950\text{ }^\circ\text{C}$  for various time duration. Seebeck coefficient increases with increasing annealing time. Highest value Seebeck coefficient is around  $270\text{ }\mu\text{V/K}$  for the annealed  $\text{FeSi}_{2.5}$  sample at  $950\text{ }^\circ\text{C}$  for 12 h.

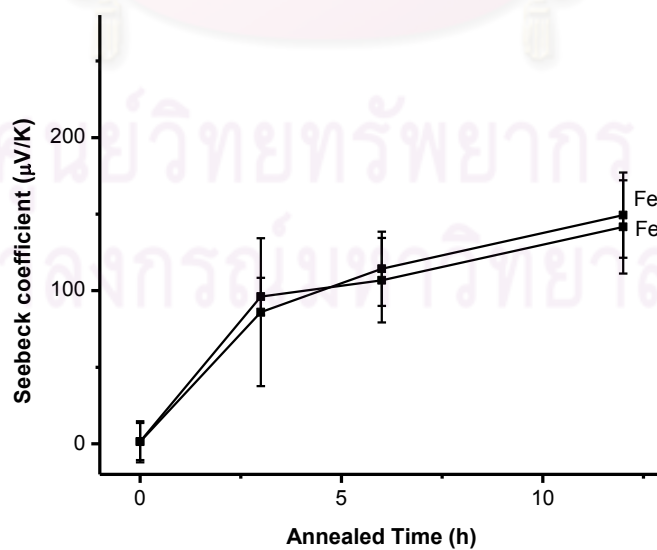


Figure 4.17: Seebeck coefficient of  $\text{FeSi}_{2.0}$  and  $\text{FeSi}_{2.3}$  samples annealed at  $820\text{ }^\circ\text{C}$  for different time.

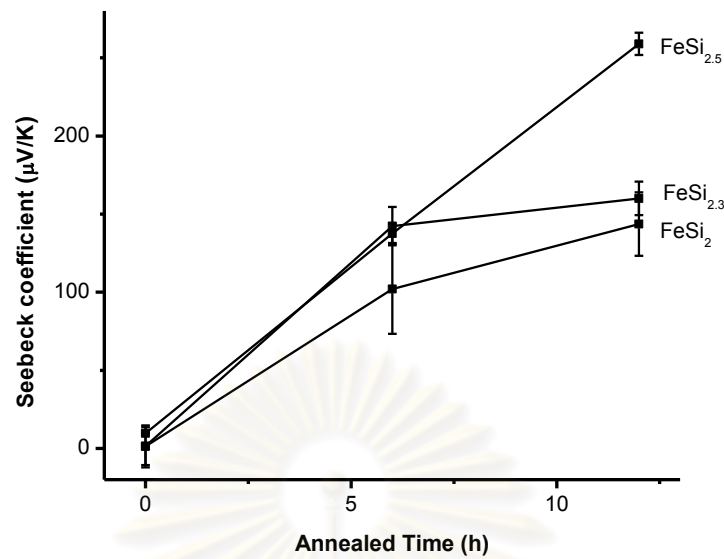


Figure 4.18: Seebeck coefficient of  $FeSi_{2.0}$ ,  $FeSi_{2.3}$  and  $FeSi_{2.5}$  samples annealed at  $950\text{ }^{\circ}\text{C}$  for different time.

Error bar represents a standard deviation from ten readings for one sample and it can be seen that the standard deviation of thermoelectric power for  $FeSi_{2.0}$  and  $FeSi_{2.3}$  samples are larger than that of  $FeSi_{2.5}$  sample. This would imply that non-homogeneity in  $FeSi_{2.0}$  and  $FeSi_{2.3}$  samples is higher than that in  $FeSi_{2.5}$  sample. We can explain this by using a model presented by Yamauchi *et al.* [28] as shown in Fig. 4.19, where the  $\beta$  and Si phases were produced by the eutectoid reaction ( $\alpha$ -decomposition) and a ring of  $\beta$ -phase around the  $\varepsilon$ -phase was produced by the peritectoid reaction. This  $\beta$  ring between  $\varepsilon$ - and  $\alpha$ -phases suppresses further peritectoid reaction. The endothermic peak at  $830\text{ }^{\circ}\text{C}$  of DTA curve was broadened due to sluggish process of peritectoid reaction. Therefore, thermoelectric power at any point on the surface of the samples is randomly different depending on the phase underneath the hot probe. On the other hand, as-grown  $FeSi_{2.5}$  sample consisted of  $\alpha$ -phase only and after annealing, that phase was transformed into  $\beta$ - and Si- phases. Both are semiconducting phases and have thermoelectric power much larger than the metallic  $\alpha$  phase.

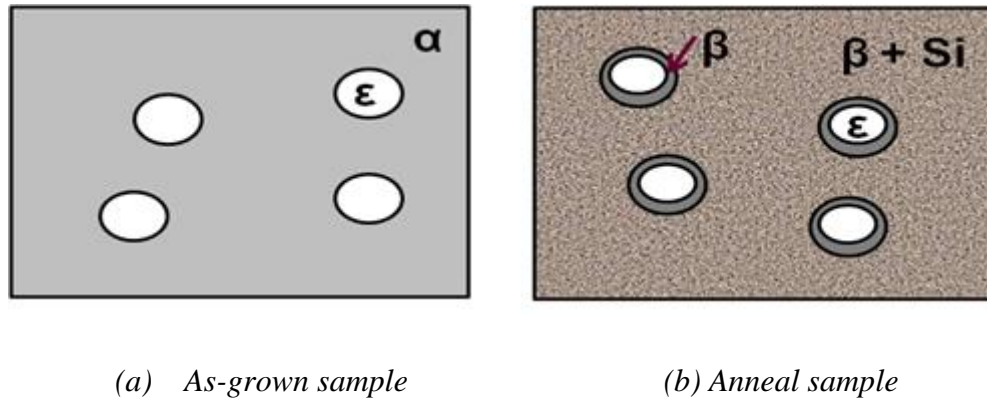


Figure 4.19: Schematic illustration of  $\beta$ -phase formation process [28].

#### 4.6.2 Temperature Dependence of Seebeck Coefficient

Figure 4.20 shows the temperature dependence of the Seebeck coefficient for  $\text{FeSi}_{2.0}$ ,  $\text{FeSi}_{2.3}$  and  $\text{FeSi}_{2.5}$  samples over the temperature range of 30 – 700 °C. The Seebeck coefficient increases with increasing temperature and then decreases at high temperature. The marked decrease in the Seebeck coefficient at high temperature is due to the marked increase in the carrier concentration. The Seebeck coefficients of the  $\text{FeSi}_{2.5}$  samples are significantly higher than that of the  $\text{FeSi}_{2.0}$  and  $\text{FeSi}_{2.3}$  samples. This result can be explained by two reasons, the existence of metallic  $\epsilon$ -phase in annealed  $\text{FeSi}_{2.0}$  and  $\text{FeSi}_{2.3}$  samples as presented in SEM images and the influence of excess Si on the carrier scattering. The Seebeck coefficient of the  $\text{FeSi}_{2.3}$  sample is larger than  $\text{FeSi}_{2.0}$  sample. This is probably due to the amount of  $\epsilon$ -phase in  $\text{FeSi}_{2.3}$  is less than  $\text{FeSi}_{2.0}$  as presented in XRD pattern. Furthermore, the small excess Si particle in  $\text{FeSi}_{2.3}$  promotes the value of Seebeck coefficient. At temperature below 500 °C, the Seebeck coefficient of all samples are largely composition dependence. The difference in Seebeck coefficient of all samples decreases with increasing temperature. This result is consistent with the work of Tani *et al.* [54] and Zhao *et al.* [27]. The carriers scattering by excess Si is sensitive at below 450 °C [53]. At high temperature, number of carriers increase so the influence of excess Si becomes insensitive. Peaks in the Seebeck coefficient generally appear near or above 330 °C in  $\text{FeSi}_{2.0}$  depending on the processing method, such as in hot pressed [55], and in pressureless sintering [56]. In this work, the maximum Seebeck coefficient for  $\text{FeSi}_{2.0}$

is  $150 \mu\text{V/K}$  at  $500 \text{ }^\circ\text{C}$ . For  $\text{FeSi}_{2.3}$ , the maximum Seebeck coefficient is  $225 \mu\text{V/K}$  at  $400 \text{ }^\circ\text{C}$ . Finally, the maximum Seebeck coefficient is  $300 \mu\text{V/K}$  at  $350 \text{ }^\circ\text{C}$  for  $\text{FeSi}_{2.5}$ .

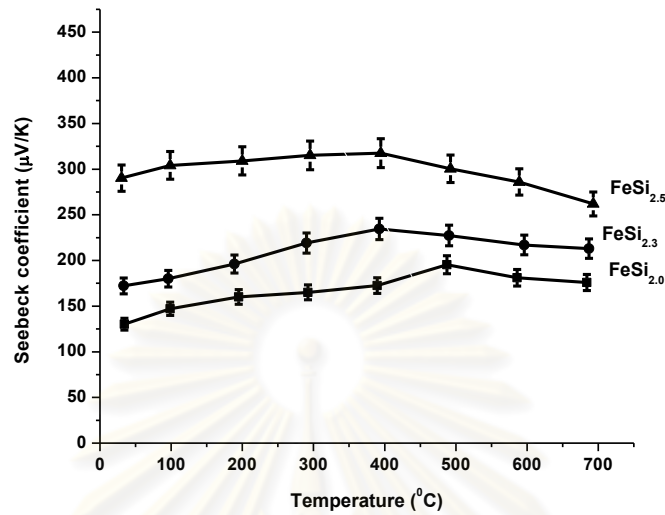


Figure 4.20: Temperature dependence of Seebeck coefficient of  $\text{FeSi}_{2.0}$ ,  $\text{FeSi}_{2.3}$  and  $\text{FeSi}_{2.5}$ .

## 4.7 Electrical Conductivity

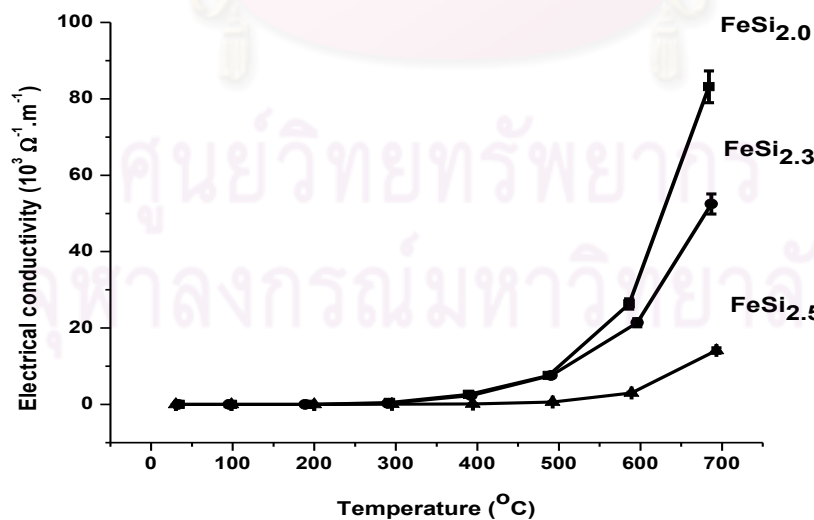


Figure 4.21: Temperature dependence of electrical conductivity of  $\text{FeSi}_{2.0}$ ,  $\text{FeSi}_{2.3}$  and  $\text{FeSi}_{2.5}$ .



Figure 4.21 shows the temperature dependence of electrical conductivity for annealed samples over the temperature range 30 – 700 °C by the DC four-terminal method. The electrical conductivity of all samples produces the same characteristic curve below 400 °C and then increases rapidly with increasing temperature. The values of electrical conductivity at high temperature are strongly dependent on composition of sample. The electrical conductivity of FeSi<sub>2.0</sub> is higher than FeSi<sub>2.3</sub> and the electrical conductivity of FeSi<sub>2.3</sub> is higher than FeSi<sub>2.5</sub>. These can be explained by the influence of metallic  $\epsilon$ -phase as present in the FeSi<sub>2.0</sub> and FeSi<sub>2.3</sub> samples.

From Eq. (2.26), the  $\log \sigma - \frac{1000}{T}$  is plotted for all samples as shown in Fig. 4.22.

The results are fitted at high temperature region by

$$\sigma(T) = \sigma_0 \exp\left(\frac{-E_g}{k_B T}\right)$$

where  $\sigma_0$  is pre-exponential factor,  $k_B$  is Boltzmann constant =  $8.617 \times 10^{-5}$  eV/ K and  $E_g$  is energy gap.

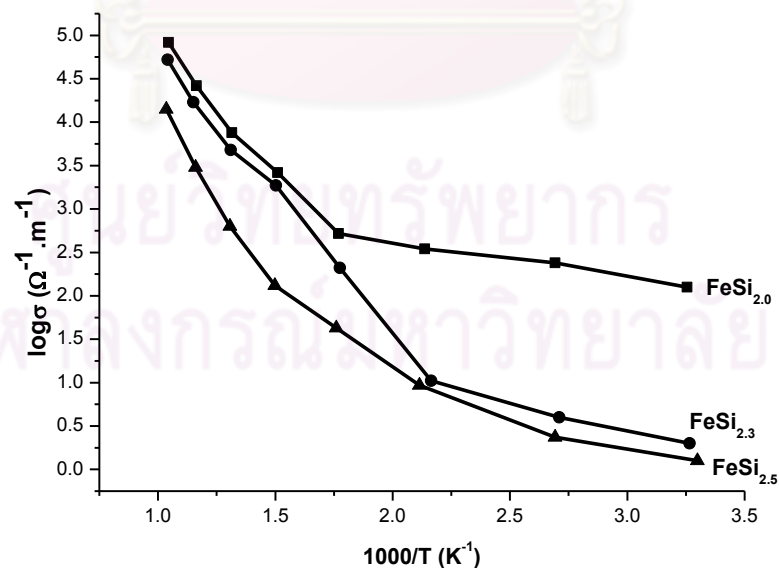


Figure 4.22:  $\log \sigma$  versus  $1000/T$  for temperature dependent conductivity.

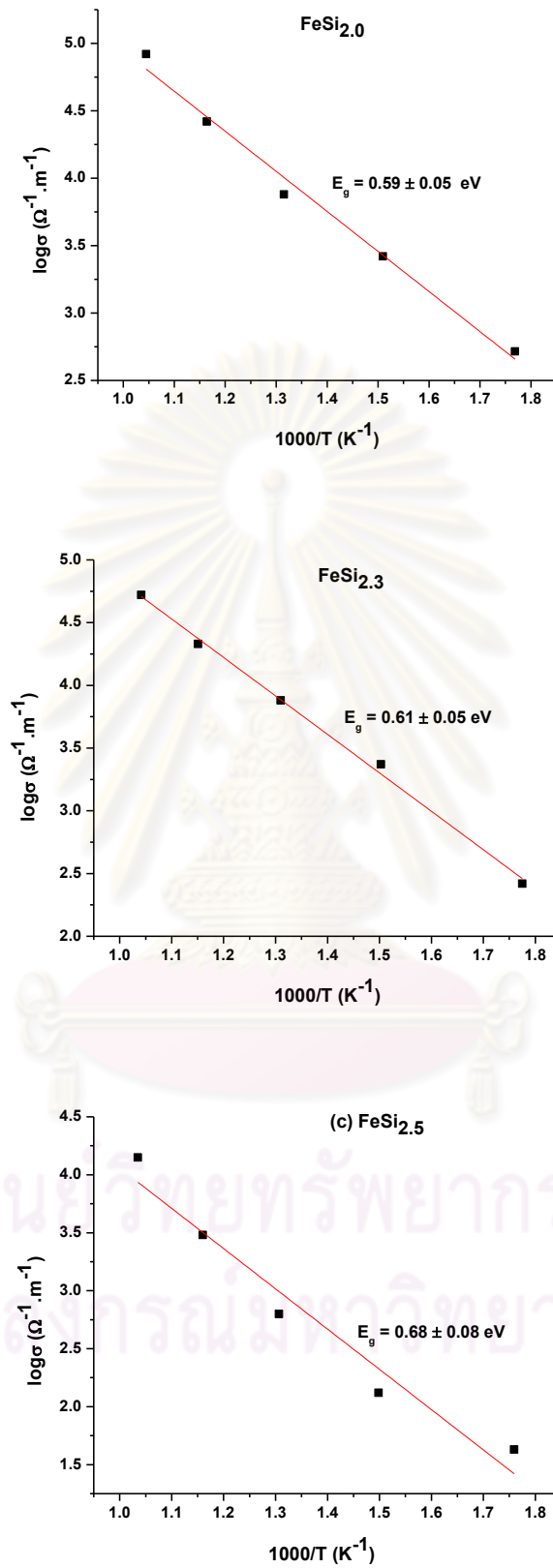


Figure 4.23: The calculation of energy gap from slope at high temperature of  $\log \sigma - \frac{1000}{T}$  plots of (a) FeSi<sub>2.0</sub>, (b) FeSi<sub>2.3</sub> and (c) FeSi<sub>2.5</sub>.

The energy gap can be calculated by slope at high temperature of  $\log \sigma - \frac{1000}{T}$  plots as shown in Fig. 4.23. At high temperature region,  $\sigma - \frac{1000}{T}$  plots correspond to an intrinsic conduction region. In our measurement, the temperature ranges from 300 to 973 K and we estimate that the mobility, which is inversely proportional to  $T^{-3/2}$ , will decrease by 17.5%. Therefore, we would take  $\frac{17.5\%}{2} = 8.56\%$  as the uncertainty in mobility. The uncertainty will be incorporated into the energy gap calculation as well. The energy gap of FeSi<sub>2.0</sub>, FeSi<sub>2.3</sub> and FeSi<sub>2.5</sub> are calculated to be 0.59 eV, 0.61 eV and 0.69 eV, respectively. It has been reported that the energy gap of  $\beta$ -FeSi<sub>2</sub> bulk crystal estimated to be 0.85 eV [29] and 0.82 – 0.88 eV [58]. In this work, the energy gap of all samples is smaller than the publications of Kakemoto. *et al.*[29] and Kuei *et al.*[58] This is probably due to existence of metallic  $\epsilon$ -phase in FeSi<sub>2.0</sub> and FeSi<sub>2.3</sub> samples which reduces the energy gap. FeSi<sub>2.0</sub> has the highest  $\epsilon$ -phase and therefore the lowest energy gap.

## 4.8 Thermal Conductivity

Figure 4.24 shows the temperature dependence of the thermal conductivity,  $K_{total}$ , of all samples annealed at 950 °C for 12 h. A plot of  $K_{total}$  versus temperature of all samples has a U-shape with minimum value around 300 °C. At every temperature, the  $K_{total}$  decrease with Si content of FeSi<sub>x</sub>. As described above, the excess Si dispersed in  $\beta$ -matrix is effective for a decrease in the  $K_{total}$ . The temperature corresponds to the minimum  $K_{total}$  decreases with increasing Si content. This is consistent with Seebeck coefficient result, the influence of excess Si particles is much stronger at lower temperature than at higher temperature.

The electronic contribution to the thermal conductivity,  $K_{el}$ , has been calculated using Wiedemann-Franz law;  $K_{el} = L\sigma T$ , where  $L$  is Lorenz number,  $\sigma$  is electrical conductivity and  $T$  is the absolute temperature. The lattice contribution,  $K_{ph}$ , is obtained by subtracting  $K_{el}$  from  $K_{total}$ . The temperature dependence of  $K_{el}$  and  $K_{ph}$  for all samples are shown in Fig. 4.25.

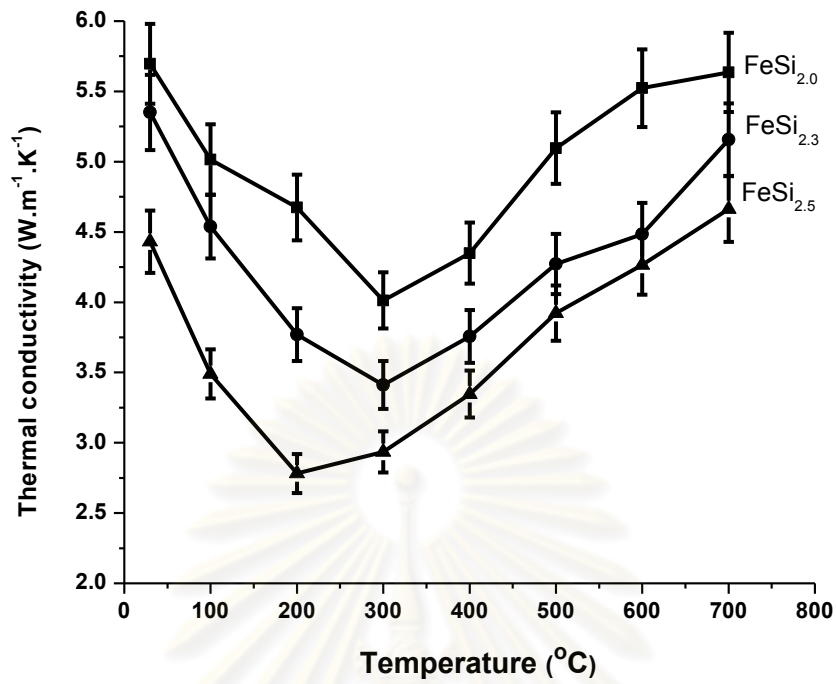


Figure 4.24: Temperature dependence of the thermal conductivity of  $\text{FeSi}_{2.0}$ ,  $\text{FeSi}_{2.3}$  and  $\text{FeSi}_{2.5}$ .

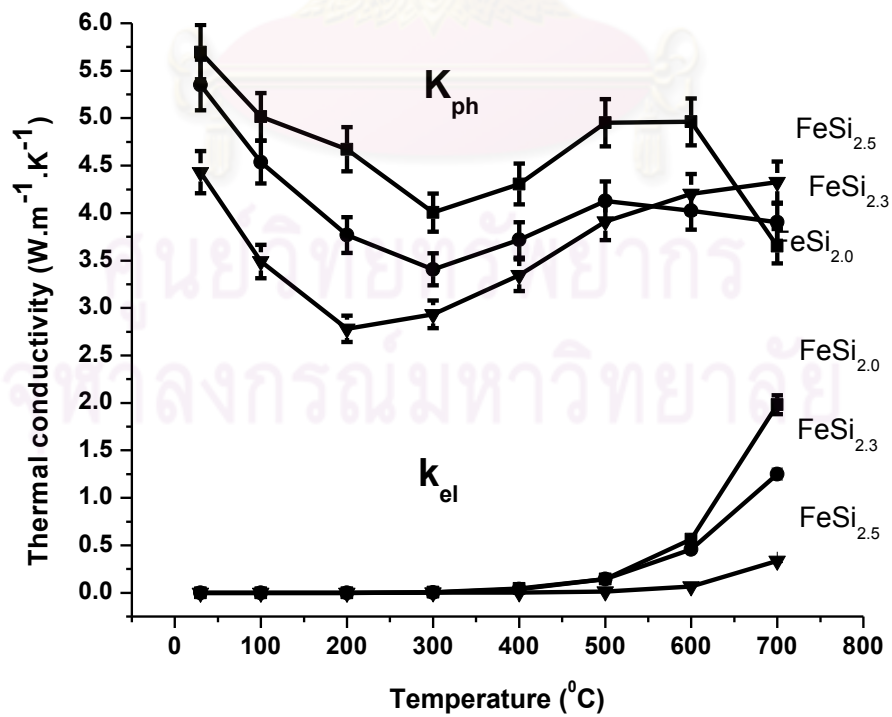


Figure 4.25: Temperature dependence of  $K_{el}$  and  $K_{ph}$  of  $\text{FeSi}_{2.0}$ ,  $\text{FeSi}_{2.3}$  and  $\text{FeSi}_{2.5}$ .

The influence of electronic contribution on thermal conductivity is rather small in comparison with the lattice contribution and  $K_{el}$  is almost independent of the amount of Si at temperature lower than 500 °C. However,  $K_{el}$  increases at high temperature due to the increase in the electronic carrier.

Waldecker, *et al* [59] reported that the Debye temperature of  $\beta$ -FeSi<sub>2</sub> was 370 °C. From classical kinetic theory of gases,  $K_{ph} \propto T^3$  at the temperature lower than Debye temperature. The results in Fig.4.24 contrast the theoretical prediction, indicating the strong lattice vibration scattering. In higher temperature range, the thermal conductivity of all samples increases with increasing temperature because of the increase in both charge carriers and phonon concentration. For FeSi<sub>2.0</sub>, the  $K_{ph}$  decreases at temperature higher than 600 °C. This is probably due to phonon- charge carriers scattering.

#### 4.9 Figure of Merit

The calculated dimensionless figure of merit,  $ZT$ , from Seebeck coefficient, electrical conductivity and thermal conductivity are shown in Fig.4.26. This work uses a B-spline to interpolate the eight points of Seebeck coefficient, electrical conductivity and thermal conductivity. The  $ZT$  value is calculated at 30 °C, 100 °C, 200 °C, 300°C, 400°C, 500 °C, 600 °C and 700 °C. The  $ZT$  of all samples increases with increasing temperature. It is surprising that the highest value of  $ZT = 0.48$  at 700 °C is obtained from FeSi<sub>2.3</sub> sample. For FeSi<sub>2.0</sub> and FeSi<sub>2.5</sub> samples, the highest values of  $ZT$  are 0.44 and 0.20 at 700 °C, respectively. In the case of FeSi<sub>2.5</sub> sample, although it shows maximum Seebeck coefficient, the thermal conductivity is minimum due to existence of excess Si. The FeSi<sub>2.5</sub> sample shows very low electrical conductivity compared with FeSi<sub>2.0</sub> and FeSi<sub>2.3</sub> samples. From this result, the  $ZT$  of FeSi<sub>2.5</sub> sample is smaller than other samples. In this work, the results indicate that the small metallic  $\epsilon$ -phase and excess Si in FeSi<sub>2.3</sub> sample markedly increase the  $ZT$ .

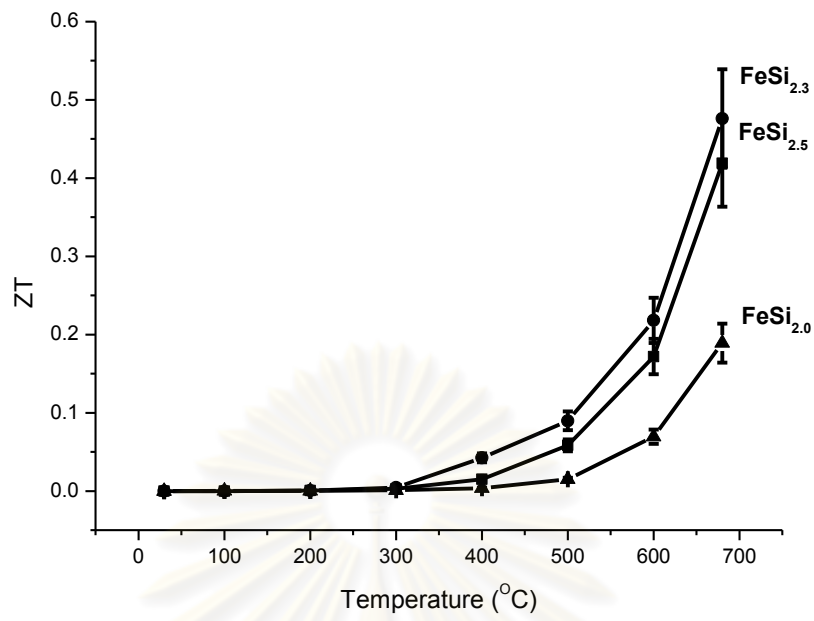


Figure 4.26: Temperature dependence of dimensionless figure of merit of  $FeSi_{2.0}$ ,  $FeSi_{2.3}$  and  $FeSi_{2.5}$  samples.

ศูนย์วิทยทรัพยากร  
จุฬาลงกรณ์มหาวิทยาลัย

# CHAPTER V

## CONCLUSION

Bulk Fe-Si compounds were synthesized by a simple thermal method. There were three compositions to be studied, FeSi<sub>2.0</sub>, FeSi<sub>2.3</sub> and FeSi<sub>2.5</sub>. A mixture of Fe and Si powder was melted at 1550 °C for 1 h in an inert gas. All samples were annealed at 820 °C or 950 °C for 3, 6 and 12 h. The structural and the thermoelectric properties of all samples were investigated. The results obtained in this study were as follows.

1. From XRD patterns and SEM images, the as-grown FeSi<sub>2.0</sub> and FeSi<sub>2.3</sub> samples composed of  $\epsilon$ - and  $\alpha$ -phases while as-grown FeSi<sub>2.5</sub> purely composed of  $\alpha$ -phase. The amount and size of  $\epsilon$ -phase seem to be independent of melting temperature but it decreased with increasing Si content.
2. From standard deviation of Seebeck coefficient at room temperature measured by a hot-probe technique, we could imply that non-homogeneity in FeSi<sub>2.0</sub> and FeSi<sub>2.3</sub> samples was higher than that in FeSi<sub>2.5</sub> sample.
3. DTA curves for FeSi<sub>2.0</sub> and FeSi<sub>2.3</sub> showed two endothermic peaks in the temperature range 960 - 1010 °C and one exothermic peak around 830 °C corresponded to peritectoid and eutectoid reaction, reversed peritectoid reaction and peritectoid reaction, respectively. DTA curves for FeSi<sub>2.5</sub> showed only endothermic peaks at 960 °C corresponded to eutectoid reaction.
4. After subsequent annealing at 820 °C and 950 °C in FeSi<sub>2.0</sub> and FeSi<sub>2.3</sub> samples and annealing at 950 °C in FeSi<sub>2.5</sub> sample for 3, 6 and 12 h, the XRD patterns and SEM images showed  $\beta$ -phase formation with some residual  $\epsilon$ -phase in FeSi<sub>2.0</sub> and FeSi<sub>2.3</sub> samples and some excess Si in FeSi<sub>2.3</sub> and FeSi<sub>2.5</sub> samples.
5. All samples were p-type with positive Seebeck coefficient and it tended to increase with increasing annealing time. The maximum Seebeck coefficient was 320  $\mu\text{V/K}$  at 400 °C for FeSi<sub>2.5</sub>, annealed at 950 °C for 12 h.
6. The minimum thermal conductivity was 2.75  $\text{W}\cdot\text{m}^{-1}\cdot\text{K}^{-1}$  at 200 °C for FeSi<sub>2.5</sub> annealed at 950 °C for 12 h. The influence of electronic contribution on thermal

conductivity is small in comparison with the lattice contribution and  $K_{el}$  is almost independent of the amount of Si at temperature lower than 500 °C.

7. The temperature-dependent electrical conductivity measurement ( $30\text{ °C} < T < 700\text{ °C}$ ) exhibited semiconducting features with its conductivity increased with increasing temperature. The maximum electrical conductivity of  $80\ \Omega^{-1}\cdot\text{m}^{-1}$  at 700 °C for  $\text{FeSi}_{2.0}$  annealed at 950 °C for 12 h. Using  $\log \sigma-1/T$  plot, the value of energy band gap were 0.59 eV, 0.61 eV and 0.69 eV for  $\text{FeSi}_{2.0}$ ,  $\text{FeSi}_{2.3}$  and  $\text{FeSi}_{2.5}$  respectively.

8. The dispersion of excess Si markedly increased the Seebeck coefficient and decreased the thermal conductivity of both  $\text{FeSi}_{2.3}$  and  $\text{FeSi}_{2.5}$  samples especially at low temperature while the present of metallic  $\epsilon$ -phase markedly increased the electrical conductivity of both  $\text{FeSi}_{2.0}$  and  $\text{FeSi}_{2.3}$  samples.

9. The  $\text{FeSi}_{2.3}$  sample annealed at 950 °C for 12 h showed the highest dimensionless figure of merit of 0.48 at 700 °C.

Although the dimensionless figure of merit of  $\text{FeSi}_{2.3}$  is the highest but the present of  $\epsilon$ -phase which causes electrical short circuit in producing thermoelectric cell and sometimes it takes more than 4 days for complete  $\beta$ -phase formation. These are the most important problems for the commercial use of this material. Furthermore, the one objective of this work is synthesizing homogeneous  $\text{FeSi}_2$  by short processing time and inexpensive process. So the  $\text{FeSi}_{2.5}$  is the most suitable composition. In order to improve the dimensionless figure of merit of  $\text{FeSi}_{2.5}$ , the electrical conductivity should be improved by doping the  $\text{FeSi}_{2.5}$  with Co to n-type or doping with Mn to p-type.



## References

- [1] Data obtained from database of ISI Web of Knowledge [Online]. 2008.  
Available from : [http // www.isiwebofknowledge.com](http://www.isiwebofknowledge.com).
- [2] Nolas, G.S., et al. Thermoelectrics basic principles and new materials developments. Springer. Berlin. 2001.
- [3] Material and Technologies for direct thermal-to-electric energy conversion.  
In Yans, J., et al. (eds.), MRS Symposium Proceedings Vol. 886.
- [4] Terasaki, I., et al. Large thermoelectric power in  $\text{NaCo}_2\text{O}_4$  single crystals.  
Phys Rev. B 56 (1997): R12685 –R12687.
- [5] Snyder, G.J., and Toberer, E.S. Complex thermoelectric materials. Nature Mater. 7(2008):105-114.
- [6] Nolas, G.S., et al. Recent developments in bulk thermoelectric materials.  
Mater. Res.Soc. Bull 31 (2006): 199-205.
- [7] Venkatasubramanian, R., et al. Thin film thermoelectric devices with high room temperature figures of merit. Nature , 413(2001):597- 602.
- [8] Slack, G.A. CRC handbook of Thermoelectrics : Boca Raton, CRC Press, 1995.
- [9] Staneff, G. High-pressure Synthesis of Thermoelectric Materials. Doctoral dissertation, California Institute of Technology, 2005.
- [10] Nolas, G.S., et al. The effect of rare-earth filling on the lattice thermal conductivity of skutterudites. J. Appl. Phys 79 (1996):4002-4007.
- [11] Cohn, G.S., et al. Glasslike heat conduction in high-mobility crystalline semiconductors. Phys. Rev. Lett 82 (1999):779-782.
- [12] Stabler, F.R. Electric energy conversion. Mater. Res. Soc. Symp. Proc., 886 (2006): 433-438.
- [13] Nishida, I. Study of semiconductor-to-metal transition in Mn-dope  $\text{FeSi}_2$ .  
Phys. Rev. B 7 (1970):2710-2715.
- [14] Birkholz, U., and Schelm, J. Mechanism of electrical conduction in  $\beta\text{-FeSi}_2$ .  
Phys. Status Solidi 27 (1968): 413-425.
- [15] Dusausoy, Y., et al. Structure crystalline du disiliciure de fer  $\text{FeSi}_2$ . Acta. Cryst. B 27 (1971):1209-1218.

- [16] Umemoto, M. Preparation of thermoelectric  $\beta$ -FeSi<sub>2</sub> doped with Al and Mn by mechanical alloying. Mater. Trans., JIM 36 (1995): 373-383.
- [17] Sakata, T., et al. Studies on the formation of FeSi<sub>2</sub> from the FeSi-Fe<sub>2</sub>Si<sub>5</sub> eutectic. J. Less Common Metals 61 (October 1978): 301-308.
- [18] Hultgren, R., et al. Selected value of binary alloy. Am.Soc.for Metals (1973): 873.
- [19] Nagai, H. Effects of mechanical alloying and grinding on the preparation and thermoelectric properties of  $\beta$ -FeSi<sub>2</sub> (overview). Mater Trans., JIM 36 (1995): 363-372.
- [20] Ur, S.C., and Kim, I.H. Phase transformation and thermoelectric properties of n-type Fe<sub>0.98</sub>Co<sub>0.02</sub>Si<sub>2</sub> processed by mechanical alloying. Mater Lett 57 (2002): 543-551.
- [21] Ito, M., et al. Thermoelectric performance of n-type and p-type  $\beta$ -FeSi<sub>2</sub> prepared by pressureless sintering with Cu addition. J. Alloys Compd. 319 (2001):303-311.
- [22] Ito, M., et al. Effects of Al and Cu addition on pressureless sintering behavior and phase transformation of  $\beta$ -FeSi<sub>2</sub>. Mater. Trans., JIM 41 (2000): 857-864.
- [23] German, R.M. Liquid phase sintering. New York: Plenum Publishing Corporation, 1985.
- [24] Nagai, H., et al. Thermoelectric properties of  $\beta$ -FeSi<sub>2</sub> mechanical alloyed with Si and C. Mater. Trans., JIM. 39 (1998): 1140-1145.
- [25] Ito, M., et al. Thermoelectric properties of Fe<sub>0.98</sub>Co<sub>0.02</sub>Si<sub>2</sub> with ZrO<sub>2</sub> and rare-earth oxide dispersion by mechanical alloying. J. Alloys Compd. 350 (2003):296-302.
- [26] Yamauchi, I., et al. Effect of Cu addition on the  $\beta$ -phase formation rate in Fe<sub>2</sub>Si<sub>5</sub> thermoelectric materials. J. Mater. Sci. 33 (1998): 385-394.
- [27] Zhao, X.B., et al. Transport properties of rapid solidified Fe-Si-Mn-Cu thermoelectric semiconductor alloy. J. Alloys Compd. 306 (2000) :303-306.
- [28] Yamauchi, I., et al. Effect of copper addition on the  $\beta$ -phase formation rate in FeSi<sub>2</sub> thermoelectric materials. J. Mater. Sci. 32 (1997): 4603-4611.

- [29] Kakemoto, H., et al. Synthesis and properties of semiconducting Iron Disilicide  $\beta$ -FeSi<sub>2</sub>. Jpn.J.Appl.Phys. 38 (1999):5192-5199.
- [30] Shibata, H., et al. Electrical properties of  $\beta$ -FeSi<sub>2</sub> bulk crystal grown by horizontal gradient freeze method. 15<sup>th</sup> International Conference on Thermoelectrics (1996): 62-66.
- [31] Hsu, Y.K., et al. Synthesis of bulk  $\beta$ -FeSi<sub>2</sub> crystal. Jpn.J.Appl.Phys. 41 (2002):3854-3859.
- [32] Oikawa, Y., and Ozaki, H. Direct formation of  $\beta$ -FeSi<sub>2</sub> in evacuated fused ampoule. Intermetallics 10 (2002): 391-397.
- [33] Yilbas, B.S. Laser short-pulse heating of metallic surface: Consideration of Seebeck coefficient. Current Appl. Phys. 9 (2009): 496-504.
- [34] Mott, N.F., and Jones, H. The theory of properties of metals and alloys. Dover, New York 1958, 311.
- [35] Chester, G.V., and Thellung, A. The law of Wiedemann and Franz. In Proceeding of the Physical Society (1960): 1005-1013.
- [36] Maxim, G., et al. Physical Rev. B 72(November 2005): 205107-1 – 205107-5.
- [37] Kumar, G.S., and Prasad, G. Review experimental determinations of the Lorenz number. J. Material Sci. 28 (1993): 4261-4272.
- [38] Nolas, G.S., et al. In Thermoelectrics basic principles and new materials developments; Springer: Verlag, Berlin, Heidelberg, 2001, 12-13.
- [39] Wood, C. Materials for thermoelectric energy conversion Rep. Prog. Phys., 51(1988): 459-463.
- [40] Herring, C. Theory of the thermoelectric power of semiconductors. Phys. Rev. 96(1954) :1163-1187.
- [41] Sze, S.M.: Semiconductor Devices (Wiley, New York 1985) : 33.
- [42] Ioffe, A.F., Semiconductor thermoelements and thermoelectric cooling information, London: Infosearch, 1957.
- [43] Lambrecht, H., et al. Thermoelectric energy conversion-overview of a TPV alternative. AIP conf. Proc. 738 (November, 2004): 24-32.
- [44] Figure obtained from brochure [Online]. 2008. Available from: [http://www.lentonfurnaces.com/doclib/lenton\\_furnace\\_brochure.pdf](http://www.lentonfurnaces.com/doclib/lenton_furnace_brochure.pdf).

- [45] Figure obtained from product of LECO Corporation [Online]. 2010. Available from: [http://www.leco.com/products/metallography/sectioning\\_machine/vc\\_50/vc\\_50.htm](http://www.leco.com/products/metallography/sectioning_machine/vc_50/vc_50.htm).
- [46] Schweitzer, J. How does a SEM work [Online]. 2010. Available from: <http://www.purdue.edu/rem/rs/sem.htm>.
- [47] Figure obtained from ULAVA Technologies, Inc. Thermal analysis/R&D. 2010. Available from: <http://www.ulvac.com/thermal/zem%203.asp>
- [48] Tani, J. and Kido, H. Thermoelectric properties of Al-doped  $Mg_2Si_{1-x}Sn_x$  ( $x \leq 0.1$ ). J. Alloy. Comp. 466 (2008):335-340.
- [49] Kloc, C., et al. Preparation and properties of FeSi,  $\alpha$ -FeSi<sub>2</sub> and  $\beta$ -FeSi<sub>2</sub> single crystals. J. Alloy. Comp. 219 (1995):93-96.
- [50] Kojima, T., et al. Formation of  $\beta$ -FeSi<sub>2</sub> from the sintered eutectic alloy FeSi-Fe<sub>2</sub>Si<sub>5</sub> doped with cobalt. J. Less-Comm.Met. 159 159 (1990):299-305.
- [51] Takigawa, Y., et al. Eutectic  $\alpha$ -Fe<sub>2</sub>Si<sub>5</sub> and  $\epsilon$ -FeSi formed in an arc furnace showed a three layer structure. Jpn. J Appl. Phys. 40 (2001): 6927-6928.
- [52] Ur, S.C., and Kim, I. H. Thermoelectric properties of mechanically alloyed iron disilicides consolidated by various processes. Met. Mater. Int. 11 (2005):301-308.
- [53] Yamauchi, I., et al.  $\beta$ -FeSi<sub>2</sub> phase formation from a unidirectionally solidified rod-type eutectic structure composed of both  $\alpha$ - and  $\epsilon$ - phases. Mater.Sci. Eng. A 208 (1996):108-115.
- [54] Tani, J. and Kido, H. Hall effect and thermoelectric properties of FeSi<sub>x</sub>. J.Appl. Phys. 39 (2000) :1054-1057.
- [55] Komabayashi, M., et al. The composition dependence of some electrical properties of FeSi<sub>x</sub> thin films. Jpn. J. Appl. Phys. 29 (1990) :1118-1121.
- [56] Zhengxin, L., et al., Doping of  $\beta$ -FeSi<sub>2</sub> films with boron and arsenic by sputtering and its application for optoelectronic devices. Opt. Mater., 27(2005): 942-947.

- [57] Jiang, J.X., et al. Thermoelectric properties of  $\beta$ -FeSi<sub>2</sub> with Si dispersoid formed by decomposition of  $\alpha$ -Fe<sub>2</sub>Si<sub>5</sub> base alloys. J. Alloy and Comp. 319 (2005): 115-122.
- [58] Kuei, Y., et al. Synthesis of bulk  $\beta$ -FeSi<sub>2</sub> crystal. Jpn. J. Appl. Phys. 41 (2002) : 3854-3859.
- [59] Waldecker, G., et al. Thermal conductivity of semiconducting and metallic FeSi<sub>2</sub>. Phys. Status Solidi A 15 (1973): 143-149.



ศูนย์วิทยทรัพยากร  
จุฬาลงกรณ์มหาวิทยาลัย

## VITAE

Aparporn Sakulalavek was born on 29<sup>th</sup> July 1979 in Phetchaburi province, Thailand. She was a student in Development and Promotion for Science and Technology Talent Project (DPST) since 2000-2010. She received his Bachelor of Science degree (Second Class Honors) in Physics from Silpakorn University in 2001, and received her Master of Science degree in Physics from Chulalongkorn University in 2006.

## LIST OF CONTRIBUTIONS

1. A. Sakulalavek and S. Kiatgamolchai, “The Effect of Annealing Time on Seebeck Coefficient of Iron-Silicon compound” 7<sup>th</sup> Eco-Energy and Materials and Engineering Symposium, Chiang Mai, Thailand, 17-20 November 2009.
2. A. Sakulalavek and S. Kiatgamolchai, “Structural investigation and Thermoelectric Power of FeSi<sub>2</sub> and FeSi<sub>2,3</sub>” *Siam Physics Congress 2010 (SPC 2010)*, Kanchanaburi, Thailand, 25-27 March 2010 .
3. A. Sakulalavek and S. Kiatgamolchai, “Structural investigation and thermoelectric power of Fe-Si compound” Osaka International Convension Center, Japan, 14-18 November 2010.

## LIST OF PUBLICATION

1. S. Kiatgamolchai and A. Sakulalavek, “ Distribution of Elements in Cu-added FeSi<sub>2</sub> Alloy under Peritectoid and Eutectoid Reaction” *Journal of Electronic Materials* (2011).